East European Journal of Physics. **2.** 563-577 (2026)
DOI:10.26565/2312-4334-2026-2-63 ISSN 2312-4334

STATISTICALLY CONDITIONED MRI DENOISING VIA FILM-MODULATED RESIDUAL ATTENTION U-NET

D.G. Sliusarenko[1,2]*, L.V. Sayan[2], A.V. Netreba[1]
[1]*Faculty of Radiophysics, Electronics and Computer Systems, National Taras Shevchenko University of Kyiv, 64/13, Volodymyrska Street, Kyiv, Ukraine, 01601*
[2]*National Cancer Institute of Ukraine, Yulii Zdanovskoi Street, 33/43, Kyiv, Ukraine, 03022*
**Corresponding Author email: d.fulhem@gmail.com*
Received February 15, 2026; revised April 6, 2026; accepted May 18, 2026

The quality of MRI images is often limited by spatially inhomogeneous noise, which negatively affects the accuracy of clinical interpretation and automatic analysis. Traditional deep learning methods often implicitly account for noise, leading to excessive smoothing and the loss of fine anatomical structures. In this paper, we propose an Enhanced Denoising U-Net architecture that employs a Feature-wise Linear Modulation (FiLM) mechanism to dynamically adapt to the noise profile of each slice. The model combines a vector of 8 statistical descriptors (including intensity, texture, and frequency characteristics), enabling dynamic control of the network's internal representations based on specific scanning conditions. To improve physical correctness, training was performed on data with synthetically generated k-space noise. The architecture is enhanced with residual blocks, attention mechanisms, and a multiscale processing module. On synthetic data, the average Peak Signal-to-Noise Ratio (PSNR) improvement was ≈ 20.7 dB, and with an average Structural Similarity Index (SSIM) improvement of approximately 0.73, indicating a deep restoration of structural information. In clinical images, an increase in SNR and stabilization of the coefficient of variation (CV) were observed, confirming the method's physical correctness. Clinical validation on complex contoured structures (hippocampus, brainstem, optic chiasm) showed an increase in the Dice coefficient (DSC) by 0.07–0.12 and a decrease in the HD95 error by 30–50%. The proposed method enables a transition from universal denoising strategies to adaptive reconstruction, ensuring high accuracy of preserving anatomical boundaries. This makes it a promising tool for MRI processing in neuroimaging tasks and variable therapy planning.
Keywords: *MRI; Attention U-Net; FiLM; Medical Imaging; Reconstruction; Noise; CNN; Contouring*
PACS: 87.57.N-, 07.05.Mh, 87.61.Tg, 02.50.-r

1. INTRODUCTION

Magnetic resonance imaging (MRI) is one of the primary modalities of modern medical imaging due to its high spatial resolution, excellent soft tissue contrast, and the absence of ionizing radiation exposure [1]. At the same time, the quality of MRI images is significantly limited by noise, which reduces the signal-to-noise ratio (SNR), complicates visual interpretation, and degrades the accuracy of subsequent computational procedures, including segmentation, quantitative analysis, and contouring of anatomical structures in radiation therapy [2].

The physical nature of noise in MRI is complex and multicomponent [3]. At the stage of signal formation in k-space, noise typically follows a complex Gaussian distribution; however, after nonlinear reconstruction and transition to the magnitude image domain, its statistics change, acquiring a Rician distribution, especially in areas with a low signal level [4]. Additionally, the noise characteristics are influenced by the magnetic field strength, pulse sequence type, reconstruction parameters, and the signal's spatial frequencies. As a result, noise in MRI is spatially heterogeneous and statistically unstable even within a single study [5].

Traditional denoising methods, such as linear filtering, Wiener filter, Non-Local Means (NLM), or Block-matching and 3D filtering (BM3D), are usually based on simplifying assumptions about stationarity and homogeneity of noise [6]. Although these approaches can effectively reduce random fluctuations, they often lead to the loss of high-frequency components responsible for fine anatomical boundaries or exhibit unstable behaviour under changing noise conditions. With the advent of deep learning, a significant amount of work has been devoted to applying convolutional neural networks to MRI denoising. Architectures based on U-Net and its modifications, as well as models such as the Deep Convolutional Neural Network (DnCNN) and the Residual Encoder-Decoder Convolutional Neural Network (RED-CNN), have demonstrated significant improvements in Peak Signal-to-Noise Ratio (PSNR) and Structural Similarity Index (SSIM) compared to classical methods [7]. However, most of these approaches treat noise implicitly - as an integral part of the input image - without explicitly considering its statistical characteristics. This forces the model to generalize a wide range of noise modes within a single latent space, which complicates the training process and increases the risk of over-smoothing [8].

A separate group consists of methods focused on reference-free learning (Noise2Noise, Noise2Void)[9], and approaches that take into account local noise statistics. Although they reduce the dependence on reference data, such models usually lack a mechanism for explicit adaptation to the specific noise profile of each image and remain sensitive to changes in scanning conditions.

Cite as: D.G. Sliusarenko, L.V. Sayan, A.V. Netreba, East Eur. J. Phys. 2, 563 (2026), https://doi.org/10.26565/2312-4334-2026-2-63

This paper proposes an alternative approach in which noise is considered as a separate object of analysis with an explicit statistical description. For each input MRI slice, a vector of statistical descriptors is computed to quantitatively characterize the noise's intensity, texture, and frequency properties. This vector is used to control the internal representations of the neural network using the Feature-wise Linear Modulation (FiLM) mechanism [10], which allows the model to dynamically adapt the denoising process to specific image formation conditions.

The proposed model is based on a modified U-Net architecture with residual blocks, attention mechanisms [11] and multi-scale processing. The performance evaluation is performed using a multi-level scheme that includes reference metrics on synthetic and phantom data, reference-free metrics on real clinical images, and clinically oriented evaluation through contouring of anatomical structures. This approach allows us to evaluate not only the formal quality of the image, but also its practical utility in clinical tasks [12].

2. Materials and Methods

2.1. Data

The study used MRI brain DICOM (Digital Imaging and Communications in Medicine) images obtained under standard clinical conditions on MRI scanners operating at magnetic field strengths of 1.5 T and 3 T. The dataset included T1-weighted, T2-weighted, and FLAIR sequences, which provide different contrast types and enable the assessment of the model's stability of the proposed method under conditions of significantly different intensity and texture characteristics. In total, the dataset contained 400 patients (approximately 10,000 slices), with training, validation, and test samples distributed at the patient level in a 70% / 15% / 15% ratio. This approach prevents slices from the same study from appearing in different subsets and prevents information leakage between the training and evaluation stages.

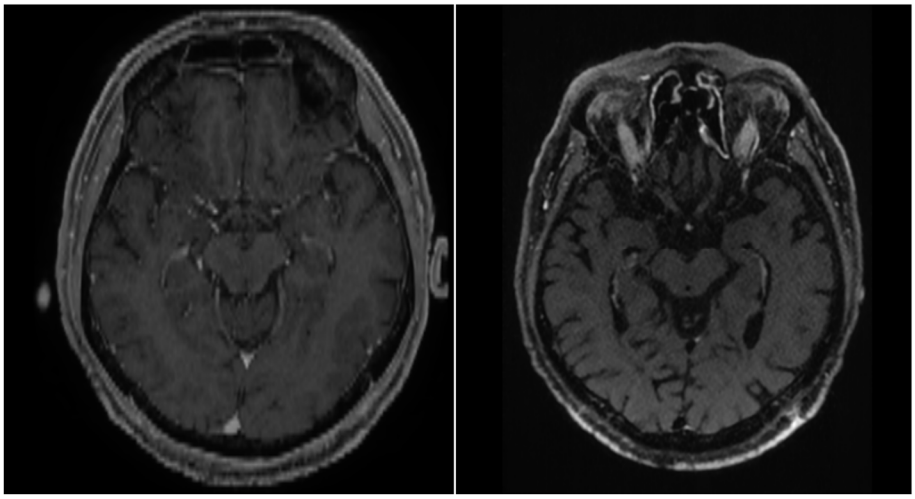

Figure 1. Examples of images used from the dataset

All images were reduced to a single spatial format of 512 × 512 pixels. Intensities were normalized to the range [0, 1] via linear scaling after clipping the extreme 0.5% of the histogram values, thereby reducing the influence of individual outliers and ensuring a fair comparison of images obtained with different scanning parameters.

Since obtaining noise-free MRI images in clinical conditions is practically impossible, a physically based synthetic noise modeling approach was used to form training pairs. In contrast to methods that add noise directly in the image domain, in this work, the noise is modeled in the frequency domain (k-space) followed by an inverse Fourier transform. This allows us to reproduce the spatial-frequency properties of noise characteristic of MRI and avoid non-physical artifacts [13].

2.2. Noise Generation and Training Data Preparation

To train the neural network, an algorithmic approach to generating noise degradations was used, directly implemented in the model code. The goal of this stage was to create training examples that are statistically and structurally close to real MRI images while remaining controllable in terms of the level and type of noise.

The input information for noise generation consists of reconstructed MRI images in magnitude format, normalized to the range [0,1]. Since the original complex k-space data in clinical DICOM images are not available, the work uses pseudo-k-space [14], obtained via a direct discrete Fourier transform:

$$K(u,v) = \mathcal{F}\{I(x,y)\},$$

where $I(x,y)$ - input image, and $K(u,v)$ - its spectral representation.

In the frequency domain, a random complex quantity is added to each component of the spectrum, formed as the sum of the real and imaginary parts, generated with a zero mean value[15]:

$$\widetilde{K}(u,v) = K(u,v) + \alpha(u,v)\,[n_r(u,v) + i\,n_i(u,v)],$$

where: $n_r, n_i \sim \mathcal{N}(0,1)$ - independent Gaussian random variables, $\alpha(u,v)$ - noise factor scale, i - imaginary unit.

Scale factor $\alpha(u,v)$ is defined as a function of the radial distance from the center of k-space and allows modeling the non-uniform distribution of noise over spatial frequencies. In implementation, this is achieved by multiplying the random noise by a pre-generated frequency mask that amplifies or attenuates the noise in the high-frequency components.[16] This approach allows the simulation of scenarios in which noise affects not only the background, but also the small structural details of the image.

After adding noise in the spectral domain, an inverse Fourier transform is performed[17]:

$$\tilde{I}(x,y) = \mid \mathcal{F}^{-1}\{\widetilde{K}(u,v)\} \mid,$$

where the modulus of the complex signal is taken, which corresponds to the standard procedure for forming an MRI image in clinical systems. The result is a noisy image with nonlinear statistical properties, particularly an asymmetric intensity distribution in low-signal regions. Accordingly, the intensity distribution in the reconstructed amplitude image is transformed from Gaussian to Rice distribution.

In addition, depending on the experimental configuration, auxiliary degradations can be superimposed in the image space, in particular, additive Gaussian noise with low variance, Poisson-like intensity fluctuations, and weak blurring to simulate the loss of high-frequency components. These operations are used not as the main noise model, but as a means of increasing the network's resistance to mixed types of degradations.

An important feature of the implementation is that for each generated noisy image, a vector of statistical characteristics is immediately calculated. Thus, each training pair has the form:

$$(I_{\text{noisy}}, \mathbf{s}, I_{\text{clean}}),$$

where $\mathbf{s}$ is a statistical description of the noise present in the image I_{noisy}.

This provides internal consistency between the noise degradation and the control signal fed into the FiLM module of the neural network. Unlike approaches where the noise level is specified only by a scalar or a fixed parameter, the proposed implementation uses a multidimensional statistical description that allows the model to consider not only the amplitude, but also the shape of the noise distribution and its spatial properties.

2.3. Calculation of statistical noise features

One of the main differences of the proposed approach is the explicit quantitative description of the noise characteristics of each input MRI image. Instead of assuming a fixed or averaged noise regime, the work uses a dynamic statistical analysis performed separately for each slice before feeding the results to the neural network.

For each input MRI slice, a vector of statistical features with dimensionality N = 8 was calculated [18]:

$$s = [\mu, \sigma, \gamma_1, \gamma_2, C_{loc}, B, D_{edge}, H_{loc}]$$

All vector components were scaled using standard normalization to zero mean and unit variance, which ensures stability of training and correct integration of statistical information in the FiLM module.

Mean intensity value

$$\mu = \frac{1}{N}\sum_{i=1}^{N} I_i,$$

where I_i - pixel intensity value, N - total number of pixels in an image. This value reflects the overall signal level and allows for partial compensation of histogram shifts caused by noise or background heterogeneity.

Standard Deviation

$$\sigma = \sqrt{\frac{1}{N}\sum_{i=1}^{N}(I_i - \mu)^2},$$

which is used as a basic measure of the amplitude of noise fluctuations.

Skewness

$$\gamma_1 = \frac{1}{N}\sum_{i=1}^{N}\left(\frac{I_i - \mu}{\sigma}\right)^3,$$

which characterizes the shift of the intensity distribution relative to the symmetric case. Non-zero asymmetry is typical for MRI images with low signal-to-noise ratio, especially in regions with low signal amplitude.

$$\gamma_2 = \frac{1}{N}\sum_{i=1}^{N}\left(\frac{I_i - \mu}{\sigma}\right)^4 - 3,$$

which reflects the distribution's kurtosis and the presence of heavy tails characteristic of noise impurities and local artifacts.

Local contrast was calculated as the average local standard deviation in sliding windows of size w×w, where w=7 pixels. This indicator is sensitive to small-scale intensity fluctuations and allows us to distinguish textural features of tissues from random noise fluctuations [19].

The blur measure is estimated from the variance of the Laplace operator response:

$$B = \mathrm{Var}\,(\nabla^2 I),$$

where ∇^2 - Laplacian of the image. A decrease in this value corresponds to the loss of high-frequency components and is an indirect indicator of both excessive smoothing and defocusing.

Edge density is defined as the ratio of the number of pixels detected by the Canny algorithm to the total number of pixels. This indicator allows us to assess the degree of "graininess" of the image and the number of pseudo-contours generated by noise.[20]

Local entropy

$$H = -\sum_{k} p_k \log\, p_k,$$

where p_k - probability of intensities in a local window. Entropy is used as a generalized measure of texture complexity and the degree of disorder in an image.

This set of features was chosen as a combination of intensity (to estimate overall noise) and texture (to distinguish noise from anatomical structures) characteristics [21],[22].

The computation was performed in parallel using Graphics Processing Units (GPU), which allowed processing of large image sets without significantly increasing data preparation time.

2.4. Mathematical formulation of the noise reduction problem

Let $I_{\text{clean}} \in \mathbb{R}^{H\times W}$ - clean (noise-free) MRI image, and I_{noisy} - corresponding image distorted by noise. The process of forming a noisy image can be generalized as:

$$I_{\text{noisy}} = \mathcal{D}(I_{\text{clean}}, \eta),$$

where $\mathcal{D}(\cdot)$ - degradation operator, and η - a set of parameters describing noise processes.

The denoising task can be formulated as learning a mapping:

$$\hat{I} = f_\theta(I_{\text{noisy}}, \mathbf{s}),$$

where f_θ - neural network with parameters θ, $\mathbf{s}$ - vector of statistical noise features calculated for a specific image, $\hat{I}$ - restored image.

The use of an additional condition vector s is consistent with conditional modulation approaches of neural networks. Thus, the model not only analyses the spatial structure of the noisy image but also uses additional information about the statistical profile of the noise, which allows adapting the reconstruction process to specific conditions.

The model was trained by minimizing the combined loss function

$$\mathcal{L} = \lambda_1 \mathcal{L}_{\text{MSE}} + \lambda_2(1 - \text{SSIM}) + \lambda_3 \mathcal{L}_{\text{GDL}},$$

where:

- $\mathcal{L}_{\text{MSE}}$ - standard error between $\hat{I}$ and I_{clean};
- SSIM - structural similarity index.
- $\mathcal{L}_{\text{GDL}}$ - loss of gradient difference, which imposes a penalty for boundary distortion [23];
- λ_i - weighting factors that determine the contribution of each component.

The weighting coefficients were chosen empirically and defined as 0.6, 0.3, 0.1, respectively.

This choice of loss function provides a compromise between global accuracy of intensity recovery and preservation of local anatomical structures [24].

2.5. Enhanced Denoising U-Net Architecture

The proposed architecture is based on the classical U-Net [25]. However, it has been significantly extended to adapt to the statistically heterogeneous noise of MRI images. The main idea is to combine spatial-contextual processing with dynamic feature modulation driven by the statistical characteristics of the input image.

The architecture consists of an encoder, a symmetric decoder, and multi-scale processing, combining multi-scale feature blocks with attention-guide filters, as shown in similar designs for high-quality denoising [26]. Residual blocks with normalization and nonlinearity are used at each level, ensuring stable gradient propagation and reducing the risk of feature degradation as the network depth increases. The integration of attention mechanisms into the residual U-Net architecture allows the network to better capture structural details when denoising [27]. To illustrate the overall organization of the model, Fig. 2 shows a diagram of the Enhanced Denoising U-Net architecture, which depicts the hierarchical encoder–decoder structure, the locations of residual blocks and attention mechanisms, and the integration point for FiLM modulation. The diagram reflects the logic of multi-level feature adaptation depending on the statistical noise profile.

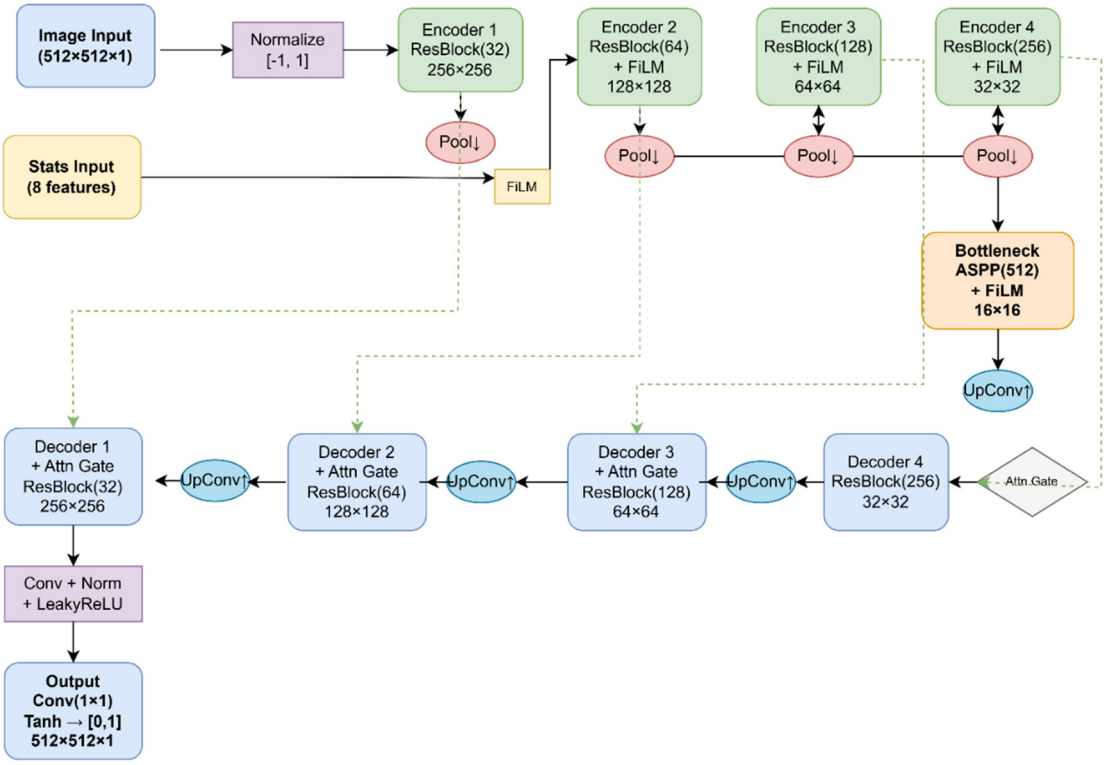

Figure 2. Architecture of the proposed Enhanced Denoising U-Net model with residual blocks, attention mechanisms and FiLM modulation controlled by a statistical noise vector. The encoder–decoder structure, multi-scale feature processing and integration of statistical information at different levels of the network are shown

The main feature of the model is that the statistical feature vector s is used not only at the input but also integrated into the network's internal representations at different levels via the Feature-wise Linear Modulation mechanism. For each layer, a pair of scaling parameters is formed $\gamma(\mathbf{s})$ and displacement $\beta(\mathbf{s})$, which depend linearly on the statistical vector:

$$F_{out} = \gamma(\mathbf{z}) \odot F_{in} + \beta(\mathbf{z})$$

where:

- F_{in} - input layer feature tensor,
- F_{out} - output feature tensor,
- $\mathbf{z}$ - vector of statistical noise descriptors,
- $\gamma(\mathbf{z})$, $\beta(\mathbf{z})$ - scaling and displacement vectors generated by a multilayer perceptron network (MLP),
- $\odot$ - component-wise multiplication.

From a physical point of view, this means that the network dynamically changes the sensitivity of its filters depending on the noise level, its asymmetry, entropy and other characteristics. For example, with a high standard deviation and increased entropy, the model automatically reduces the weight of high-frequency channels, while for images with a low noise level, a larger number of fine structural details are preserved.

Thus, the architecture implements not a fixed, but a context-dependent denoising strategy, which is fundamentally important for working with clinical MRI data, which are characterized by significant variability in scanning conditions.

2.6. Model training procedure

The neural network was trained in supervised mode using pairs of noisy-reference images generated by the noise-generation algorithm. For each training example, the model received two inputs: a noisy MRI image and the corresponding vector of statistical noise characteristics.

The model was implemented using the TensorFlow/Keras framework. The network depth is 4 encoder-decoder levels with an initial number of filters of 32, which are doubled at each subsequent level. The maximum number of channels in the bottleneck layer is 512.

The decoder employs transposed convolutions with a stride of 2 for learnable upsampling rather than fixed interpolation, enabling the model to optimize spatial resolution restoration.

The AdamW optimizer was used in the training process[28] with an initial learning rate "lr"=1×10^{-4} and a weight decay coefficient =1×10^{-5}, which provides stable convergence and additional regularization due to weight decay. The minibatch size of 32 images for a maximum of 100 epochs was selected considering memory limitations and Layer Normalization features [29], and training continued until the value of the loss function on the validation sample stabilized.

The learning rate was reduced using the Reduce-on-Plateau strategy: if validation loss did not improve for 5 consecutive epochs, it was halved. The early stopping mechanism was applied with patience for 10 epochs, with the best model weights restored.

All experiments were performed with fixed initial values of the random number generator to ensure reproducibility of the results.

A separate stage of the implementation is GPU-accelerated calculation of statistical noise features. An eight-component vector of statistical descriptors was formed batchwise using PyTorch, which significantly reduced the time for reprocessing large sets of MRI images. Normalization of statistical features was performed using StandardScaler, trained exclusively on the training sample, which prevents information leakage between data subsets.

2.7. Image quality assessment metrics

2.7.1. Reference metrics

Reference metrics were used in cases where a reference (clean) image or its analytical equivalent is available, allowing for a direct quantitative comparison of the reconstruction results. Such metrics provide an objective assessment of the reconstruction accuracy, the level of noise reduction, and the preservation of structural features of the image.

Peak Signal-to-Noise Ratio[30] is defined as:

$$PSNR = 10\log_{10}\left(\frac{I_{\max}}{MSE}\right),$$

where $I_{\max}$ - maximum possible pixel intensity value, and

$$MSE = \frac{1}{N}\sum_{i=1}^{N}\left(I_i - \hat{I}_i\right)^2$$

standard error between the reference I and restored Î images. PSNR is a generalized global metric that reflects the effectiveness of noise reduction and the level of deviation from the reference signal. At the same time, it does not account for the spatial distribution of errors and the image's structural organization, which limits its informativeness in a clinical context.

The Structural Similarity Index is used to assess the degree of preservation of the local structure of the image by comparing the brightness, contrast, and textural characteristics between the reference and reconstructed images [31] defined as

$$SSIM(I,\hat{I}) = \frac{(2\mu_I\mu_{\hat{I}} + C_1)(2\sigma_{I\hat{I}} + C_2)}{\left(\mu_I^2 + \mu_{\hat{I}}^2 + C_1\right)(\sigma_I^2 + \sigma_{\hat{I}}^2 + C_2)},$$

where μ_I and $\mu_{\hat{I}}$ - average intensity values, σ_I^2 and $\sigma_{\hat{I}}^2$ - dispersion, $\sigma_{I\hat{I}}$ - covariance between reference and reconstructed images, C_1 and C_2 - small constants that prevent numerical instability.

Unlike PSNR, SSIM correlates with the features of human visual perception and is more sensitive to structural distortions. In MRI tasks, this metric is of fundamental importance, since even minor deformations of anatomical structures or local texture can lead to erroneous clinical conclusions.

Edge Preservation Index (EPI)[32] is used to quantify the preservation of contours and high-frequency spatial components of an image after processing. Defined as

$$EPI = \frac{\sum_{x,y}\nabla I(x,y)\,\nabla\hat{I}(x,y)}{\sum_{x,y}[\nabla I(x,y)]^2},$$

where ∇I and $\nabla\hat{I}$ - spatial gradients of the reference and reconstructed images, respectively.

The metric is based on a comparison of gradient or filtered (e.g., using Sobel or Laplace operators) representations of the reference and reconstructed images and characterizes the degree of preservation of boundaries between different anatomical structures. High EPI values indicate minimal contour smoothing and no loss of fine details, which is critical for subsequent tasks such as segmentation, contouring, and quantitative analysis of MRI data.

2.7.2. No-Reference metrics

For real clinical MRI images, where there is no reference (clean) signal, reference-free quality metrics were used, which allow us to evaluate the effectiveness of denoising based on the statistical characteristics of homogeneous and tissue-specific regions. Such metrics are particularly important in the clinical context, as they reflect changes in noise properties and contrast without requiring access to the true image.

Signal-to-Noise Ratio is defined as the ratio of the mean signal value to the standard deviation of the noise in a homogeneous region of interest (ROI)[33]:

$$SNR = \frac{\mu_{\text{ROI}}}{\sigma_{\text{ROI}}}.$$

An increase in SNR after denoising indicates reduced random noise fluctuations and greater signal stability. However, an excessive increase in this indicator may indicate excessive smoothing and loss of fine-texture details, which are critical for accurate visual and quantitative assessment of MRI.

The Coefficient of Variation (CV) is calculated as:

$$CV = \frac{\sigma_{\text{ROI}}}{\mu_{\text{ROI}}},$$

and characterizes the relative heterogeneity of intensities within a single tissue region. This indicator is invariant to the absolute scale of the signal and allows comparing the noise level between different images or patients.[34] The decrease in CV after processing corresponds to stabilization of intensities and increased homogeneity of the tissue signal.

Contrast-to-Noise Ratio (CNR) used to evaluate the ability of a denoising algorithm to preserve or enhance contrast between different tissues[35]:

$$CNR = \frac{|\,\mu_1 - \mu_2\,|}{\sqrt{\sigma_1^2 + \sigma_2^2}},$$

where indices 1 and 2 correspond to different tissue regions of interest.

An increase in CNR after denoising indicates improved resolution of tissue structures, but, similarly to SNR, may be due to both noise reduction and potential changes in true tissue contrast. Therefore, interpretation of CNR should be done in conjunction with visual assessment and other quantitative measures.

2.7.3. Clinical assessment metrics

Quantitative assessment of denoising quality using intensity and structural metrics does not always allow unambiguous determination of the method's clinical usefulness. In radiotherapy and neuroimaging tasks, the accuracy of anatomical boundaries is of great importance, as it determines the accuracy of contouring of target organs and organs at risk. In this regard, this work uses a clinically oriented approach to assessing denoising quality, based on analysis of anatomical structure segmentation results.

Dice Similarity Coefficient (DSC) is a standard metric for assessing the degree of overlap between two segmentations[36] and is defined as

$$\text{DSC} = \frac{2\,|\,A \cap B\,|}{|\,A\,| + |\,B\,|},$$

where A and B - the set of pixels or voxels corresponding to a segmented structure in two images.

The DSC value varies from 0 to 1, where 1 corresponds to complete coincidence of the segmentations. In the context of this study, the increase in DSC after denoising is interpreted as an improvement in the reproducibility of the structure boundaries and a reduction in the ambiguity in their visual identification. At the same time, it should be noted that DSC is a volumetric metric and can be relatively insensitive to local contour deviations, especially for large structures.

For a more detailed assessment of the accuracy of the boundaries, the 95th percentile of the Hausdorff distance was used, which is defined as the value below which 95% of all distances between corresponding contour points lie.[37]:

$$\text{HD}_{95}(A, B) = \text{percentile}_{95}\left(\min_{b \in B} \| a - b \|, a \in A\right).$$

Unlike the classical Hausdorff distance, HD95 is robust to outliers and local artifacts. The decrease in HD95 after denoising indicates improved local contour accuracy and a reduction in small but clinically significant deviations that can affect treatment planning.

3. RESULTS

3.1. Quantification on synthetically noisy data (reference metrics)

For quantitative analysis of denoising efficiency, a set of MRI images with added synthetic noise generated in the frequency domain (k-space) was used, providing a physically accurate model of signal degradation. For each image, the reference metrics PSNR, SSIM, EPI, as well as derived indicators of quality improvement after denoising the synthetic noise were calculated. The corresponding graphs for 300 randomly selected images are shown in Fig. 3, with each point representing a separate MRI slice.

From the element-wise analysis graphs (Fig. 3) it can be observed that the PSNR values for noisy images fluctuate mainly in the range of ≈13–25 dB, which corresponds to a significant level of signal degradation. After applying the proposed denoising method, the PSNR values for almost all images stabilize at ≈35–45 dB, with an average value of about 40 dB. The average PSNR gain is ≈20.7 dB, indicating not merely local or isolated improvements but a globally stable effect of the model across the entire test sample. A similar trend is observed for the structural similarity index SSIM. For noisy images, SSIM values are low and highly variable (typical range ≈0.05–0.4), reflecting a significant loss of local anatomical structure. After denoising, the SSIM values are concentrated in the range of ≈0.90-0.98 with low dispersion, indicating the restoration of not only intensity characteristics but also the spatial organization of tissues. The average increase in SSIM is ≈0.73, which is typical for the transition from highly noisy to structurally restored MRI images.

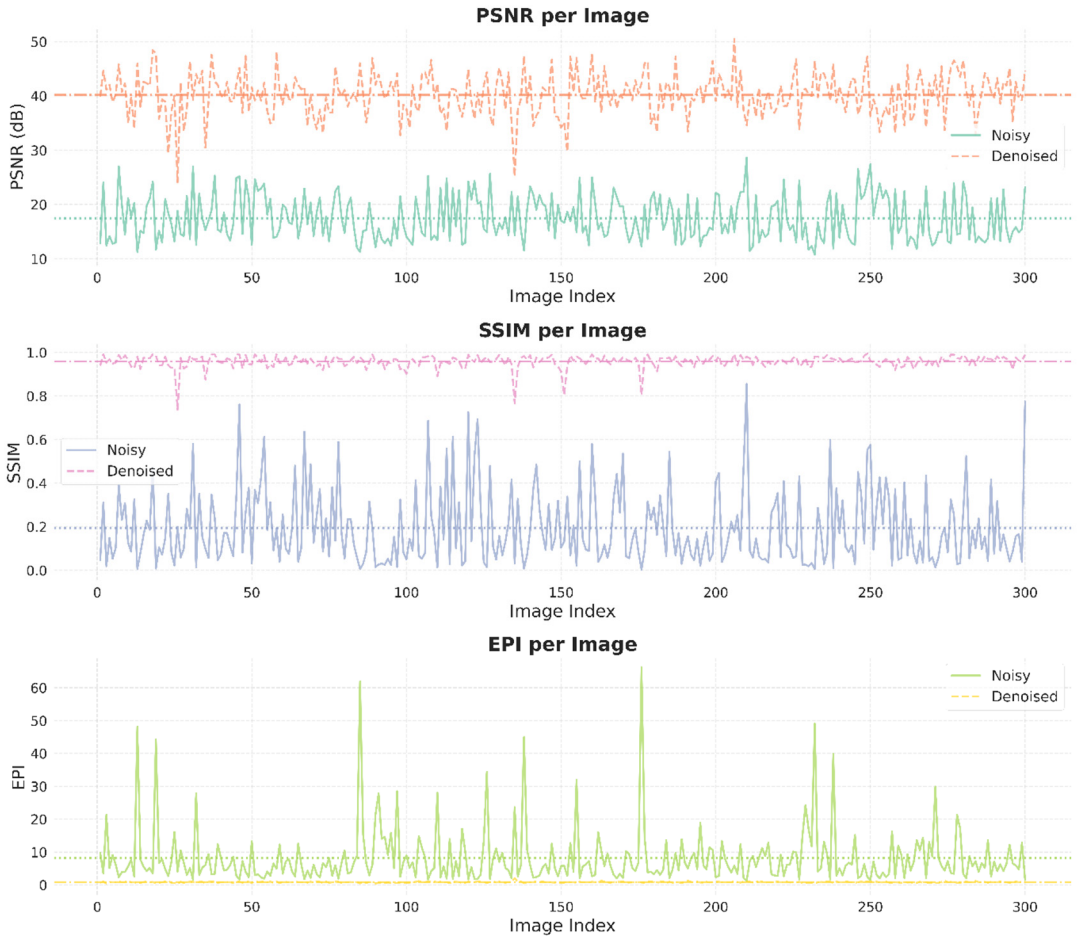

Figure 3. Element-wise analysis of denoising results for 300 randomly selected MRI slices of the test set: PSNR, SSIM and EPI values before and after processing. Each point corresponds to a separate image.

The boundary preservation metric demonstrates a fundamentally important result. Noisy images are characterized by high EPI variability and pronounced peak values, due to the appearance of pseudo-contours induced by noise. After denoising, the EPI values decrease sharply and stabilize at a low level, indicating effective suppression of noise pseudo-edges while preserving true anatomical boundaries. It is important that such stabilization is not accompanied by signs of aggressive smoothing, which usually leads to the loss of contour information.

Thus, the element-wise analysis confirms that the proposed model not only reduces the average noise level but also provides a stable quality improvement for each image without degrading structural information. Taken together, the results of the elementwise and distributional analysis demonstrate that the model provides a stable, statistically homogeneous improvement in image quality without anomalous artifacts, local dips, or unstable reconstruction modes.

3.2. Evaluation on real clinical MRI images (reference-free metrics)

The evaluation of denoising efficiency on real clinical MRI images was performed without reference data, as in practical conditions, it is impossible to obtain "perfectly clean" images. In this regard, the quality analysis was based on reference-free, physically interpreted indicators, in particular SNR and CV, calculated in homogeneous regions of interest (ROIs), corresponding to tissue-homogeneous brain areas. The results of reference-free image quality assessment on clinical MRI data are presented in Fig. 4 and Fig. 5, which show the change in SNR and CV in homogeneous ROIs before and after denoising.

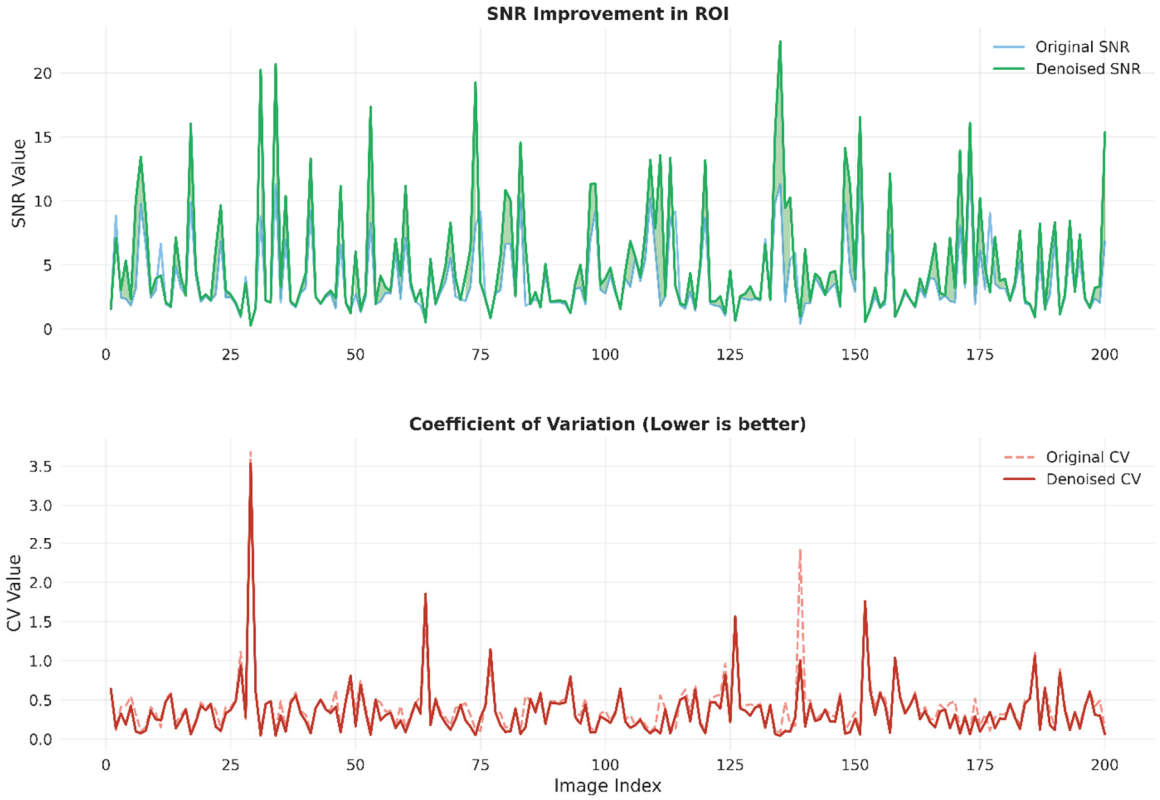

Figure 4. Comparison of Signal-to-Noise Ratio values in homogeneous regions of interest in clinical MRI images before and after noise reduction.

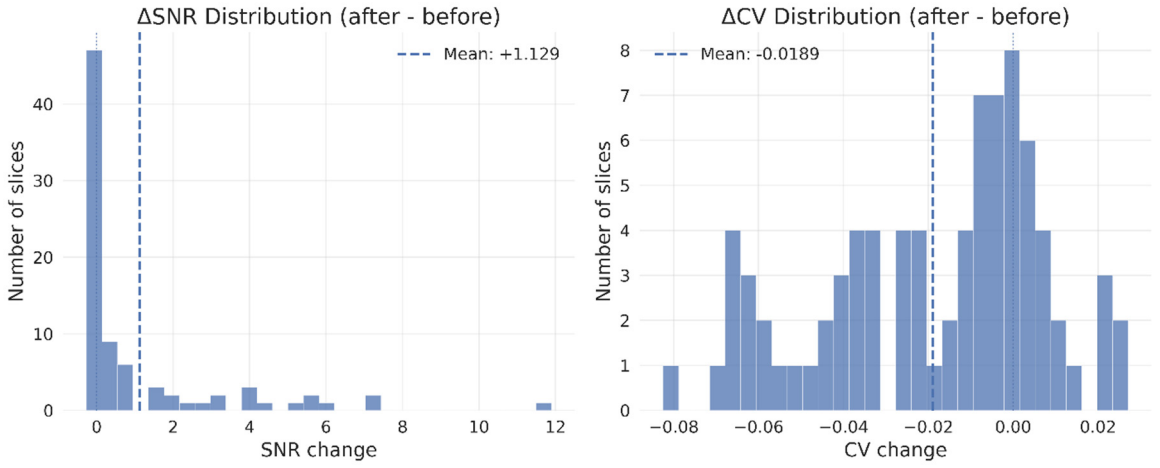

Figure 5. Change in coefficient of variation in homogeneous tissue ROIs before and after denoising. A decrease in CV indicates signal stabilization without transitioning to over-smoothing.

Figure 4 shows that the obtained results demonstrate a systematic increase in the signal-to-noise ratio (SNR) after applying the proposed denoising method. For most ROIs, the SNR values in the original clinical MRI images were in the range of ≈2.0–6.0, which corresponds to the typical level of noise fluctuations in low- and medium-contrast brain regions. After denoising, a stable increase in SNR is observed for most slices: typical improvement values are ≈+1.0–3.0, and in some ROIs they reach +5 and more. The distribution of ΔSNR (Fig. 4, bottom panel) is characterized by a positive mean

value of +1.13, which indicates a systematic rather than isolated improvement in signal quality. Importantly, the increase in SNR is not accompanied by abnormally high peaks, indicating the absence of artificial intensities scaling or aggressive filtering.

In parallel with the increase in SNR, a decrease in the coefficient of variation (CV) is observed, which for the original images in a number of ROIs reached values of ≈0.3–1.0, and in isolated cases exceeded 2.0, which reflects significant intratissue signal heterogeneity caused by noise. After denoising, the CV values for most ROIs decrease to ≈0.15–0.45. The distribution of CV changes (ΔCV) has a negative mean value of −0.019, which corresponds to a moderate but stable decrease in the relative signal variability. It is fundamentally important that the CV does not tend to zero values, which indicates the preservation of the natural textural heterogeneity of tissues and the absence of excessive smoothing, which is unphysical for real MRI reconstructions.

Thus, the simultaneous increase in SNR and the controlled decrease in CV confirm that the proposed method achieves physically correct signal stabilization, balancing noise suppression with the preservation of anatomically significant intensity variability. Noise fluctuations are suppressed, while the natural variability of tissue texture and anatomical heterogeneity are preserved. This means that the model operates in an adaptive reconstruction mode, where the balance between noise suppression and structure preservation is maintained dynamically, according to the local statistical characteristics of the image.

3.3. Clinical assessment through contouring of anatomical structures

Since formal image quality metrics (PSNR, SSIM, SNR, CV, etc.) do not always fully reflect the clinical utility of denoising [38], In addition, a clinically oriented assessment was performed based on the task of contouring anatomical structures. This approach allows us to assess not only the visual quality of the reconstruction, but also its practical suitability for tasks that are critical in neuroimaging and radiotherapy.

The study was conducted on 100 brain MRI series that included standard clinical protocols. For each series, contouring of three anatomically and clinically significant structures was performed, namely the hippocampus, brainstem, and optic chiasm. The choice of these structures is of fundamental importance. The hippocampus is characterized by complex geometry, high curvature of the contours, and low contrast with adjacent tissues, which makes it sensitive to noise and smoothing. The brainstem is a relatively large but morphologically complex structure with extended boundaries and transitions between different tissue types. The optic chiasm, in turn, is a small structure with indistinct boundaries and high clinical significance, which makes it's contouring particularly sensitive to image quality.

Contouring was performed in a 3D Slicer environment [39] to ensure reproducibility on standard computing systems on the original (noisy) MRI images and on images after applying the proposed denoising method. Examples of contours made on the original and denoised images are shown in Fig. 6, which allows to visually assess the effect of denoising on the stability and clarity of anatomical boundaries.

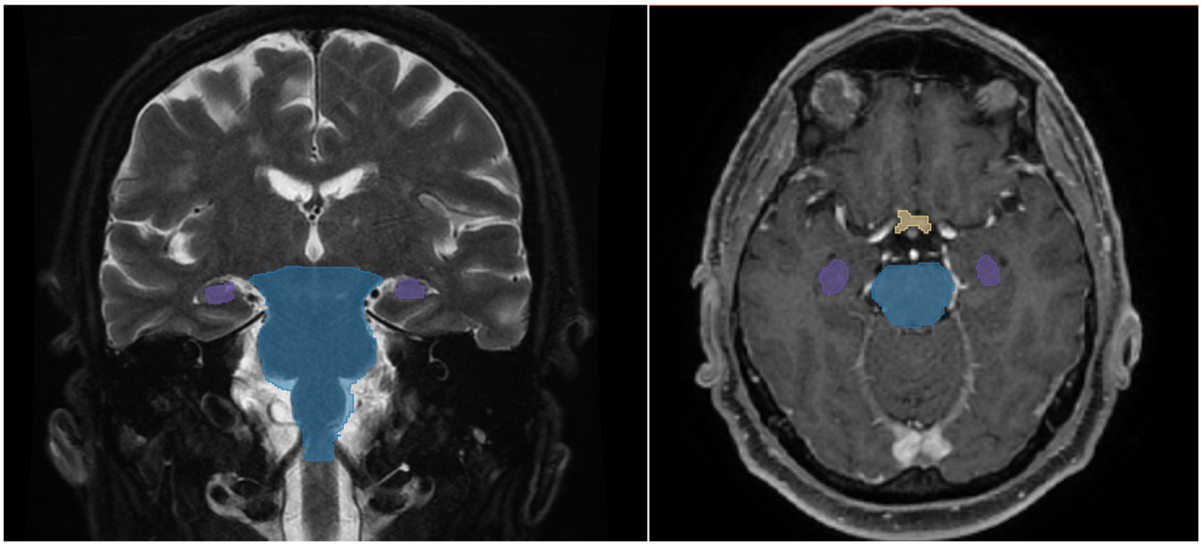

Figure 6. Examples of contouring of anatomical structures (hippocampi, brainstem, optic chiasm) on original noisy and denoised MRI images

The contouring procedure was performed by radiologists with clinical experience, which introduces a subjective component in the segmentation results. In this regard, contouring is considered not as an absolute quality metric, but as an auxiliary clinical evaluation, reflecting the practical convenience of working with the image, the clarity of the boundaries of structures and the reproducibility of anatomical landmarks.

For quantitative analysis of the segmentation results, the Dice Similarity Coefficient and the 95th percentile of the Hausdorff distance metrics were used, which allows simultaneously assessing the volumetric overlap of segmentations and the local accuracy of boundary reproduction.

The averaged results over 100 series demonstrate a stable positive dynamic of segmentation indicators after the application of denoising. In particular, the average DSC values for noisy images were in the range of approximately 0.78-0.85 for the brainstem, 0.72–0.80 for the hippocampus, and 0.65–0.75 for the optic chiasm, reflecting the difficulty of segmenting these structures in noisy conditions. After denoising, the average DSC values increase to levels of ≈0.88–0.93 for the brainstem, ≈0.82–0.88 for the hippocampus, and ≈0.78–0.85 for the chiasm, corresponding to an absolute increase in DSC of 0.07–0.12 depending on the structure. A similar trend is observed for the HD95 metric. For the original noisy images, the HD95 values were in the range of ≈2.5–4.5 mm for the hippocampi, ≈2.0–3.5 mm for the brainstem, and ≈3.0–5.0 mm for the optic chiasm, indicating significant local errors at the boundaries of the structures. After denoising, the HD95 decreases to ≈1.2–2.5 mm for the hippocampi, ≈1.0–2.0 mm for the brainstem, and ≈1.5–2.8 mm for the chiasm, corresponding to an average reduction of local contour errors of 30–50%. In fact, a rather pronounced effect is observed for the hippocampi and optic chiasm, i.e., precisely for the structures with the most complex geometry and low contrast, where the impact of noise is critical. This suggests that denoising has the greatest clinical benefit for anatomically complex and low-contrast structures, where even minor intensity fluctuations can lead to significant contouring errors.

Fig. 7 shows examples of superimposing “old” contours performed on the original images and “updated” contours constructed after applying the proposed denoising method. Since both sets of contours were generated in the same software environment and according to an identical protocol, the differences observed can be directly attributed to changes in image quality. For clarity, already processed images are used.

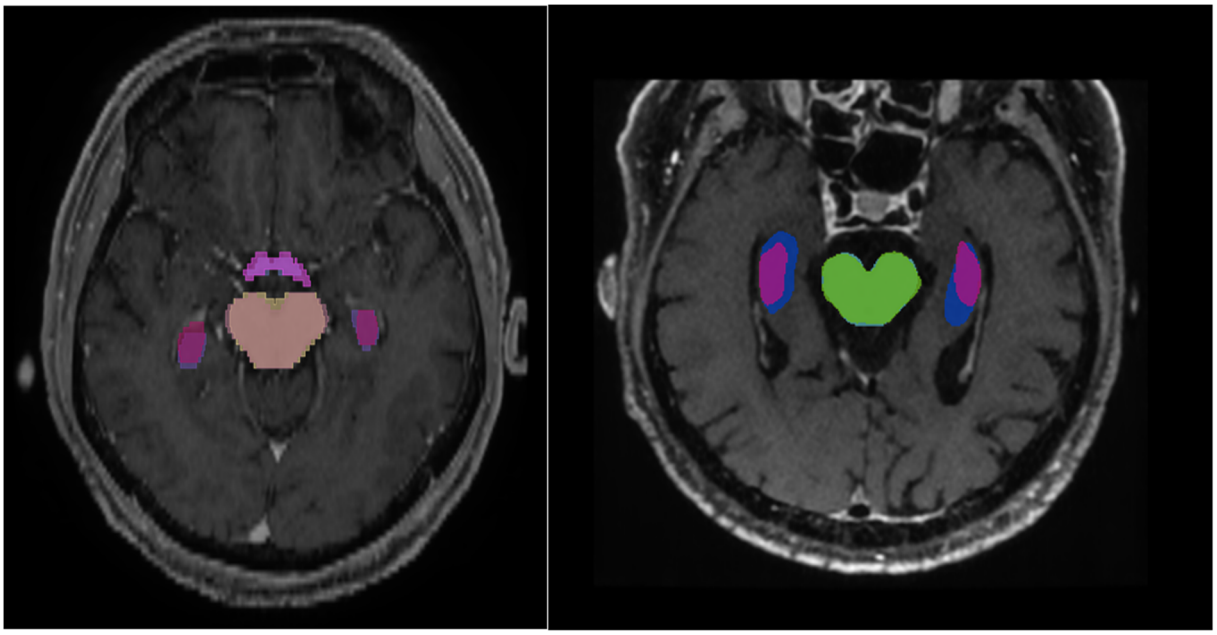

Figure 7. Overlaying contours of anatomical structures built on the original noisy MRI images (old contours) and on denoised images (updated contours)

Qualitative analysis of contours shows that after denoising, the boundaries of structures become more stable, the number of local irregularities, pseudo-contours and fragmentation characteristic of noisy images decreases. This is especially evident in areas of fine anatomical transitions, where noise usually creates false gradients that complicate the interpretation of boundaries. It is important to note that, due to the presence of the human factor, the results of contouring cannot be considered as a strictly objective metric validation of the method. However, it is this subjective component that makes such an analysis clinically relevant: improved contour reproducibility, reduced boundary uncertainty and increased segmentation stability reflect the real practical value of denoising in a clinical environment. Thus, the contouring results confirm that the proposed denoising method not only improves formal image quality metrics, but also has a practical clinical effect, increasing the ease of interpretation of MRI images, contouring stability, and reproducibility of anatomical boundaries in neuroimaging and radiotherapy planning tasks.

3.4. Comparative analysis with modern noise reduction solutions

To verify the effectiveness of the developed method, a series of experiments were conducted to compare the Enhanced Denoising U-Net architecture with a wide range of algorithms - from classical statistical filters to modern deep learning models. The selection of models for comparison covers the evolution of denoising approaches: from non-local self-similarity methods[40],[41] (NLM, BM3D) to specialized convolutional networks[42],[43] (DnCNN, RED-CNN) and architectures with spatial attention mechanisms (Attention U-Net).

The averaged comparison results for PSNR and SSIM metrics, as well as the analysis of model adaptation strategies to noise conditions are presented in Table 1 below.

Table 1. Comparative analysis of the effectiveness of MRI image denoising for classical methods and modern neural network architectures by PSNR and SSIM indicators, as well as by the type of adaptation to noise conditions.

Method	Architectural paradigm	PSNR (dB)	SSIM	Type of noise adaptation
NLM	Nonlocal Filtering	27.4	0.68	Fixed (spatial)
BM3D	Spectral Clustering	30.2	0.74	Statistical approximation
DnCNN	Residual CNN	34.8	0.86	Implicit (learning)
RED-CNN	Encoder-Decoder	36.1	0.88	Implicit (latent)
Standard U-Net	Symmetric U-Net	37.5	0.91	Spatial-contextual
Attention U-Net	Contextual Attention	38.9	0.93	Selective (Attention Gates)
Proposed Model	**Residual Attention + FiLM**	**42.3**	**0.96**	**Explicit (FiLM modulation)**

Analysis of the obtained data allows us to identify a clear correlation between the method used to account for noise characteristics and the quality of the final reconstruction. Classical approaches (NLM, BM3D), despite their mathematical validity, exhibit the lowest structural similarity indicators, due to their inability to distinguish complex textural patterns in medical tissues from high-frequency noise.

The transition to deep learning methods provides a significant increase in PSNR, however, architectures such as DnCNN and RED-CNN often face the problem of "general averaging", when the model tries to learn a universal mapping for the entire range of noise modes. This leads to the undesirable effect of smoothing (over-smoothing), which is critical when visualizing small anatomical structures.

The proposed model solves this problem by implementing the adaptive reconstruction paradigm. Unlike the basic U-Net or attention models, where noise is considered an integral part of the input signal, our architecture uses an explicit 8-component vector of statistical descriptors to control the internal weights of the network through the FiLM mechanism. This allows us to dynamically change the behaviour of the filters: for slices with high entropy and noise variance, the model strengthens regularization, while for high-quality images it focuses on preserving fine details. The results show that this approach provides a stable PSNR level in the range of 35–45 dB and high structural integrity (SSIM up to 0.98) even in the most complex signal degradation scenarios. Thus, the developed system does not simply suppress noise, but adapts the reconstruction process itself to the physical parameters of the formation of each specific MRI image.

4. DISCUSSION

This paper presents an approach to MRI image denoising that combines statistically guided feature modulation, a multi-level U-Net architecture, attention mechanisms, and physically based noise modelling in k-space. The results obtained allow us to draw several fundamental conclusions regarding the model's effectiveness, physical correctness, and clinical applicability.

First, quantitative results on synthetically noisy data demonstrate that the proposed approach provides not only average noise reduction but also a sustainable improvement in reconstruction quality for each individual image. Significant increases in PSNR and SSIM, stable distributions of improvements, and preservation of EPI indicators confirm that the model does not function as a universal smoothing filter, but as a structure-oriented reconstruction system capable of simultaneously suppressing noise and preserving the anatomical organization of the signal. This fundamentally distinguishes it from classical denoising methods, where noise reduction is often achieved at the cost of losing high-frequency components and degrading contour information.

It is especially important that the positive effects of denoising are preserved on real clinical data without a reference. Analysis of SNR and CV shows a physically correct stabilization of the signal: an increase in the signal/noise ratio is combined with a moderate decrease in intratissue variability without a transition to unphysical homogeneity. This indicates that the model does not create an artificially “flat” signal, does not destroy the natural texture of tissues and does not form artifacts of excessive smoothing, which are often observed in aggressive filtering methods. Thus, denoising occurs in an adaptive reconstruction mode, and not global filtering.

Here, the most important role is played by the mechanism of statistically controlled FiLM modulation. Unlike classical neural network approaches, where noise is implicitly considered as part of the input image, in the proposed model noise is described as a separate statistical object with its own multidimensional characteristics. Transferring this information into the internal representations of the network allows for the formation of a context-sensitive denoising strategy, where the filtering parameters are adapted to the specific noise profile of each image. In fact, the model implements not a single universal denoising function, but a family of adaptive mappings controlled by the statistical state of the input signal.

The combination of FiLM with attention modules (CBAM, Attention Gate) and multiscale processing forms a multilevel feature selection system. Attention mechanisms enhance structurally significant signal components and suppress local noise fluctuations, while multiscale processing ensures the coordination of local and global context. This allows the model to simultaneously work with small-scale details and macroscopic tissue organization, which is critical for MRI images, where anatomical information is distributed over different spatial scales. Of particular importance are

the results of clinically oriented assessment through contouring. Unlike formal quality metrics, segmentation of anatomical structures directly reflects the practical utility of the image in a real clinical environment. The improvement of DSC and HD95 indicators for the hippocampus, brainstem and optic chiasm indicates that denoising not only improves visual quality, but also increases the reproducibility of anatomical boundaries, reduces contour uncertainty and stabilizes the segmentation process. The most pronounced effect for small and morphologically complex structures emphasizes that the benefit of denoising is maximum precisely where the impact of noise has the greatest clinical consequences.

At the same time, it is important to emphasize that contouring, by its nature, involves a subjective component tied to the human factor. That is why, in this work, it is considered not an absolute metric for validation, but an additional clinically oriented quality indicator. However, it is this subjectivity that makes such an analysis clinically relevant, since it reflects the real convenience of the doctor's work with the image, the stability of interpretation and confidence in reproducing the boundaries of structures.

The importance of physically based noise modeling in k-space should be highlighted separately. The use of a spectral noise model enabled us to avoid non-physical artifacts characteristic of approaches that add noise directly in the image domain and to generate training data that are statistically closer to the real conditions of MRI reconstruction. This significantly reduced the gap between the training and clinical domains and improved the model's generalizability.

Taken together, the results of the study indicate that the proposed approach forms a new paradigm for MRI denoising, in which noise is considered not as a random impurity, but as a statistically described process integrated into the reconstruction model. This approach allows us to move from universal filtering strategies to adaptive, context-sensitive reconstruction models, which is fundamentally important for medical imaging with its high demands on structural accuracy and clinical interpretability.

CONCLUSIONS

In this paper, a comprehensive method for denoising MRI brain images is proposed that combines modern deep learning architectures with physically based noise modeling in k-space and a multi-level evaluation system. The developed FiLM-modulated Residual Attention U-Net model demonstrated a stable and significant improvement in both technical and clinically oriented image quality indicators compared to traditional denoising methods (NLM, BM3D) and common deep architectures (standard U-Net, Attention U-Net).

The key advantage of the approach is the explicit adaptation to the individual noise conditions of each image by integrating an 8-dimensional vector of statistical noise descriptors through the FiLM-modulation mechanism. This provides adaptive, frame-by-frame processing of slices, in contrast to models that implicitly generalize different noise regimes within a single latent space. Combined with residual blocks, CBAM, Attention Gate, and multiscale feature processing, the model effectively suppresses noise, preserving fine anatomical details, contours, and tissue structural organization critical for diagnostic interpretation.

The use of a synthetic noise model in k-space enabled us to create a training set that more closely matched real-world scanning conditions, reducing the gap between training and clinical data and increasing the model's generalizability and robustness when applied to data from different scanners and protocols.

Quantitative evaluation on synthetically noisy data showed a stable PSNR gain of approximately 20.7 dB and an increase in SSIM of approximately 0.73, with PSNR values stabilizing in the range of 35–45 dB after denoising. Analysis of the edge-preservation metric confirmed effective suppression of noise-induced pseudo-contours, with no signs of over-smoothing. On real clinical MRI images, the method demonstrated a systematic increase in SNR and a controlled decrease in the coefficient of variation, indicating physically correct signal stabilization without loss of natural textural heterogeneity of tissues. Clinically oriented validation by contouring anatomically complex structures (hippocampus, brainstem, visual chiasm) showed a stable improvement in segmentation quality: an increase in Dice Similarity Coefficient by 0.07–0.12 and a decrease in HD95 by 30–50%. This indicates increased reproducibility of structural boundaries, reduced contour uncertainty, and improved consistency of results, confirming the practical clinical value of denoised images in neuroimaging and radiotherapy planning tasks.

Overall, the proposed approach can be considered an adaptive, physically based MRI preprocessing tool that shifts the denoising process from universal filtering to statistically driven reconstruction. This is especially important in clinical scenarios where high structural accuracy, contour stability, and preservation of anatomically significant details are critical. Further research can focus on extending the model to multi-channel and multi-contrast MRI, integrating it with k-space reconstruction methods, and implementing it in clinical decision support systems for radiotherapy and neurodiagnostic.

Ethics Statement

The MRI images used in this study were obtained as part of standard clinical examinations according to routine diagnostic protocols. All data were anonymized prior to analysis, eliminating the possibility of patient identification during the study. The study was performed in accordance with generally accepted ethical principles for conducting scientific research using human medical data and in compliance with current institutional and national requirements for the use of retrospective clinical images for scientific purposes.

Data Availability

The MRI dataset used in this study contains clinical medical images and therefore cannot be made publicly available due to confidentiality requirements and institutional restrictions. Access to the data may be provided by the authors upon reasonable request and subject to approval by the relevant medical institution and compliance with applicable ethical and legal regulations.

Acknowledgements
The authors express their sincere gratitude to the radiologists of the Department of Radiology, National Cancer Institute, for their assistance in the contouring of anatomical structures used in the clinically oriented evaluation of the proposed method for denoising MRI images. Their professional experience and participation were essential for the clinical validation of the obtained results.

ORCID
D.G. Sliusarenko, https://orcid.org/0009-0009-1802-5859, **L.V. Sayan**, https://orcid.org/0009-0009-3797-9148;
A.V. Netreba, https://orcid.org/0000-0003-1347-3854

REFERENCES

[1] F. Lugauer, and J. Wetzl, "Magnetic Resonance Imaging," in: *Medical Imaging Systems: An Introductory Guide*, edited by A. Maier, S. Steidl, V. Christlein, and J. Hornegger, (Springer, Cham (CH), 2018). https://doi.org/10.1007/978-3-319-96520-8_6
[2] C.M. Sonderer, and N. Chen, "Improving the Accuracy, Quality, and Signal-To-Noise Ratio of MRI Parametric Mapping Using Rician Bias Correction and Parametric-Contrast-Matched Principal Component Analysis (PCM-PCA)," Yale J Biol Med **91**(3), 207–214 (2018). **PMCID**: PMC6153621
[3] W.A. Edelstein, G.H. Glover, C.J. Hardy, and R.W. Redington, "The intrinsic signal-to-noise ratio in NMR imaging," Magn Reson Med **3**(4), 604–618 (1986). https://doi.org/10.1002/mrm.1910030413
[4] H. Gudbjartsson, and S. Patz, "The Rician distribution of noisy MRI data," Magn. Reson. Med. **34**(6), 910–914 (1995). https://doi.org/10.1002/mrm.1910340618
[5] V. Prabhakaran, V.A. Nair, B.P. Austin, C. La, T.A. Gallagher, Y. Wu, D.G. McLaren, G. Xu, P. Turski, and H. Rowley, "Current Status and Future Perspectives of Magnetic Resonance High-Field Imaging: A Summary," Neuroimaging Clin. N. Am. **22**(2), 373–xii (2012). https://doi.org/10.1016/j.nic.2012.02.012
[6] K. Dabov, A. Foi, V. Katkovnik, and K. Egiazarian, "Image Denoising by Sparse 3-D Transform-Domain Collaborative Filtering," IEEE Transactions on Image Processing, **16**(8), 2080–2095 (2007). https://doi.org/10.1109/TIP.2007.901238
[7] M. Elad, B. Kawar, and G. Vaksman, "Image Denoising: The Deep Learning Revolution and Beyond—A Survey Paper," SIAM Journal on Imaging Sciences," **16**(13), 1594-1654 (2023). https://doi.org/10.1137/23M1545859
[8] S.W. Zamir, A. Arora, S. Khan, M. Hayat, F.S. Khan, M.-H. Yang, and L. Shao, "Learning Enriched Features for Real Image Restoration and Enhancement," in: *Computer Vision – ECCV 2020: 16th European Conference, Glasgow, UK, August 23–28, 2020, Proceedings, Part XXV*, (Springer-Verlag, Berlin, Heidelberg, 2020), pp. 492–511. https://doi.org/10.1007/978-3-030-58595-2_30
[9] J. Lehtinen, J. Munkberg, J. Hasselgren, S. Laine, T. Karras, M. Aittala, and T. Aila, "Noise2Noise: Learning image restoration without clean data," in: *35th International Conference on Machine Learning, ICML 2018*, (International Machine Learning Society, 2018), pp. 4620–4631. https://doi.org/10.48550/arXiv.1803.04189
[10] E. Perez, F. Strub, H. de Vries, V. Dumoulin, and A. Courville, "FiLM: visual reasoning with a general conditioning layer," in: *Proceedings of the Thirty-Second AAAI Conference on Artificial Intelligence and Thirtieth Innovative Applications of Artificial Intelligence Conference and Eighth AAAI Symposium on Educational Advances in Artificial Intelligence*, (AAAI Press, New Orleans, Louisiana, USA, 2018), pp. 3942–3951. https://doi.org/10.48550/arXiv.1709.07871
[11] O. Oktay, J. Schlemper, L.L. Folgoc, M. Lee, M. Heinrich, K. Misawa, K. Mori, S. McDonagh, N.Y. Hammerla, B. Kainz, B. Glocker, and D. Rueckert, "Attention U-Net: Learning Where to Look for the Pancreas," (2022). https://doi.org/10.48550/arXiv.1804.03999
[12] X. Chen, X. Wang, K. Zhang, K.-M. Fung, T.C. Thai, K. Moore, R.S. Mannel, H. Liu, B. Zheng, and Y. Qiu, "Recent advances and clinical applications of deep learning in medical image analysis," Medical Image Analysis **79**, 102444 (2022). https://doi.org/10.1016/j.media.2022.102444
[13] R. Ayde, M. Vornehm, Y. Zhao, F. Knoll, E.X. Wu, and M. Sarracanie, "MRI at low field: A review of software solutions for improving SNR," NMR Biomed, **38**(1), e5268 (2025). https://doi.org/10.1002/nbm.5268
[14] M. Safari, S. Wang, Z. Eidex, R. Qiu, C.-W. Chang, D.S. Yu, and X. Yang, "A Physics-Informed Deep Learning Model for MRI Brain Motion Correction," ArXiv, arXiv:2502.09296v1 (2025). https://doi.org/10.1002/mp.70197
[15] L. Han, S. Xiao, M. Li, J. Liu, and X. Zhou, "Noise-Controllable Complex-Valued Diffusion Model for k-Space Data of Hyperpolarized ^{129}Xe Lung MRI Generation," in: *Medical Image Computing and Computer Assisted Intervention – MICCAI 2025*, edited by J.C. Gee, D.C. Alexander, J. Hong, J.E. Iglesias, C.H. Sudre, A. Venkataraman, P. Golland, J.H. Kim, and J. Park, (Springer Nature Switzerland, Cham, 2026), pp. 360–369. https://doi.org/10.1007/978-3-032-05127-1_35
[16] C. Ciulla, "Two-dimensional image noise removal and reconstruction using discrete Fourier transform, k-space filtering and Z-space filtering," Progress in Engineering Science, **2**(1), 100056 (2025). https://doi.org/10.1016/j.pes.2025.100056
[17] T. Song, F. Nie, Y. Guo, F. Xu, and S. Zhang, "FilterDiff: Noise-Free Frequency-Domain Diffusion Models for Accelerated MRI Reconstruction," in: *Medical Image Computing and Computer Assisted Intervention – MICCAI 2025*, edited by J.C. Gee, D.C. Alexander, J. Hong, J.E. Iglesias, C.H. Sudre, A. Venkataraman, P. Golland, J.H. Kim, and J. Park, (Springer Nature Switzerland, Cham, 2026), pp. 205–215. https://doi.org/10.1007/978-3-032-05325-1_20
[18] W. Zhang, Y. Guo, and Q. Jin, "Radiomics and Its Feature Selection: A Review," Symmetry, **15**(10), 1834 (2023). https://doi.org/10.3390/sym15101834
[19] M. Shakeri, A. Mostaar, A.Z. Sadeghi, S.M. Hosseini, A.Y. Joybari, and H. Ghadiri, "A Comprehensive Evaluation of Radiomic Features in Normal Brain Magnetic Resonance Imaging: Investigating Robustness and Region Variations," J. Med. Phys. **49**(4), 608–622 (2024). https://doi.org/10.4103/jmp.jmp_149_24
[20] M. Dohmen, M.A. Klemens, I.M. Baltruschat, T. Truong, and M. Lenga, "Similarity and quality metrics for MR image-to-image translation," Sci. Rep. **15**(1), 3853 (2025). https://doi.org/10.1038/s41598-025-87358-0
[21] "The Image Biomarker Standardization Initiative: Standardized Quantitative Radiomics for High-Throughput Image-based Phenotyping," Radiology," **295**(2), (2020). https://doi.org/10.1148/radiol.2020191145
[22] D. Sliusarenko, and A. Netreba, "Phantom-Guided Adaptive Denoising of Medical Images Using Enhanced U-Net Architecture," Radioelectronics and Communications Systems, (2025). https://doi.org/10.3103/S0735272725020049
[23] M. Mathieu, C. Couprie, and Y. LeCun, "Deep multi-scale video prediction beyond mean square error," CoRR, (2015). https://doi.org/10.48550/arXiv.1511.05440

[24] P. Isola, J.-Y. Zhu, T. Zhou, and A.A. Efros, "Image-to-Image Translation with Conditional Adversarial Networks," in: *2017 IEEE Conference on Computer Vision and Pattern Recognition (CVPR)*, (2017), pp. 5967–5976. https://doi.org/10.1109/CVPR.2017.632
[25] D. Sliusarenko, A. Netreba, and S. Radchenko, "Refining Clarity Medical Image via U-Net with Tailored Architectural Modifications and Transfer Learning," in: *Proc. IEEE Int. Conf. Electron. Nanotechnol., ELNANO.*, (Institute of Electrical and Electronics Engineers, 2024), pp. 456–460. https://doi.org/10.1109/ELNANO63394.2024.10756858
[26] H. Liu, Z. Li, S. Lin, and L. Cheng, "A Residual UNet Denoising Network Based on Multi-Scale Feature Extraction and Attention-Guided Filter," Sensors (Basel), **23**(16), 7044 (2023). https://doi.org/10.3390/s23167044
[27] H. Zhang, Q. Lian, J. Zhao, Y. Wang, Y. Yang, and S. Feng, "RatUNet: residual U-Net based on attention mechanism for image denoising," PeerJ Comput. Sci. **8**, e970 (2022). https://doi.org/10.7717/peerj-cs.970
[28] Z. Zhuang, M. Liu, A. Cutkosky, and F. Orabona, "Understanding AdamW through Proximal Methods and Scale-Freeness," Trans. Mach. Learn. Res. (2022). https://doi.org/10.48550/arXiv.2202.00089
[29] S. Brody, U. Alon, and E. Yahav, "On the Expressivity Role of LayerNorm in Transformers' Attention," (arXiv, 2023). https://doi.org/10.48550/arXiv.2305.02582
[30] T.-T. Han, H. Nguyen Van, and P. Nguyen Huu, "Denoising Method for MRI Images Using Modified BM3D Filter with Complex Network and Artificial Neural Networks," Journal of Electrical and Computer Engineering, **2024**(1), 2606485 (2024). https://doi.org/10.1155/2024/2606485
[31] Z. Wang, A.C. Bovik, H.R. Sheikh, and E.P. Simoncelli, "Image quality assessment: from error visibility to structural similarity," IEEE Transactions on Image Processing, **13**(4), 600–612 (2004). https://doi.org/10.1109/TIP.2003.819861
[32] M.J. Kobra, M.O. Rahman, and A.M. Nakib, "A Novel Hybrid Framework for Noise Estimation in High-Texture Images using Markov, MLE, and CNN Approaches," Scientific Journal of Engineering Research, **1**(2), 54–63 (2025). https://doi.org/10.64539/sjer.v1i2.2025.25
[33] H.M.S.S. Herath, H.M.K.K.M.B. Herath, N. Madusanka, and B.-I. Lee, "A Systematic Review of Medical Image Quality Assessment," Journal of Imaging, **11**(4), 100 (2025). https://doi.org/10.3390/jimaging11040100
[34] R. Rodrigues, L. Lévêque, J. Gutiérrez, H. Jebbari, M. Outtas, L. Zhang, A. Chetouani, S. Al-Juboori, M.G. Martini, and A.M.G. Pinheiro, "Objective quality assessment of medical images and videos: review and challenges," Multimed Tools Appl **84**(25), 29915–29948 (2025). https://doi.org/10.1007/s11042-024-20292-x
[35] K.M. Kempski, M.T. Graham, M.R. Gubbi, T. Palmer, and M.A. Lediju Bell, "Application of the generalized contrast-to-noise ratio to assess photoacoustic image quality," Biomed. Opt. Express, **11**(7), 3684–3698 (2020). https://doi.org/10.1364/BOE.391026
[36] O. Rainio, and R. Klén, "Modified Dice Coefficients for Evaluation of Tumor Segmentation from PET Images: A Proof-of-Concept Study," J. Digit. Imaging. Inform. Med. (2025). https://doi.org/10.1007/s10278-025-01535-1
[37] P. Ramachandran, T. Eswarlal, M. Lehman, and Z. Colbert, "Assessment of Optimizers and their Performance in Autosegmenting Lung Tumors," J. Med. Phys. **48**(2), 129–135 (2023). https://doi.org/10.4103/jmp.jmp_54_23
[38] A. Mason, J. Rioux, S.E. Clarke, A. Costa, M. Schmidt, V. Keough, T. Huynh, and S. Beyea, "Comparison of Objective Image Quality Metrics to Expert Radiologists' Scoring of Diagnostic Quality of MR Images," IEEE Transactions on Medical Imaging, **39**(4), 1064–1072 (2020). https://doi.org/10.1109/TMI.2019.2930338
[39] K. Chupetlovska, K. Groot Lipman, Z. Bodalal, F.M. Aricò, L. Topff, M. Maas, and S. Trebeschi, "Do's and don'ts of tumor segmentation with 3D slicer: A practical guide for radiologists, by radiologists," European Journal of Radiology Artificial Intelligence, **5**, 100053 (2026). https://doi.org/10.1016/j.ejrai.2025.100053
[40] A. Buades, B. Coll, and J.-M. Morel, "A non-local algorithm for image denoising," in *2005 IEEE Computer Society Conference on Computer Vision and Pattern Recognition (CVPR'05)*, (2005), pp. 60–65 vol. 2. https://doi.org/10.1109/CVPR.2005.38
[41] K. Zhang, W. Zuo, Y. Chen, D. Meng, and L. Zhang, "Beyond a Gaussian Denoiser: Residual Learning of Deep CNN for Image Denoising," IEEE Transactions on Image Processing, **26**(7), 3142–3155 (2017). https://doi.org/10.1109/TIP.2017.2662206
[42] Q. Yang, P. Yan, Y. Zhang, H. Yu, Y. Shi, X. Mou, M.K. Kalra, Y. Zhang, L. Sun, and G. Wang, "Low Dose CT Image Denoising Using a Generative Adversarial Network with Wasserstein Distance and Perceptual Loss," IEEE Trans Med Imaging, **37**(6), 1348–1357 (2018). https://doi.org/10.1109/TMI.2018.2827462

СТАТИСТИЧНО ОБУМОВЛЕНЕ ШУМОЗАГЛУШЕННЯ МРТ ЗА ДОПОМОГОЮ АРХІТЕКТУРИ RESIDUAL ATTENTION U-NET З FILM-МОДУЛЯЦІЄЮ

Д.Г. Слюсаренко[1,2], Л.В. Саян[2], А.В. Нетреба[1]
[1]Факультет радіофізики, електроніки та комп'ютерних систем, Київський національний університет імені Тараса Шевченка, вул. Володимирська, 64/13, Київ, Україна, 01601
[2]Національний інститут раку України, вул. Юлія Здановського, 33/43, Київ, Україна, 03022

Якість зображень МРТ часто обмежується просторово неоднорідним шумом, що негативно впливає на точність клінічної інтерпретації та автоматичного аналізу. Традиційні методи глибокого навчання часто враховують шум неявно, що призводить до надмірного згладжування та втрати дрібних анатомічних структур. У цій статті ми пропонуємо архітектуру покращеного шумозаглушення U-Net, яка використовує механізм лінійної модуляції за ознаками (FiLM) для динамічної адаптації до профілю шуму кожного зрізу. Модель поєднує вектор з 8 статистичних дескрипторів (включаючи характеристики інтенсивності, текстури та частоти), що дозволяє динамічно керувати внутрішніми представленнями мережі залежно від конкретних умов сканування. Для підвищення фізичної коректності навчання проводилося на даних із синтетично згенерованим шумом у k-просторі. Архітектура вдосконалена за допомогою блоків залишків, механізмів уваги та багатомасштабного модуля обробки. На синтетичних даних середнє покращення пікового співвідношення сигнал/шум (PSNR) становило ≈ 20,7 дБ, а середнє покращення індексу структурної подібності (SSIM) – приблизно 0,73, що свідчить про глибоке відновлення структурної інформації. На клінічних зображеннях спостерігалося збільшення співвідношення сигнал/шум (SNR) та стабілізація коефіцієнта варіації (CV), що підтверджує фізичну коректність методу. Клінічна валідація на складних контурних структурах (гіпокамп, стовбур мозку, зоровий хіазм) показала збільшення коефіцієнта Дайса (DSC) на 0,07–0,12 та зменшення похибки HD95 на 30–50%. Запропонований метод дозволяє перейти від універсальних стратегій шумозаглушення до адаптивної реконструкції, забезпечуючи високу точність збереження анатомічних меж. Це робить його перспективним інструментом для обробки МРТ у задачах нейровізуалізації та планування варіативної терапії.

Ключові слова: *МРТ; Attention U-Net; FiLM; медична візуалізація; реконструкція; шум; CNN; контурування*

East European Journal of Physics. 2. 578-583 (2026)
DOI:10.26565/2312-4334-2026-2-64 ISSN 2312-4334

SPECTROSCOPIC STUDY OF THE INTERACTIONS OF METAL IONS AND PROTEINS WITH BENZANTHRONE DERIVATIVES

E. Romanovska-Dzalbe[1], O. Zhytniakivska[2]*, U. Malovytsia[2], E. Kirilova[1], A. Pučkins[1], R. Fridmans[1], S. Osipovs[1], V. Trusova[2], G. Gorbenko[2]
[1]Institute of Life Sciences and Technology, Daugavpils University, LV-5401 Daugavpils, Latvia
[2]Department of Medical Physics and Biomedical Nanotechnologies, V.N. Karazin Kharkiv National University
4 Svobody Sq., Kharkiv, 61022, Ukraine
**Corresponding Author email: olga.zhytniakivska@karazin.ua*
Received February 25, 2026; revised April 26; accepted May 10, 2026

The present work describes the characterization of complexes between various metals and three benzanthrone derivatives bearing structurally similar substituents. Within this investigation, the obtained complexes were meticulously examined using spectroscopic techniques. The absorption spectra of solutions of the obtained complexes in the UV-visible region showed a small bathochromic or hypsochromic shift in the visible region compared to the initial compounds. In the emission spectra of these complexes, significant changes in the positions and intensities of the fluorescence bands were observed as a function of the dyes' chemical structures. Interaction with metal ions in the presence of β-lactoglobulin amyloid fibrils showed metal-specific effects, including fluorescence enhancement with Zn^{2+} and pronounced quenching with Cu^{2+}, suggesting a combined contribution of dye–metal and fibril–metal interactions. These findings highlight the potential of benzanthrone derivatives, both free and fibril-bound, as sensitive and selective fluorescent probes for heavy metal detection, providing a foundation for the development of hybrid biomaterial-based sensing platforms.
Keywords: *Benzanthrone dyes; Metal complex; Optical spectroscopy; β-lactoglobulin*
PACS: 87.14.C++c, 87.16.Dg

With the expansion of industrial and agricultural activities and the consequent direct and indirect anthropogenic impacts on the environment, heavy metals have emerged as a global concern due to their contamination of aquatic systems, soils, and other ecosystems, posing significant environmental and health risks. Previous studies have identified Zn, Pb, Hg, Cr, and Cd as exhibiting notable toxicity and potential ecological hazards [1]. In particular, Pb^{2+}, Cr^{3+}, and Cd^{2+} ions are associated with prolonged detrimental effects on human health and environmental quality [2]. While certain heavy metals play essential roles in biochemical processes at trace levels, elevated concentrations can pose significant risks to human health [3,4].

Chemical sensors play a vital role as devices designed to detect, measure, and monitor specific chemical compounds in a given environment, providing critical data for a wide range of scientific, industrial, medical, and environmental applications [5-7]. These sensors operate by interacting with a sensing material that generates a signal interpreted to determine the concentration of the target compound. Their ability to detect analytes at minimal concentrations has led to their widespread use in areas such as environmental monitoring, clinical diagnostics, food safety, and the pharmaceutical industry. As demand for accurate and reliable data in these areas grows, the development of highly selective sensors has become a research priority.

The rapid advancement of fluorescent probe technology enables faster and more efficient real-time detection of important molecules and ions in complex matrices. The advancement of contemporary science also increasingly highlights the need for comprehensive investigation of biologically relevant small molecules, biomarkers, and proteins. This demand has stimulated the development of biosensors capable of selectively recognizing cellular and biomolecular targets. The investigation of biologically significant proteins increasingly requires the development of novel and highly efficient fluorescent probes. In particular, real-time monitoring of β-lactoglobulin is of considerable importance due to its extensive application in the modern food and beverage industry [8,9].

Therefore, the development of sensitive and selective methods for heavy metal detection is critical to effective environmental monitoring. Benzanthrone derivatives exhibit strong potential as heavy-metal sensors for environmental monitoring owing to their multifunctional characteristics, including broad fluorescence emission and high photostability [10,11]. In this study, we evaluate the sensitivity of benzanthrone-based fluorescent dyes for detecting Cu^{2+}, Zn^{2+}, Ni^{2+}, and Pb^{2+} ions, and investigate the interactions between the dye molecules and β-lactoglobulin fibrils.

METHODS

Materials

Bovine β-lactoglobulin (βlg), copper (II) chloride dihydrate, nickel (II) chloride, lead (II) nitrate, and zinc chloride were purchased from Sigma, USA. Benzanthrone dyes A, B, and C (see Fig. 1) were synthesized by previously described procedures [12-14]. All other reagents were of analytical grade and used without further purification.

Cite as: E. Romanovska-Dzalbe, O. Zhytniakivska, U. Malovytsia, E. Kirilova, A. Pučkins, R. Fridmans, S. Osipovs, V. Trusova, G. Gorbenko, East Eur. J. Phys. 2, 578 (2026), https://doi.org/10.26565/2312-4334-2026-2-64

Preparation of working solutions

The absorption and steady-state fluorescence measurements were carried out in ethanol. Dye concentration was 32 µM and 23 µM for the absorbance and fluorescence measurements, respectively. Heavy metal concentration was 414,3 µM.

The β-lactoglobulin stock solutions 10 mg/ml (βlgF) was prepared in distilled water with HCl (pH 2.0). The protein (stock solutions) fibrillization reaction was conducted at 90°C for 2 days. The working solutions of protein were prepared by dissolving a stock solution of the fibrillar β-lactoglobulin in distilled water (pH 6.07). The fluorometric measurements were carried out in distilled water (pH 6.07).

Spectroscopic measurements

The absorption and steady-state fluorescence spectra were recorded using a Shimadzu UV-2600 spectrophotometer and an RF-6000 spectrofluorimeter (Shimadzu, Japan) at 25°C. All measurements were conducted in 10-mm path-length quartz cuvettes.

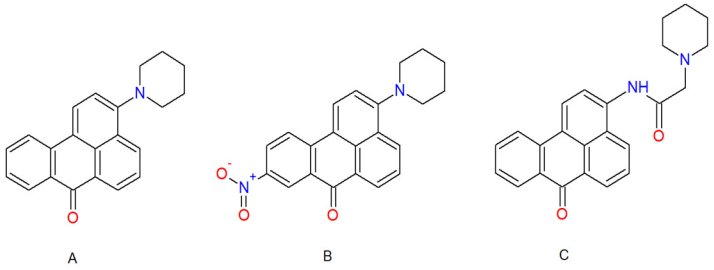

Figure 1. Structure of studied dyes A, B, C.

RESULTS AND DISCUSSION

Our previous studies have shown that amidine derivatives of benzanthrone tend to form complexes with chromium ions [15], and amino derivatives of benzanthrone form complexes with heavy metal ions, showing pronounced spectral changes in solution upon binding of Cu^{2+}, Zn^{2+}, Ni^{2+} and Pb^{2+} [16].

In this study three highly luminescent benzanthrone derivatives A, B, C were used for study of complexation with copper (II), nickel (II) lead (II), and zinc ions. All substances have benzanthrone residue with a piperidine moiety.

In the initial phase of our study, we evaluated dye's ability to detect heavy metal ions. The absorption spectrum of the dye A shows a band in the UV-visible region at 460 nm; the ethanol solutions of the obtained complexes with metal ions showed a bathochromic shift of 10-30 nm from the initial compound (see Fig. 2).

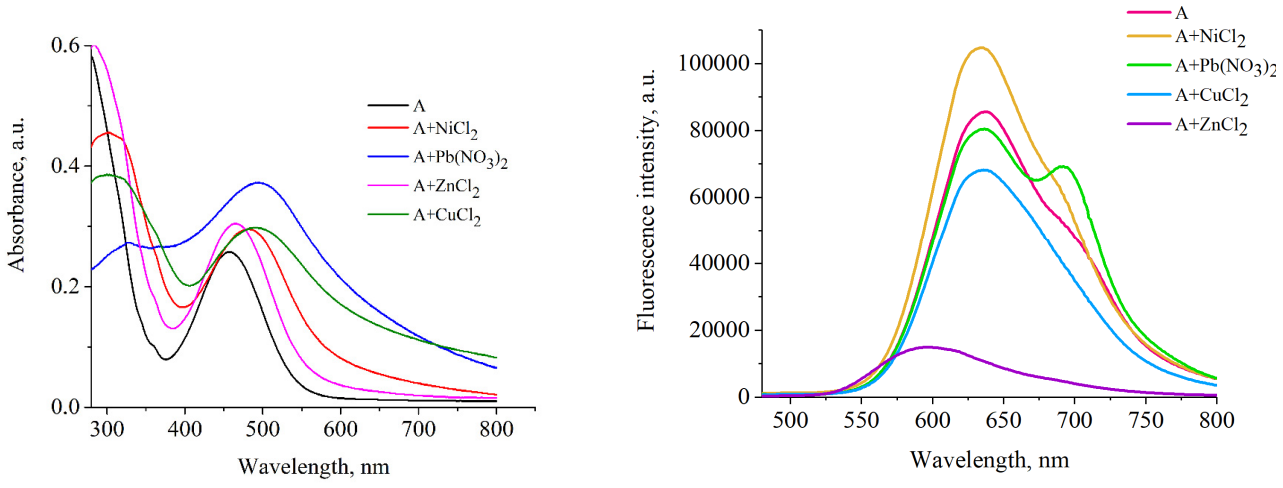

Figure 2. Absorption (left) and emission spectra (right) of dye A in the presence of heavy metal ions. Concentrations of 32 µM and 23 µM were used for absorbance and fluorescence measurements, respectively

The dye A displays a broad emission spectrum with a prominent peak at 630 nm and a shoulder at approximately 700 nm. Upon binding to Ni^{2+} ions, the emission band at 700 nm of dye A diminishes, while the fluorescence around 630 nm increases by approximately 1.3-fold. In contrast, exposure to Pb^{2+}, Cu^{2+}, and Zn^{2+} leads to a decrease in overall fluorescence intensity, with Zn^{2+} producing the most pronounced effect—over sixfold quenching of the 630 nm band—indicating a particularly strong affinity of dye A for zinc ions. The observed shifts in emission peaks are likely due to the formation of metal–ligand charge-transfer complexes, involving electron transfer from the metal ions to nitrogen- and oxygen-containing groups within the dye. Interestingly, the absorption spectrum of dye A shows minimal changes

upon complexation with Zn^{2+}, suggesting that the interaction primarily involves the electron transfer switching moiety, which modulates fluorescence without significantly perturbing the fluorophore's ground-state electronic structure [17]. To explore the influence of electron-withdrawing substituents on metal binding and electron transfer modulation, a derivative of dye A (dye B) containing a nitro group was synthesized, and its spectral behaviour in the presence of metal ions was investigated.

The spectral study of the dye B shows an absorption band at 468 nm and a broad emission peak at 657 nm in ethanol. Unlike dye A, derivative B does not change the position of absorption and fluorescence maxima in the presence of metal ions (see Table 1 and Fig. 3). Binding with metal ions results in about a 1.3-fold reduction in fluorescence intensity. Thus, dye B exhibits a lower affinity for metal ions than dye A. Notably, dye B shows an even lower affinity for metal ions than the compound without a nitro group. Apparently, the presence of the nitro group causes a redistribution of electron density that ultimately hinders intracomplex charge transfer.

Table 1. The basic photophysical characteristics of benzanthrone dyes binding with metal ions.

	Dye A				Dye B				Dye C			
	λ_A, nm	I, a.u.	λ_F, nm	I, a.u.	λ_A, nm	I, a.u.	λ_F, nm	I, a.u.	λ_A, nm	I, a.u.	λ_F, nm	I, a.u.
Dye	457	0.28	636	85441	468	0.3810	657	18945	423	0.2426	566 687	14360 16350
Ni^{2+}	484	0.29	634	103930	468	0.3563	657	14540	420	0.2513	548	44780
Cu^{2+}	495	0.29			468	0.3454	657	14220	407	0.2592	543	83500
Zn^{2+}	488	0.301	598	14878	468	0.3492	657	14400	423	0.2435	557 682	21670 15980
Pb^{2+}	517	0.37	635 693	80087 69349	468	0.3478	657	14170	417	0.2399	544	103900

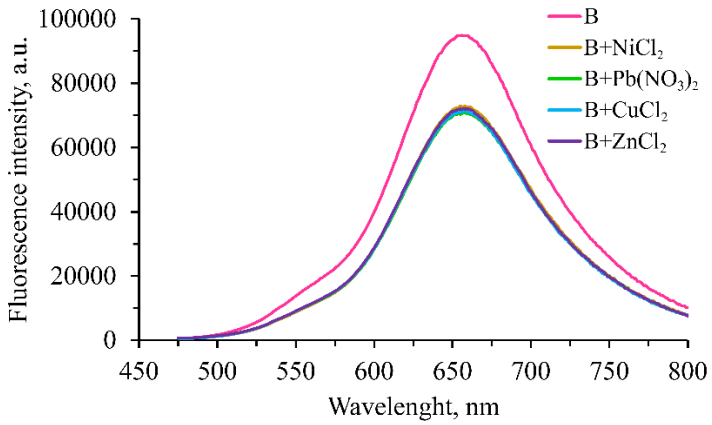

Figure 3. Emission spectra of dye B in the presence of heavy metal ions. Concentration of 23 μM was used for fluorescence measurements

The next object of study was a derivative of benzanthrone in which the piperidine ring is attached to benzanthrone via an acetylamide group (dye C). Such a structure with additional nitrogen and oxygen atoms should presumably facilitate the possible complexation of the dye and metal ions. The performed spectral study confirms this assumption. Observed changes in the absorption and luminescence spectra confirm the formation of complexes between dye C molecules and metal ions. In particular, binding to Ni^{2+}, Cu^{2+} and Pb^{2+} results in a hypsochromic shift of the absorption band by 3–16 nm compared to the free ligand C.

Even more pronounced changes are observed in the luminescence spectra. The dye C displays a broad emission spectrum with a two broad peaks at 566 nm and 687 nm (see Fig. 4). When this dye binds to metal ions, the emission at 566 nm is enhanced, while the band at 687 nm is weakened and disappears completely in the presence of copper and lead ions. Dye C exhibits the highest affinity for lead ions, which is confirmed by a significant increase in fluorescence (more than 7 times). Apparently, when interacting with dye molecules, Pb^{2+} ions stabilize the excited state of the dye, reducing nonradiative decay and leading to high emission intensity at a wavelength of 544 nm.

In recent decades, protein-derived nanomaterials have attracted growing interest as versatile platforms for heavy metal remediation, driven by the chemical diversity of amino acid side chains and their inherent ability to self-assemble into well-defined supramolecular architectures, including fibrillar networks, hydrogels, and nanoscale condensates [18-22]. For instance, hydrogels derived from soy protein have demonstrated selective removal of Cu(II) even in the presence of competing ions [20]. Particularly promising are composite filtration membranes that combine activated carbon with amyloid fibrils obtained from proteins such as β-lactoglobulin or soy protein. These hybrid systems have been shown to efficiently remove a wide range of metal ions—including Au, Hg, Pb, Pd, As, Cr, and Ni—from both

model solutions and real wastewater streams [18–23]. Beyond their established adsorption performance, amyloid fibrils exhibit outstanding mechanical stability, high specific surface area, and a dense distribution of functional binding sites, rendering them highly suitable scaffolds for post-functionalization. Despite these advantageous properties, the incorporation of amyloid fibril architectures with fluorescent probes for heavy metal ion sensing remains largely unexplored. Integrating these two approaches could enable the development of hybrid sensing platforms that combine the adsorption capacity and structural robustness of amyloid frameworks with the high sensitivity of fluorescence-based detection. Achieving this, however, requires a detailed understanding of fluorophore–metal interactions as well as the binding mechanisms between metal ions and β-lactoglobulin amyloid fibrils.

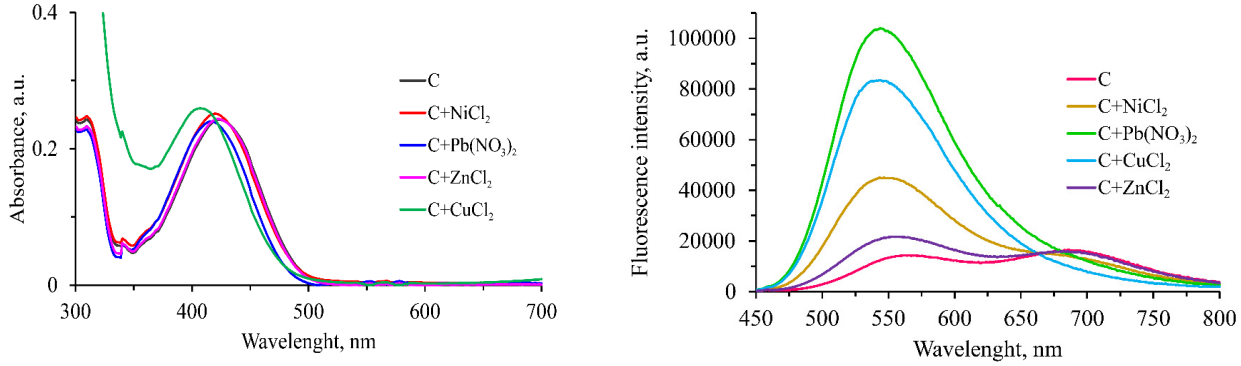

Figure 4. Absorption (left) and emission spectra (right) of dye C in the presence of heavy metal ions. Concentrations of 32 µM and 23 µM were used for absorbance and fluorescence measurements, respectively

Therefore, in the next phase of our study, we investigated the sensitivity of dye A to heavy metal ions in the presence of β-lactoglobulin amyloid fibrils (β-lgF). Fig. 5 illustrates the emission spectra of dye A in systems containing β-lgF (Fig. 5A) and β-lgF +heavy metals (Fig. 5B). As shown in Fig. 5, the free dye in aqueous solution exhibits an emission maximum at 636 nm. Upon addition of fibrillar β-lactoglobulin to dye A in water, a pronounced enhancement in fluorescence intensity was observed, together with an approximately 25 nm hypsochromic shift of the emission maximum, consistent with dye relocation into a more hydrophobic fibrillar environment. The introduction of heavy metal ions modulated the fluorescence intensity of this band in a metal-specific manner. In particular, the addition of Ni^{2+} and Pb^{2+} produced no significant changes in either the emission maximum or the overall fluorescence intensity. In contrast, relative to the dye A–β-lgF system, the presence of Zn^{2+} led to an enhancement in fluorescence intensity, whereas the addition of Cu^{2+} produced a pronounced quenching of the emission. A plausible explanation for these observations is that the metal ions interact simultaneously with the dye and the amyloid fibril scaffold, thereby modifying the local microenvironment surrounding dye A and influencing its photophysical behaviour.

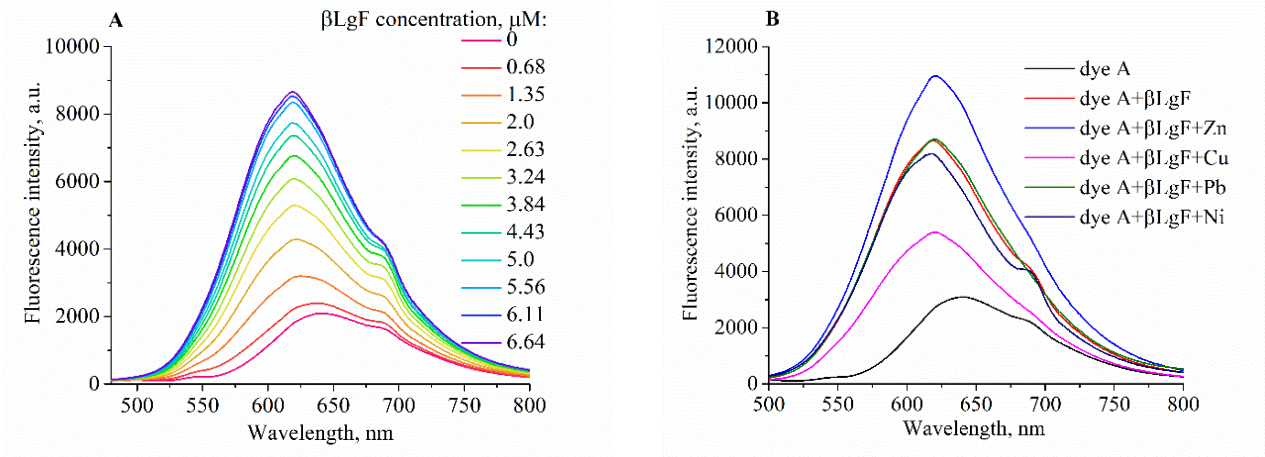

Figure 5. Emission spectra of dye A in the presence of β- lactoglobulin amyloid fibrils (A) and in the systems containing β-lgF and metal ions (B). Dye A concentration was 1 µM

Additionally, differences in metal ion coordination chemistry and binding strength likely contribute to the observed metal-specific effects. Peydayesh et al. [22] reported that the adsorption of chromium, nickel, silver, and platinum ions onto β-lactoglobulin amyloid fibrils is highly exothermic and strongly ion-specific, highlighting the complex and selective nature of these interactions. As can be seen from Fig. 5B, in the presence of Ni^{2+} and Pb^{2+}, no significant changes in emission maximum or intensity are observed. This suggests that these ions likely bind to fibrillar sites located away from the dye and therefore have minimal impact on the local microenvironment of the fibril-bound fluorophore or on the efficiency of the electron transfer process. Moreover, Fan et al. showed that β-lactoglobulin

amyloid fibrils exhibit a notably higher adsorption capacity for Cu^{2+} compared to Ni^{2+} [24]. Cu^{2+} is a paramagnetic d^9 ion capable of facilitating photoinduced electron transfer, enhanced intersystem crossing, and static or dynamic quenching when coordinated near the dye [25-27]. Its strong affinity for amyloid fibrils likely positions Cu^{2+} in close proximity to the dye, facilitating quenching of the dye's fluorescence. Similar quenching phenomena have been reported for other PET-active dyes, such as rhodamine B and naphthalimide derivatives, where proximity of Cu^{2+} leads to effective suppression of emission via both static and dynamic quenching mechanisms [26-29].

CONCLUSIONS

The results show that two of the studied benzanthrone dyes exhibit metal-specific fluorescence responses in ethanol solutions. In particular, dyes A and C undergo pronounced spectral changes in ethanol solution upon binding Cu^{2+}, Zn^{2+}, Ni^{2+}, and Pb^{2}. It was found that binding dye A to Cu^{2+}, Zn^{2+}, and Pb^{2+} ions leads to fluorescence quenching, whereas complexation of dye C with metal ions leads to increased emission. In contrast, compound B with a nitro group demonstrates a lower affinity for metal ions. The results indicate that benzanthrone dyes interact specifically with metal ions in the presence of β-lactoglobulin amyloid fibrils, exhibiting effects characteristic of each metal, including enhanced fluorescence with Zn^{2+} and pronounced quenching with Cu^{2+}. These results demonstrate the potential of using benzanthrone derivatives as sensitive and selective fluorescent probes for heavy metal detection, laying the foundation for the development of biomolecular-based hybrid sensing platforms.

Acknowledgements

This work was supported by the Ministry of Education and Science of Ukraine (the project "Development of economically affordable nanosystems for rapid identification and purification of water from heavy metal ions based on carbon nanoallotropes and amyloids from organic waste" No. 0124U000968) and the Latvian Council of Science. Project No. lzp-2022/1-0436 "Novel fluorescent anthrone-derived functional materials for bioimaging applications".

ORCID

E. Romanovska-Dzalbe, https://orcid.org/0009-0002-4014-4570; **Olga Zhytniakivska,** https://orcid.org/0000-0002-2068-5823;
Uliana Malovytsia, https://orcid.org/0000-0002-7677-0779; **Elena Kirilova,** https://orcid.org/0000-0002-9577-5612;
Aleksandrs Pučkins, https://orcid.org/0000-0001-9006-0493; **Sergejs Osipovs,** https://orcid.org/0000-0002-3875-1331;
Valeriya Trusova, https://orcid.org/0000-0002-7087-071X; **Galyna Gorbenko,** https://orcid.org/0000-0002-0954-5053

REFERENCES

[1] E.Y. Ouardi, A. Giove, M. Laatikainen, C. Branger, and K. Laatikainen, J. Environ. Chem. Eng. **9**, 106548 (2021). https://doi.org/10.1016/j.jece.2021.106548
[2] K. Renu, R. Chakraborty, H. Myakala, R. Koti, A.C. Famurewa, H. Madhyastha, B. Vellingiri, *et al*., Chemosphere, **271**, 129735 (2021). https://doi.org/10.1016/j.chemosphere.2021.129735
[3] C. Ariño, N. Serrano, J.M. Díaz-Cruz, and M. Esteban, Anal. Chim. Acta, **990**, 11 (2017). https://doi.org/10.1016/j.aca.2017.08.016
[4] L. Li, S. Xu, X. Li, H. Gao, L. Yang, and C. Jiang, Chem. Eng. J. **493**, 152636 (2024). https://doi.org/10.1016/j.cej.2024.152636
[5] M. R. Willner, and P. J. Vikesland, J. Nanobiotechnol. **16**, 95 (2018). https://doi.org/10.1186/s12951-018-0404-1
[6] C. Qu, H. Li, S. Zhou, G. Li, C. Wang, R. Snyders, C. Bittencourt, and W. Li, Chemosensors, **9**, 190 (2021). https://doi.org/10.3390/chemosensors9070190
[7] P.C. Wanniarachchi, K.G. Upul Kumarasinghe, and C. Jayathilake, Food Chem. **436**, 137733 (2024). https://doi.org/10.1016/j.foodchem.2023.137733
[8] G. Chakraborty, A.K. Ray, P.K. Singh, and H. Pal, Sens. Actuators B Chem. **327**, 128864 (2021). https://doi.org/10.1016/j.snb.2020.128864
[9] D.E.W. Chatterton, G. Smithers, P. Roupas, and A. Brodkorb, Int. Dairy J. **16**, 1229 (2006). https://doi.org/10.1016/j.idairyj.2005.10.008
[10] A. Maļeckis, and E. Romanovska-Dzalbe, Chem. Pap. **79**, 3463 (2025). https://doi.org/10.1007/s11696-025-04123-0
[11] M.B. Patel, V.A. Trivedi, R.C. Dabhi, J.J. Maru, and Z.M. Patel, Mini-Rev. Org. Chem. **22**, e18756298330235 (2024). https://doi.org/10.2174/0115734066298330240215051646
[12] E.M. Kirilova, I.A. Meirovics, and S.V. Belyakov, Chem. Heterocycl. Compd. **38**, 789 (2002). https://doi.org/10.1023/A:1020983720281
[13] A. Maļeckis, M. Cvetinska, A. Puckins, S. Osipovs, J. Sirokova, S. Belyakov, and E. Kirilova, Molecules, **28**, 5171 (2023). https://doi.org/10.3390/molecules28135171
[14] E.M. Kirilova, I.D. Nikolaeva, E. Romanovska, A.I. Puckins, and S.V. Belyakov, Chem. Heterocycl. Compd. **56**, 192 (2020). https://doi.org/10.1007/s10593-020-02653-8
[15] E. Kirilova, A. Bulanovs, A. Puckins, E. Romanovska, and G. Kirilov, Polyhedron, **157**, 107 (2019). https://doi.org/10.1016/j.poly.2018.10.040
[16] U. Malovytsia, O. Zhytniakivska, K. Yeltsov, K. Vus, V. Trusova, E. Kirilova, and G. Gorbenko, East Eur. J. Phys. (3), 523 (2025). https://doi.org/10.26565/2312-4334-2025-3-57
[17] L. Zhu, Z. Yuan, J. T. Simmons, and K. Sreenath, RSC Adv. **4**, 20398 (2014). https://doi.org/10.1039/C4RA00610A
[18] J. Liu, D. Su, J. Yao, Y. Huang, J. Shao, and X. Chen, J. Mater. Chem. A, **5**, 4163 (2017). https://doi.org/10.1039/C6TA09858G
[19] X. Yu, W. Liu, X. Deng, S. Yan, and Z. Su, Chem. Eng. J. **335**, 176 (2017). https://doi.org/10.1016/j.cej.2017.10.121
[20] J. Kostal, A. Mulchandani, and W. Chen, Macromolecules, **34**, 2257 (2001). https://doi.org/10.1021/ma001973m
[21] S. Bolisetty, and R. Mezzenga, Nat. Nanotechnol. **11**, 365 (2016). https://doi.org/10.1038/nnano.2015.310

[22] M. Peydayesh, S. Bolisetty, T. Mohammadi, and R. Mezzenga, Langmuir, **35**, 6035 (2019). https://doi.org/10.1021/acs.langmuir.8b04234
[23] L.C. Ramírez-Rodríguez, L.E. Díaz Barrera, M.X. Quintanilla-Carvajal, *et al*., Membranes, **10**, 386 (2020). https://doi.org/10.3390/membranes10120386
[24] Y. Fu, L. Han, Q. Zhang, R. Liu, and C. Hu, Chemosphere, **297**, 134241 (2022). https://doi.org/10.1016/j.chemosphere.2022.134241
[25] J.R. Lakowicz, *Principles of Fluorescence Spectroscopy*, 3rd ed. (Springer, New York, 2006).
[26] G. Li, W. Li, L. Zhang, B. Liu, and Y. Li, Dalton Trans. **42**, 1827 (2013). https://doi.org/10.1039/C2DT32156A
[27] N. Ahmed, W. Zareen, D. Zhang, X. Yang, and Y. Ye, J. Fluoresc. **30**, 1171 (2020). https://doi.org/10.1007/s10895-020-02582-5
[28] O. Sahin, O. Alev, M. Sahin, and M. Yilmaz, Curr. Anal. Chem. **22**(6), 21 (2025). https://doi.org/10.2174/0115734110377737250831043859
[29] L. Zhang, J. Li, S. Zhao, *et al*., RSC Adv. **8**, 33121 (2018). https://doi.org/10.1039/C8RA06118G

СПЕКТРОСКОПІЧНЕ ДОСЛІДЖЕННЯ ВЗАЄМОДІЇ ІОНІВ МЕТАЛІВ ТА БІЛКІВ З ПОХІДНИМИ БЕНЗАНТРОНУ

Евіта Романовська-Дзалбе[1], Ольга Житняківська, Уляна Маловиця[2], Олена Кірілова[1], Олександр Пучкін[1], Роман Фрідман[1], Сергій Осипов[1], Валерія Трусова[2], Галина Горбенко[2]

[1]Інститут наук про життя та технології, Даугавпілський університет, LV-5401 Даугавпилс, Латвія
[2]Кафедра медичної фізики та біомедичних нанотехнологій, Харківський національний університет імені В.Н. Каразіна м. Свободи 4, Харків, 61022, Україна

У даній роботі охарактеризовано комплекси різних металів із трьома похідними бензантрону, що містили структурно подібні замісники. Отримані комплекси були детально досліджені за допомогою спектроскопічних методів. У спектрах поглинання комплексів бензантронів з металами виявлено незначні батохромні чи гіпсохромні зсуви у видимій області порівняно зі спектрами за відсутності металів. В спектрах флуоресценції цих комплексів спостерігалися суттєві зміни в положенні та інтенсивності спектральних смуг, які залежали від хімічної структури досліджуваних барвників. При вивченні взаємодії бензантронів з іонами металів в присутності амілоїдних фібрил β-лактоглобуліну виявлені метал-специфічні ефекти, зокрема, зростання флуоресценції в присутності іонів Zn^{2+} та значне гасіння флуоресценції іонами Cu^{2+}, що вказує на внесок обох типів взаємодій – барвник-метал та фібрили-метал. Ці дані свідчать про потенціал похідних бензантрону, як у вільному, так і у фібрил-зв'язаному стані як чутливих та селективних флуоресцентних зондів для детектування важких металів, що створює підґрунтя для розробки гібридних сенсорних платформ на основі біоматеріалів.

Ключові слова: *бензантронові барвники; комплекси металів; оптична спектроскопія; β-лактоглобулін*

East European Journal of Physics. **2.** 584-593 (2026)
DOI:10.26565/2312-4334-2026-2-65 ISSN 2312-4334

A MOLECULAR DOCKING STUDY OF AMYLOID-POLYSACCHARIDE COMPOSITES: II. INTERACTIONS WITH BIOLOGICALLY ACTIVE PROTEINS AND POLYPHENOLS

V. Trusova*, U. Malovytsia, O. Zhytniakivska, G. Gorbenko
Department of Medical Physics and Biomedical Nanotechnologies, V.N. Karazin Kharkiv National University
4 Svobody Sq., Kharkiv, 61022, Ukraine
**Corresponding Author email: valerija.trusova@karazin.ua*
Received March 1, 2026; revised April 13, 2026; accepted May 11, 2026

Amyloid fibrils, structurally unique protein aggregates, are increasingly emerging as a novel type of proteinaceous nanomaterial with an expanding range of applications. One example of a biomedical application of amyloid-based nanomaterials is the fabrication of biocompatible hydrogel adhesives for wound healing. The present study was undertaken to evaluate the possibility of utilizing the lysozyme amyloid fibrils integrated with polysaccharide chitosan as a polymeric matrix for incorporation the agents with pronounced wound healing capabilities such as polyphenols and biologically active proteins lactoferrin and conalbumin. Using the molecular docking technique the binding affinities, amino acid composition of the binding sites and possible competitive interactions between polyphenols have been characterized in the two-, three- and four-component systems. Polyphenolic compounds were found to display an ability to associate with bioactive proteins, with the highest binding affinities being revealed for curcumin enol, quercetin and sesamin. In the three- and four-component systems the binding sites for polyphenols are either localized exclusively on lactoferrin or conalbumin or encompass amino acid residues of both fibrillar lysozyme and bioactive proteins. Combinations of polyphenols that can compete with each other for binding sites have been identified. These findings provide a basis for the development of novel amyloid-based nanoformulations with wound-healing properties.
Keywords: *Lysozyme amyloid fibrils; Chitosan; Polyphenols; Lactoferrin; Conalbumin; Binding sites; Binding affinity; Molecular docking*
PACS: 87.14.C++c, 87.16.Dg

Amyloid fibrils, highly ordered protein assemblies distinguished by the presence of β-structured core region are currently regarded as a prospective type of biocompatible, biodegradable and structurally stable proteinaceous nanomaterials [1, 2]. A rapidly expanding area of their potential applications includes removal of heavy metals and other contaminants from water [3], sensing of various substances such as glucose [4], heavy metals [5], nitrogen dioxide [6] etc., production of bioplastic for food packaging [7], fabrication of conductive nanowires [8], cell scaffolding [9], drug delivery [10], to name only a few. Growing evidence indicates that amyloid–based materials have strong pro-regenerative potential and can accelerate wound repair [11, 12]. In particular, the hydrogel derived from lysozyme amyloid fibrils was used to prepare injectable adhesives with improved anti-swelling and antibacterial capabilities to stimulate wound closure and hemostasis [13, 14]. An advantageous feature of fibrillar lysozyme is its intrinsic antibacterial activity [15] that can be increased in the composite hydrogels from amyloid fibrils and other biopolymers with wound healing properties. In this regard, much attention has been given to chitosan, a natural polymer with antimicrobial, mucoadhesive, and anti-inflammatory activities that are favorable for wound treatment [16, 17]. Further loading of composite hydrogels with various therapeutic agents enables the creation of more efficient nanosystems for wound healing applications.

In the previous paper in this series, we obtained molecular docking predictions of the binding sites for six polyphenolic compounds from different classes in the binary system of fibrillar lysozyme–chitosan [18]. The aim of the present work was to extend the above studies by introducing additional therapeutic components, such as the functional proteins lactoferrin and conalbumin (ovotransferrin), which, like polyphenols, can promote wound repair through multiple mechanisms [19-23]. Specifically, polyphenols are known to reduce oxidative stress, modulate inflammatory responses, and enhance tissue regeneration [23], lactoferrin displays immuno-modulating activities, promotes tissue granulation, reepithelization, and synthesis of the elements of the extracellular matrix [19-21], conalbumin has antioxidant, anti-inflammatory, and immuno-stimulating properties [22, 24].

METHODS

The structures of polyphenols under study drawn in MarvinSketch software, v.18.10, ChemAxon were then optimized with Avogadro 1.1.0 software using the Universal Force Field21. The structures of bovine lactoferrin (PDB ID 1BLF) and conalbumin from chicken egg white (PDB ID 8FEI) were taken from the Protein Data Bank. The structure of the 12-mer chitosan (CS) was derived from PolySac3DB, a database of polysaccharide 3D structures (http://polysac3db.cermav.cnrs.fr). The Avogadro 1.1.0 software was utilized to protonate the chitosan molecule and optimize its geometry. The docking of the proteins and polyphenols to amyloid fibrils was conducted using the web-based server HDOCK which combines template-based and free docking [25]. The most energetically favorable docking complexes were visualized using VMD.

Cite as: V. Trusova, U. Malovytsia, O. Zhytniakivska, G. Gorbenko, East Eur. J. Phys. 2, 584 (2026), https://doi.org/10.26565/2312-4334-2026-2-65

RESULTS AND DISCUSSION

The examined systems contain two components of bioactive polymeric matrix, viz. the lysozyme amyloid fibrils and chitosan, and two therapeutic agents representing different classes of polyphenols (curcumin (enol and keto froms), gallic acid, salicylic acid, quercetin, resveratrol, sesamin) and functional proteins (lactoferrin and conalbumin). The molecular docking approach was employed to uncover the possible binding preferences of these components. Shown in Fig. 1 are the most energetically favorable complexes between lactoferrin and the examined polyphenolic compounds.

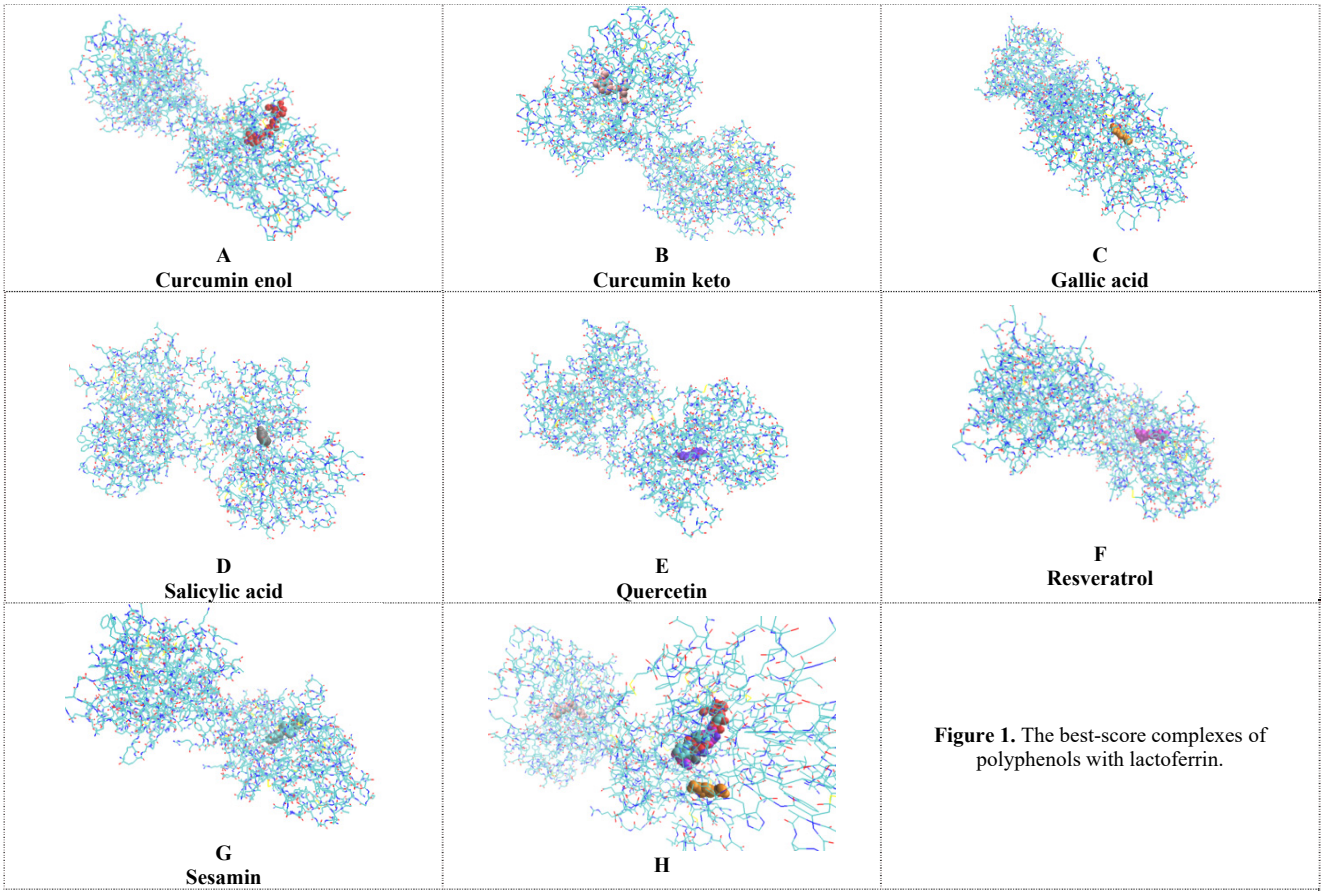

Figure 1. The best-score complexes of polyphenols with lactoferrin.

The comparative depiction of the docking poses (Fig. 1, H) indicates that the binding sites for most polyphenols are close to each other, whereas the curcumin keto and gallic acid occupy remote sites. In the case of conalbumin (Fig. 2), two predominant types of the binding sites are observed – the sites of the first type accommodate curcumin keto, gallic and salicylic acids, quercetin, resveratrol, and sesamin reside on the sites of the second type, while curcumin enol is located at the remote site with completely different interface residues (Table 1).

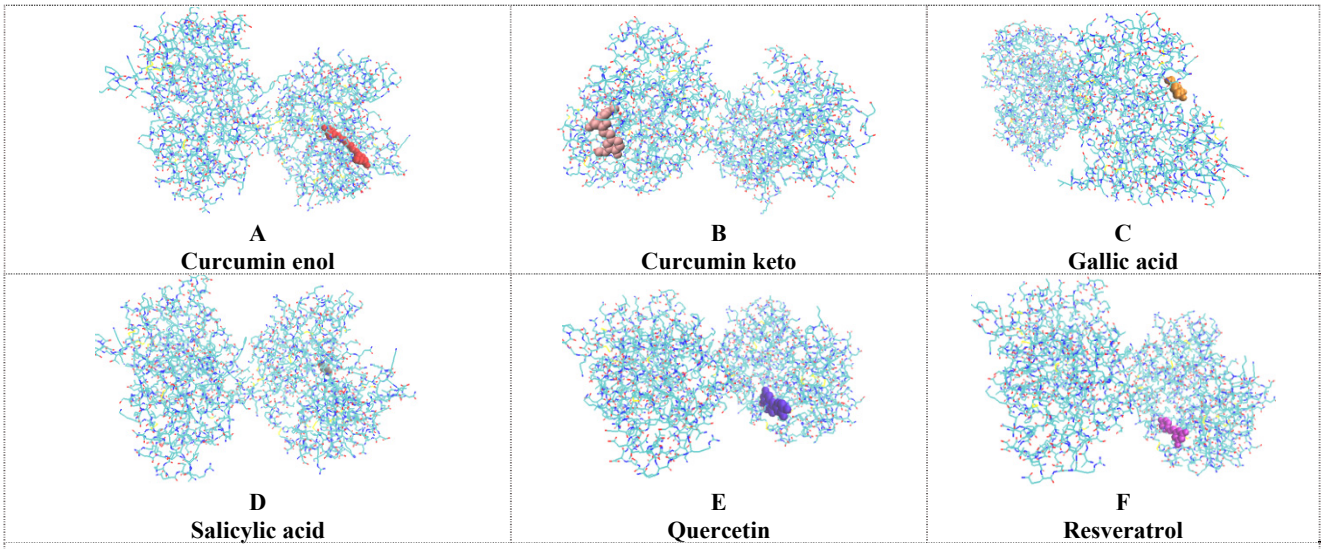

Figure 2. The best-score complexes of polyphenols with conalbumin
(*continued on next page*)

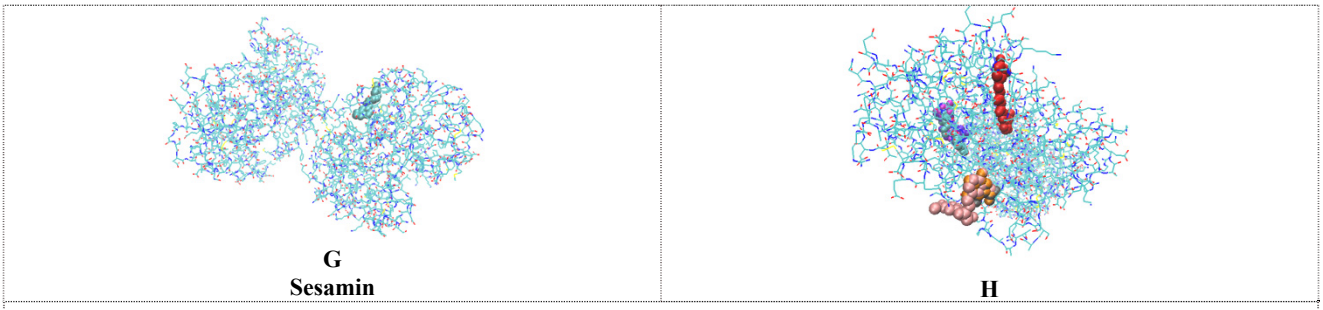

Figure 2. The best-score complexes of polyphenols with conalbumin (*continuation*)

Table 1. The interface residues in the complexes of polyphenols with lactoferrin and conalbumin

Polyphenol	Lactoferrin	Conalbumin
Curcumin enol	VAL_{350A} PRO_{352A} GLU_{353A} GLU_{354A} ARG_{463A} ASP_{508A} ASP_{509A} SER_{519A} LYS_{520A} GLU_{521A} LYS_{522A} TYR_{523A} TYR_{524A} GLY_{525A} TYR_{526A} THR_{527A} GLY_{528A} ARG_{531A} HIS_{595A} LYS_{637A} ASN_{638A} LEU_{639A} LEU_{640A} ASN_{642A}	VAL_{350A} GLU_{354A} THR_{377A} ALA_{393A} LEU_{394A} ARG_{460A} ALA_{515A} SER_{516A} SER_{517A} HIS_{518A} GLU_{519A} LYS_{520A} PHE_{522A} GLY_{523A} TYR_{524A} THR_{525A} GLY_{526A} ARG_{529A} TRP_{557A} HIS_{592A} ASN_{632A} LYS_{633A} ASP_{634A}
Curcumin keto	ILE_{11A} GLU_{15A} PHE_{41A} ALA_{42A} THR_{58A} LEU_{59A} ASP_{60A} MET_{63A} LEU_{119A} GLY_{120A} ARG_{121A} CYS_{160A} CYS_{183A} SER_{185A} PHE_{190A} GLY_{191A} TYR_{192A} SER_{193A} GLY_{194A} HIS_{253A} GLN_{295A} ARG_{296A} ASP_{297A} LEU_{298A}	ARG_{414A} TYR_{415A} ASP_{416A} ARG_{427A} PRO_{428A} ALA_{429A} SER_{430A} TYR_{431A} PHE_{432A} HIS_{542A} TYR_{581A} ARG_{582A} GLU_{588A} LEU_{640A}
Gallic acid	GLU_{413A} ASN_{414A} ARG_{415A} TYR_{433A} TYR_{526A} LYS_{544A} ASP_{546A} PRO_{593A} ASN_{594A} HIS_{595A} ASN_{642A} ASN_{644A} THR_{645A}	GLU_{413A} ARG_{414A} TYR_{415A} ASP_{416A} ARG_{427A} PRO_{428A} ALA_{429A} SER_{430A} TYR_{431A} PHE_{432A} HIS_{542A} TYR_{581A} ARG_{582A} LEU_{640A}
Salicylic acid	GLU_{354A} ASN_{393A} LEU_{394A} GLU_{413A} ARG_{463A} TYR_{524A} TYR_{526A} HIS_{595A} LYS_{637A} ASN_{638A} LEU_{639A} LEU_{640A} PHE_{641A} ASN_{642A}	GLU_{413A} ARG_{414A} TYR_{415A} ASP_{416A} ARG_{427A} PRO_{428A} ALA_{429A} SER_{430A} TYR_{431A} PHE_{432A} HIS_{542A} ARG_{582A}
Quercetin	GLU_{354A} ASN_{393A} LEU_{394A} ASP_{395A} GLU_{413A} ARG_{463A} ASN_{518A} SER_{519A} GLU_{521A} TYR_{524A} GLY_{525A} TYR_{526A} THR_{527A} GLY_{528A} HIS_{595A} LYS_{637A} ASN_{638A} LEU_{639A} LEU_{640A} PHE_{641A} ASN_{642A}	VAL_{458A} GLY_{459A} TRP_{464A} CYS_{478A} ASN_{479A} PHE_{480A} ASP_{481A} SER_{492A} PRO_{493A} LEU_{668A} LYS_{669A} CYS_{671A} ASN_{672A} SER_{674A}
Resveratrol	GLU_{354A} ASN_{393A} LEU_{394A} GLU_{413A} ARG_{463A} SER_{519A} TYR_{524A} GLY_{525A} TYR_{526A} THR_{527A} GLY_{528A} HIS_{595A} LYS_{637A} ASN_{638A} LEU_{639A} LEU_{640A} PHE_{641A} ASN_{642A}	VAL_{458A} GLY_{459A} TRP_{464A} CYS_{478A} ASN_{479A} PHE_{480A} ASP_{481A} SER_{492A} PRO_{493A} SER_{496A} LEU_{498A} ILE_{665A} LEU_{668A} LYS_{669A} CYS_{671A} ASN_{672A}
Sesamin	GLU_{353A} GLU_{354A} THR_{377A} ASN_{393A} LEU_{394A} ASP_{395A} TYR_{398A} ARG_{463A} ASN_{518A} SER_{519A} GLU_{521A} LYS_{522A} TYR_{523A} TYR_{524A} GLY_{525A} TYR_{526A} THR_{527A} GLY_{528A} HIS_{595A} LYS_{637A} ASN_{638A} LEU_{639A} ASN_{642A}	TYR_{400A} VAL_{458A} TRP_{464A} VAL_{465A} CYS_{478A} ASN_{479A} PHE_{480A} ASP_{481A} LEU_{498A} ILE_{665A} LEU_{668A} LYS_{669A} CYS_{671A} ASN_{672A} PRO_{673A} LEU_{677A}

These results are suggestive of the possibility that the use of certain polyphenol combinations may lead to competitive interactions between these compounds for the binding sites on lactoferrin or conalbumin.

The analysis of the best score values (Table 2) showed that quercetin forms the strongest complexes with lactoferrin, while curcumin (enol) - with conalbumin, with the binding affinities increasing in the order: salicylic acid < gallic acid < resveratrol < curcumin keto < curcumin enol < sesamin < quercetin for lactoferrin, and in the order salicylic acid < gallic acid < resveratrol < curcumin keto < quercetin < sesamin < curcumin enol for conalbumin. Notably, gallic and salicylic acids displayed the lowest affinity for both proteins. Another observation noteworthy is that polyphenols appeared to have slightly different (curcumin enol) or higher affinities for lactoferrin and conalbumin compared to those for the lysozyme fibrils [18].

Table 2. The best score values for the complexes of polyphenols with lactoferrin, conalbumin and chitosan

Polyphenol	Lactoferrin	Conalbumin	Chitosan
Curcumin enol	-177.30 (0.633)	-181.39 (0.652)	-18.64 (0.067)
Curcumin keto	-162.58 (0.563)	-151.14 (0.506)	-17.23 (0.066)
Gallic acid	-128.36 (0.394)	-117.76 (0.344)	-16.58 (0.065)
Salicylic acid	-107.48 (0.299)	-98.36 (0.263)	-13.78 (0.062)
Quercetin	-204.36 (0.748)	-169.24 (0.595)	-21.45 (0.071)
Resveratrol	-154.94 (0.525)	-126.49 (0.385)	-14.78 (0.063)
Sesamin	-187.76 (0.680)	-172.04 (0.608)	-17.94 (0.067)

*The confidence scores for binding probability are given in parentheses, with the values > 0.7 indicating a high probability, 0.5-0.7 moderate probability, and < 0.5 - low probability.

Accordingly, in the systems lysozyme fibrils + proteins the binding sites for polyphenols predominantly encompass the amino acid residues of lactoferrin or conalbumin (Figs. 3, 4), although in some cases (marked in grey in Table 3) the amino acids of fibrillar lysozyme also contribute to stabilization of the complexes being formed.

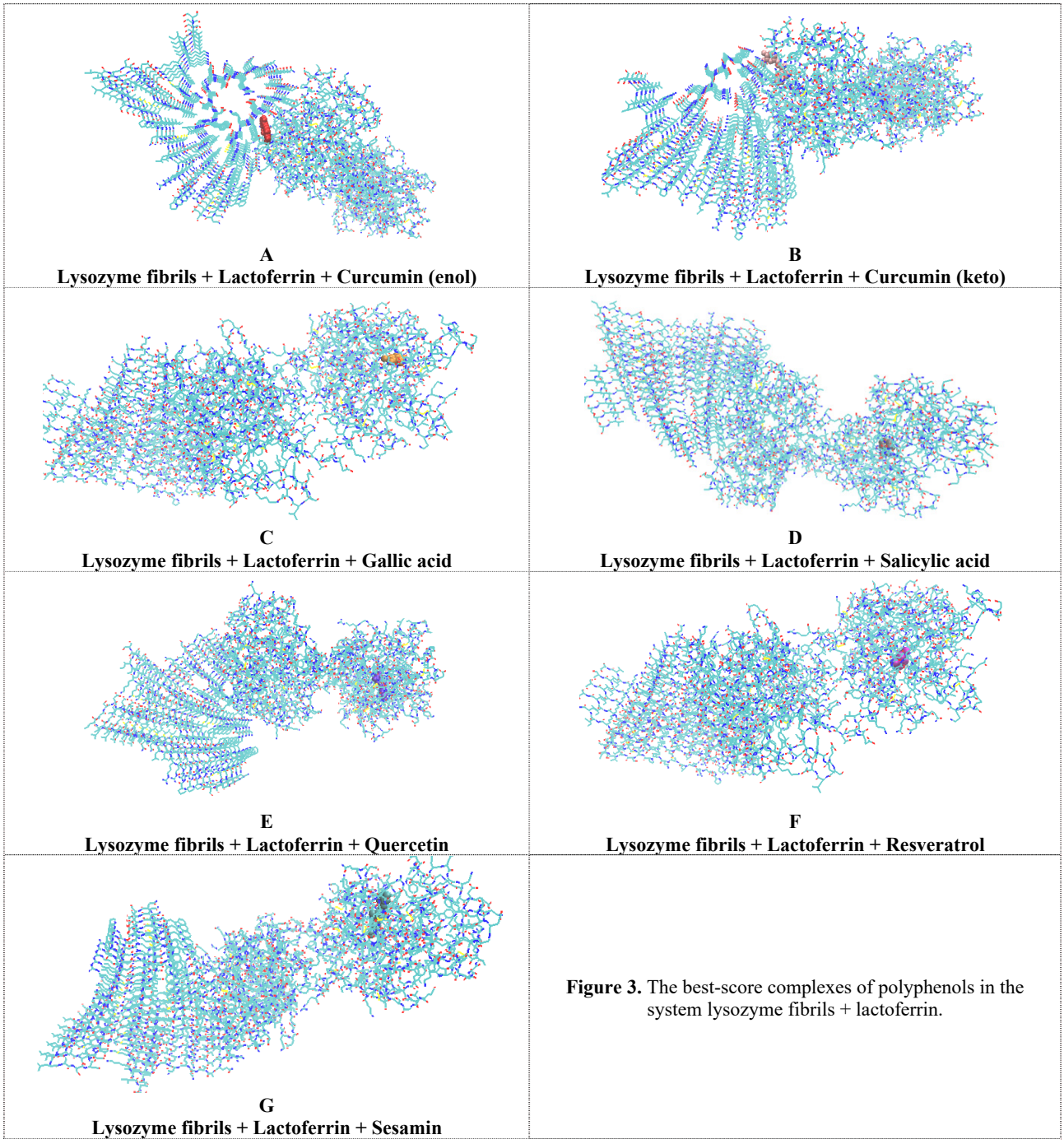

A
Lysozyme fibrils + Lactoferrin + Curcumin (enol)

B
Lysozyme fibrils + Lactoferrin + Curcumin (keto)

C
Lysozyme fibrils + Lactoferrin + Gallic acid

D
Lysozyme fibrils + Lactoferrin + Salicylic acid

E
Lysozyme fibrils + Lactoferrin + Quercetin

F
Lysozyme fibrils + Lactoferrin + Resveratrol

G
Lysozyme fibrils + Lactoferrin + Sesamin

Figure 3. The best-score complexes of polyphenols in the system lysozyme fibrils + lactoferrin.

In the lactoferrin-containing systems, only curcumin enol and curcumin keto were found to form contacts with both lactoferrin and lysozyme fibrils, whereas the binding sites for other polyphenols are localized exclusively on the protein molecule (Fig. 3, Table 3).

Table 3. The interface residues in the complexes of polyphenols with the components of the systems lysozyme fibrils + lactoferrin / conalbumin in the absence and presence of chitosan

	Lactoferrin	**Conalbumin**	**Lactoferrin**	**Conalbumin**
	Lysozyme fibrils		**Lysozyme fibrils + chitosan**	
Curcumin enol	PHE_{34C} GLU_{35C} PHE_{34E} GLU_{35E} SER_{36E} PHE_{34G} GLU_{35G} SER_{36G} PHE_{34I}	TRP_{63A} GLY_{26C} TRP_{63C} GLY_{26E} TRP_{63E} GLY_{26G} TRP_{63G} GLY_{26I} TRP_{63I}	PHE_{34A} PHE_{34C} GLU_{35C} SER_{36C} PHE_{34E} GLU_{35E} SER_{36E} PHE_{34G} GLU_{35G}	VAL_{350A} GLU_{354A} THR_{377A} ALA_{393A} ARG_{460A} ALA_{515A}

	Lactoferrin	Conalbumin	Lactoferrin	Conalbumin
	Lysozyme fibrils		**Lysozyme fibrils + chitosan**	
	GLU_{35I} SER_{36I} GLN_{13A} PRO_{14A} PHE_{17A} LYS_{18A} ARG_{21A} GLY_{175A} GLU_{176A} ASN_{179A} SER_{185A} ARG_{186A} PRO_{188A} PRO_{292A} PRO_{293A} GLN_{295A}	VAL_{81A} SER_{88A} GLN_{271A} SER_{272A} ASP_{273A} PHE_{274A} GLY_{275A} VAL_{276A} ASP_{277A} THR_{278A} PHE_{285A} ILE_{305A} MET_{306A} LYS_{308A} GLY_{685A} LYS_{686A}	SER_{36G} PHE_{34I} SER_{36I} GLN_{13A} PRO_{14A} PHE_{17A} ARG_{21A} LYS_{174A} ARG_{186A} PRO_{188A} PRO_{292A} PRO_{293A} GLN_{295A}	SER_{516A} SER_{517A} HIS_{518A} GLU_{519A} LYS_{520A} PHE_{522A} GLY_{523A} TYR_{524A} THR_{525A} GLY_{526A} ARG_{529A} TRP_{557A} HIS_{592A} ASN_{632A} LYS_{633A} ASP_{634A}
Curcumin keto	PHE_{38A} ASN_{39A} PHE_{38C} ASN_{39C} PHE_{38E} GLU_{216A} LYS_{280A} ASN_{281A} GLN_{287A} PHE_{289A} GLY_{290A} SER_{291A} ARG_{296A} ASP_{302A} SER_{303A}	ARG_{61A} ASP_{66A} PRO_{70A} GLY_{71A} SER_{72A} ASP_{66C} VAL_{458A} TRP_{464A} CYS_{478A} ASN_{479A} PHE_{480A} ASP_{481A} SER_{492A} PRO_{493A} LEU_{498A} LEU_{68A} LYS_{669A} CYS_{671A} ASN_{672A}	SER_{36G} ASN_{37G} PHE_{38G} SER_{36I} ASN_{37I} PHE_{38I} ASN_{39I} SER_{93A} LYS_{197A} GLN_{200A} ASP_{201A} ASN_{217A} LEU_{218A} ASP_{223A} GLN_{226A} TYR_{227A} PRO_{292A} PRO_{293A} GLY_{294A} ARG_{296A}	TRP_{63E} CYS_{64E} ASN_{65E} TRP_{63G} CYS_{64G} ASN_{65G} GLY_{26I} TRP_{63I} ASN_{65I} PHE_{432A} ARG_{582A} GLU_{583A} ASN_{585A} ALA_{587A} GLU_{588A} LYS_{660A}
Gallic acid	GLU_{413A} ASN_{414A} ARG_{415A} TYR_{433A} TYR_{526A} LYS_{544A} ASP_{546A} PRO_{593A} ASN_{594A} HIS_{595A} ASN_{642A} ASN_{644A} THR_{645A}	TRP_{63A} CYS_{64A} ASN_{65A} TRP_{63C} CYS_{64C} ASN_{65C} TRP_{264A} LYS_{308A} ARG_{309A} VAL_{310A} PRO_{311A} SER_{312A} GLN_{678A} MET_{679A} PHE_{682A}	SER_{36G} ASN_{37G} PHE_{38G} SER_{36I} PHE_{38I} SER_{193A} GLY_{194A} PHE_{196A} LYS_{197A} GLN_{200A} ASN_{217A} PRO_{293A} GLY_{294A} ARG_{296A}	TRP_{28I} CYS_{30I} SER_{60I} TRP_{62I} TRP_{445A} GLY_{469A} LEU_{470A} ILE_{471A} ASN_{473A} ARG_{474A} THR_{571A} ASP_{572A}
Salicylic acid	GLU_{354A} ASN_{393A} LEU_{394A} GLU_{413A} ARG_{463A} TYR_{524A} TYR_{526A} HIS_{595A} ASN_{638A} LEU_{639A} LEU_{640A} PHE_{641A} ASN_{642A}	TRP_{63A} CYS_{64A} ASN_{65A} TRP_{63C} CYS_{64C} ASN_{65C} TRP_{63E} TRP_{264A} LYS_{308A} ARG_{309A} VAL_{310A} PRO_{311A}	PHE_{38G} PHE_{38I} SER_{193A} GLY_{194A} PHE_{196A} LYS_{197A} GLN_{200A} ASN_{217A} PRO_{293A} GLY_{294A} ARG_{296A}	TRP_{28I} CYS_{30I} SER_{60I} TRP_{62I} TRP_{445A} GLY_{469A} LEU_{470A} ILE_{471A} ASN_{473A} ARG_{474A} THR_{571A}
Quercetin	GLU_{354A} ASN_{393A} LEU_{394A} ASP_{395A} GLU_{413A} ARG_{463A} SER_{519A} TYR_{524A} GLY_{525A} TYR_{526A} THR_{527A} GLY_{528A} HIS_{595A} LYS_{637A} ASN_{638A} LEU_{639A} LEU_{640A} PHE_{641A} ASN_{642A}	VAL_{458A} GLY_{459A} TRP_{464A} CYS_{478A} ASN_{479A} PHE_{480A} ASP_{481A} SER_{492A} PRO_{493A} LEU_{668A} LYS_{669A} CYS_{671A} ASN_{672A} SER_{674A}	GLU_{354A} ASN_{393A} LEU_{394A} ASP_{395A} GLU_{413A} ARG_{463A} SER_{519A} GLU_{521A} TYR_{524A} GLY_{525A} TYR_{526A} THR_{527A} GLY_{528A} HIS_{595A} LYS_{637A} ASN_{638A} LEU_{639A} LEU_{640A} PHE_{641A} ASN_{642A}	TRP_{28I} ILE_{58I} ASN_{59I} SER_{60I} ARG_{61I} TRP_{62I} SER_{72I} ASN_{74I} TRP_{445A} LEU_{470A} ASN_{473A} ARG_{474A} THR_{571A} ASP_{572A}
Resveratrol	GLU_{354A} ASN_{393A} LEU_{394A} GLU_{413A} ARG_{463A} SER_{519A} GLU_{521A} TYR_{524A} GLY_{525A} TYR_{526A} THR_{527A} GLY_{528A} HIS_{595A} LYS_{637A} ASN_{638A} LEU_{639A} LEU_{640A} PHE_{641A} ASN_{642A}	ASN_{59A} SER_{60A} ARG_{61A} GLY_{71A} SER_{72A} ASN_{59C} VAL_{458A} TRP_{464A} CYS_{478A} ASN_{479A} PHE_{480A} ASP_{481A} LEU_{498A} CYS_{671A} ASN_{672A}	GLU_{354A} ASN_{393A} LEU_{394A} GLU_{413A} ARG_{463A} SER_{519A} TYR_{524A} GLY_{525A} TYR_{526A} THR_{527A} GLY_{528A} HIS_{595A} LYS_{637A} ASN_{638A} LEU_{639A} LEU_{640A} PHE_{641A} ASN_{642A}	GLU_{35C} LYS_{33E} GLU_{35E} ARG_{45E} LYS_{33G} GLU_{35G} ARG_{45G} ASP_{52G} LYS_{33I} GLU_{35I} ARG_{45I} ASP_{52I} CS_7 CS_8 CS_9 CS_{10}
Sesamin	GLU_{353A} GLU_{354A} ASN_{393A} LEU_{394A} ASP_{395A} TYR_{398A} ARG_{463A} ASN_{518A} SER_{519A} GLU_{521A} LYS_{522A} TYR_{523A} TYR_{524A} GLY_{525A} TYR_{526A} THR_{527A} GLY_{528A} ARG_{531A} HIS_{595A} THR_{636A} LYS_{637A} ASN_{638A} LEU_{639A} PHE_{641A} ASN_{642A}	TYR_{400A} VAL_{458A} TRP_{464A} VAL_{465A} CYS_{478A} ASN_{479A} PHE_{480A} ASP_{481A} LEU_{498A} ILE_{665A} LEU_{668A} LYS_{669A} CYS_{671A} ASN_{672A} PRO_{673A} LEU_{677A}	GLU_{35A} PHE_{34C} GLU_{35C} SER_{36C} PHE_{34E} GLU_{35E} SER_{36E} PHE_{34G} GLU_{35G} SER_{36G} PHE_{34I} GLU_{35I} SER_{36I} PHE_{17A} ARG_{21A} PRO_{292A} PRO_{293A} GLY_{294A} GLN_{295A}	LYS_{33E} PHE_{34E} GLU_{35E} ARG_{45E} LYS_{33G} PHE_{34G} GLU_{35G} ARG_{45G} LYS_{33I} PHE_{34I} GLU_{35I} ARG_{45I} ASP_{52I} CS_7 CS_8 CS_9 CS_{10} CS_{11}

At the same time, in the conalbumin-containing systems, quercetin and sesamin reside on the protein molecule, while the other polyphenolic compounds form contacts with both conalbumin and lysozyme fibrils (Fig. 4, Table 3).

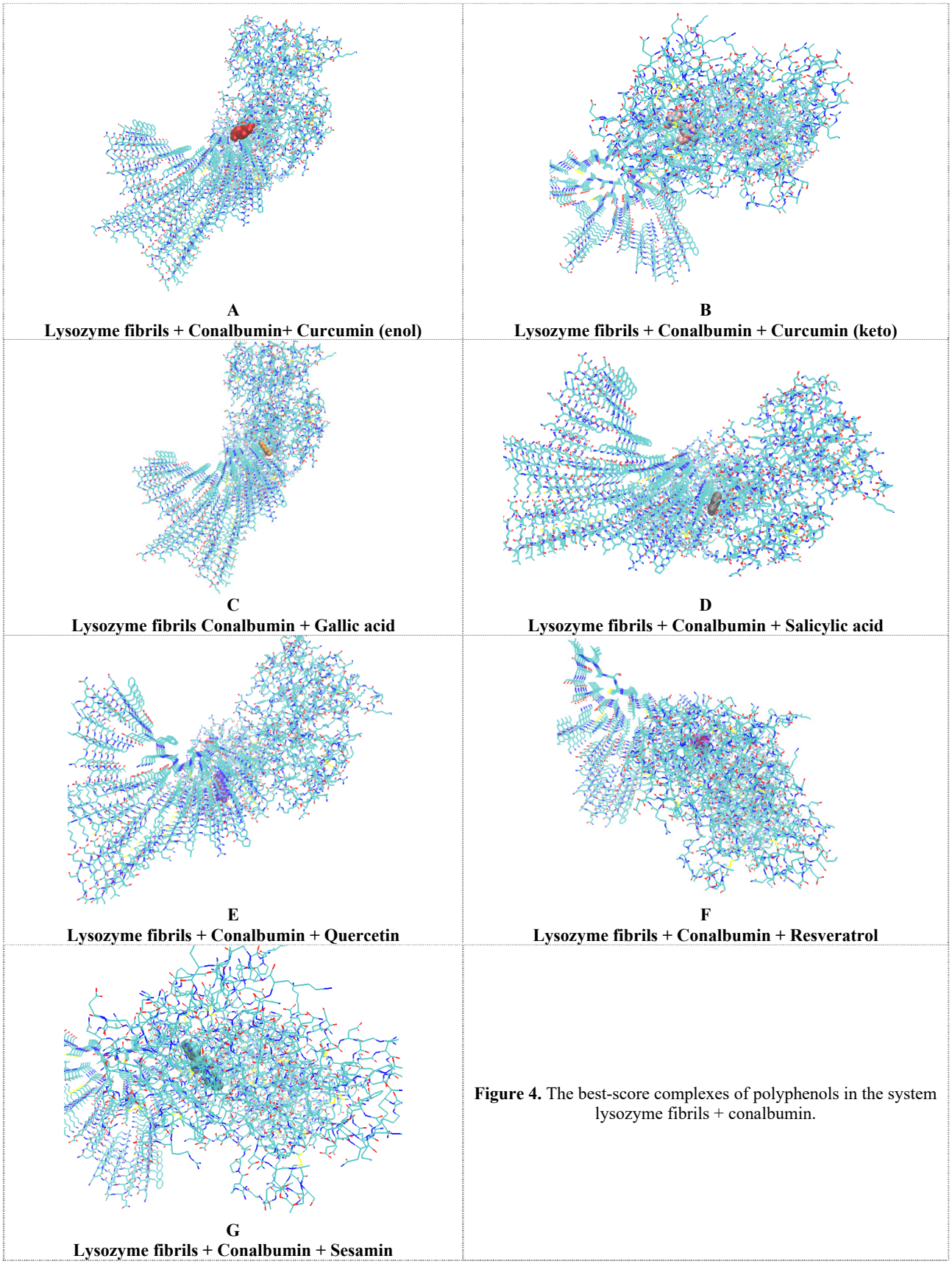

A
Lysozyme fibrils + Conalbumin+ Curcumin (enol)

B
Lysozyme fibrils + Conalbumin + Curcumin (keto)

C
Lysozyme fibrils Conalbumin + Gallic acid

D
Lysozyme fibrils + Conalbumin + Salicylic acid

E
Lysozyme fibrils + Conalbumin + Quercetin

F
Lysozyme fibrils + Conalbumin + Resveratrol

G
Lysozyme fibrils + Conalbumin + Sesamin

Figure 4. The best-score complexes of polyphenols in the system lysozyme fibrils + conalbumin.

The addition of chitosan to the system lysozyme fibrils + lactoferrin / conalbumin resulted in the association of polyphenols with completely different or slightly changed binding sites (Figs. 5, 6, Table 3). As judged from Table 3, the

smallest changes in the presence of chitosan were observed in the lactoferrin-containing systems for quercetin (the appearance of GLU_{521A} in the binding site) and resveratrol (the disappearance of GLU_{521A} in the binding site). Likewise, the analysis of the composition of binding sites showed that in the ternary systems with lactoferrin there exists a possibility of competitive interactions between salicylic acid, quercetin, resveratrol and sesamin; while in the systems with conalbumin gallic acid can compete with salicylic acid, quercetin – with resveratrol and sesamin. In the quaternary systems with lactoferrin the competition may occur between curcumin keto, gallic and salicylic acids, quercetin and resveratrol, curcumin enol and sesamin, while in the systems with conalbumin the competitive ligands are represented by quercetin, gallic and salicylic acids, resveratrol and sesamin. Obviously, the possibility of competitive interactions must be taken into account while incorporating the mixtures of different polyphenols into a polymeric matrix.

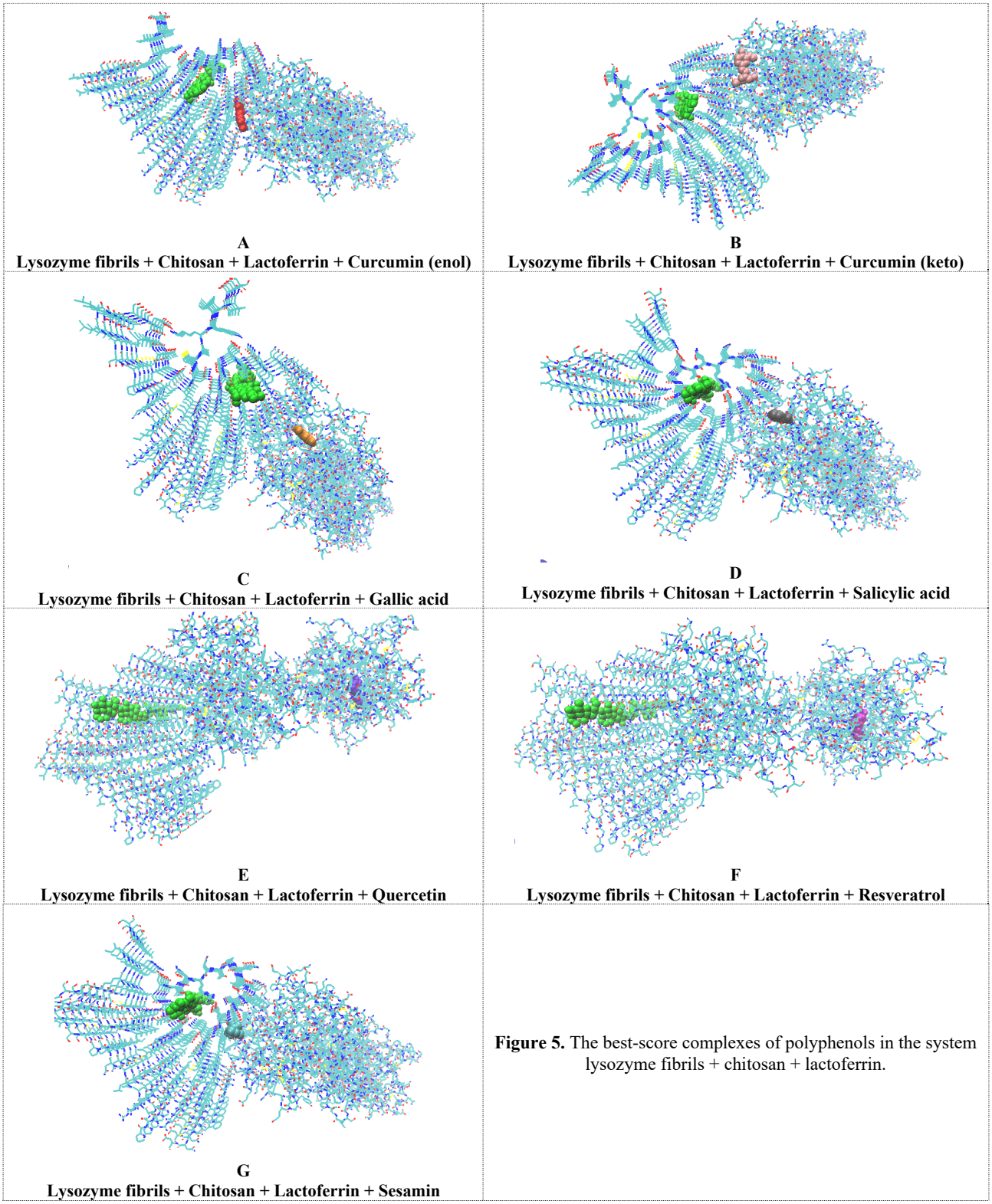

Figure 5. The best-score complexes of polyphenols in the system lysozyme fibrils + chitosan + lactoferrin.

As seen from Table 4, in most cases, chitosan did not exert influence on the binding affinities of polyphenols – the changes in the best score values were less than 10%. The most pronounced increases in the best score values were observed in the systems with lactoferrin / conalbumin and curcumin enol, by 14% and 10%, respectively. On the contrary, the binding affinities of the gallic and salicylic acids showed a decrease (~12%) in the systems with chitosan and conalbumin (Table 4).

Table 4. The best score values for polyphenol binding with the components of the systems lysozyme fibrils + lactoferrin / conalbumin, in the absence and presence of chitosan

Polyphenol	Lysozyme fibrils + Lactoferrin	Lysozyme fibrils + Chitosan + Lactoferrin	Lysozyme fibrils +Conalbumin	Lysozyme fibrils +Chitosan + Conalbumin
	-333.24 (0.975)	-335.82 (0.976)	-280.81 (0.932)	-295.49 (0.948)
Curcumin enol	-179.21 (0.642)	-204.77 (0.749)	-185.38 (0.669)	-183.19 (0.660)
Curcumin keto	-169.33 (0.596)	-177.26 (0.633)	-167.26 (0.586)	-183.75 (0.663)
Gallic acid	-127.27 (0.388)	-128.33 (0.393)	-141.75 (0.459)	-124.36 (0.375)
Salicylic acid	-106.88 (0.297)	-113.55 (0.325)	-117.21 (0.342)	-102.86 (0.280)
Quercetin	-205.28 (0.751)	-203.43 (0.744)	-171.98 (0.608)	-173.77 (0.617)
Resveratrol	-154.12 (0.521)	-154.71 (0.524)	-132.80 (0.415)	-135.29 (0.427)
Sesamin	-187.74 (0.680)	-197.86 (0.723)	-173.6 (0.616)	-185.91 (0.672)

Interestingly, in the systems with conalbumin resveratrol and sesamin displayed the ability to form contacts with chitosan, so that the binding sites for these polyphenols contain only amino acid residues of lysozyme fibrils and monomeric subunits of chitosan (Table 3), while in the absence of polysaccharide resveratrol form contacts only with conalbumin, while sesamin associate with both the protein and fibril (Fig. 6, F, G). In the presence of chitosan the binding affinity of resveratrol remained practically unchanged, while that of sesamin slightly increased (Table 4).

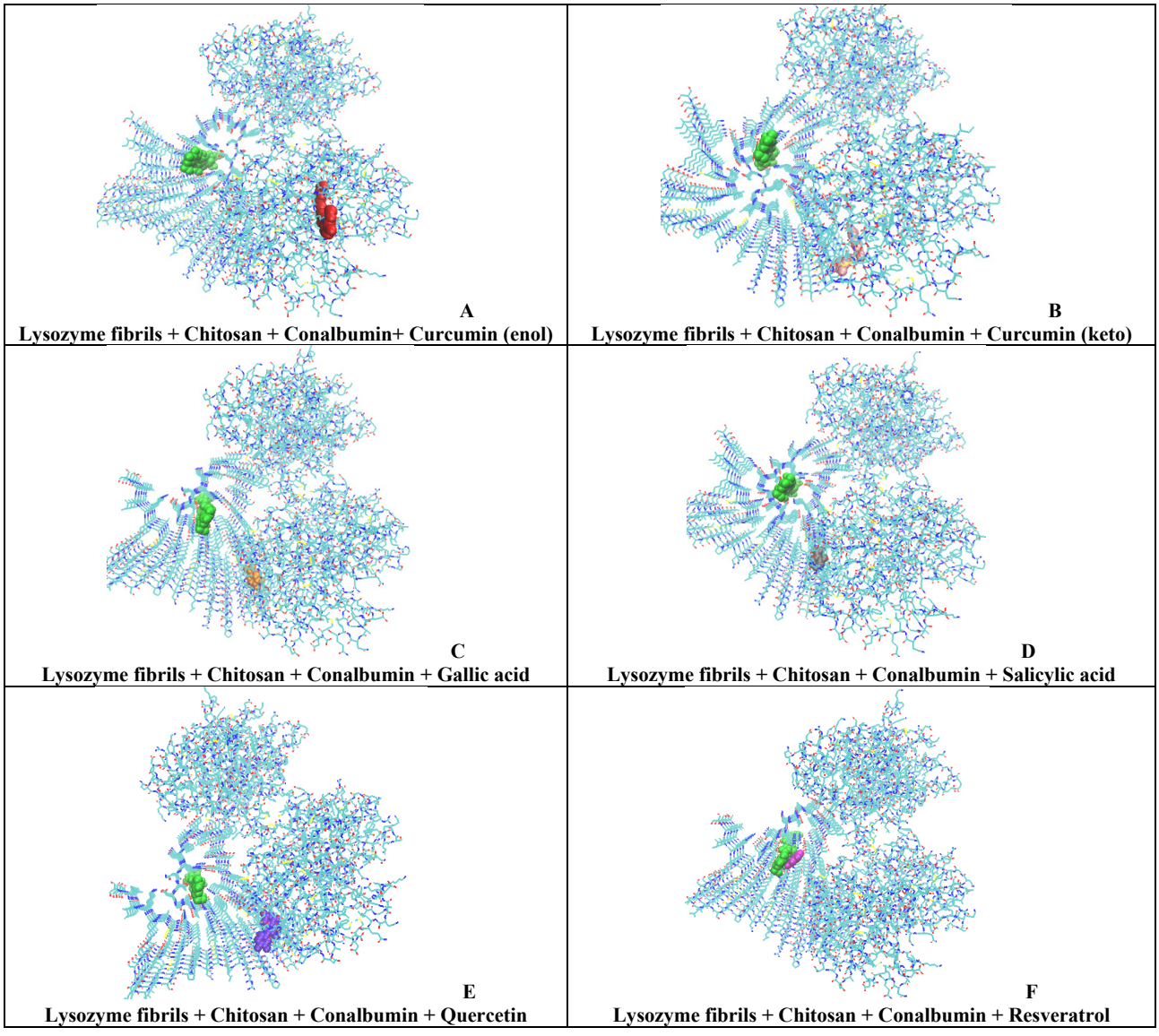

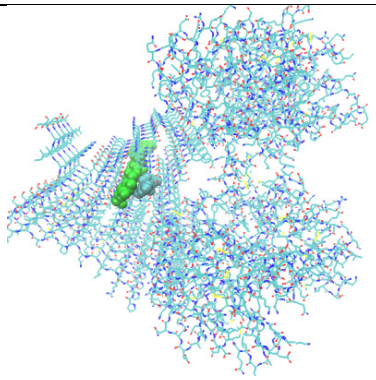

G
Lysozyme fibrils + Chitosan + Conalbumin + Sesamin

Figure 6. The best-score complexes of polyphenols in the system lysozyme fibrils +chitosan + conalbumin

Another noteworthy observation is that the association of the examined polyphenols with chitosan per se is very weak; the best docking scores range from -13 to -21 (Table 2). However, as shown in our previous work [18], when chitosan resides in the grooves of lysozyme fibrils, most polyphenolic compounds tend to form contacts with both the amyloid fibrils and the polysaccharide, and binding affinities are much higher than those for free chitosan. At the same time, in the systems complemented by lactoferrin or conalbumin, polyphenols exhibit more complex binding behavior, so that only resveratrol and sesamin interact exclusively with fibrillar lysozyme and chitosan in the presence of conalbumin.

CONCLUSIONS

In summary, the present study demonstrated the possibility of creating nanosystems composed of four biologically active components: lysozyme amyloid fibrils, chitosan as the polymeric matrix, and lactoferrin or conalbumin and polyphenols as therapeutic agents. The molecular docking technique provided insights into the behavior of these components in binary, ternary, and quaternary systems. The main results are as follows: i) the binding affinity of polyphenols for functional proteins increases in the order salicylic acid < gallic acid < resveratrol < curcumin keto < curcumin enol < sesamin < quercetin for lactoferrin, and in the order salicylic acid < gallic acid < resveratrol < curcumin keto < quercetin < sesamin < curcumin enol for conalbumin, suggesting that quercetin, sesamin and curcumin enol form the strongest complexes with the proteins; ii) among 24 examined ternary and quaternary combinations of various components in 10 systems polyphenols prefer to associate with lactoferrin or conalbumin, while in the remaining systems they form contacts with both fibrillar lysozyme and bioactive proteins; iii) in the ternary and quaternary systems polyphenols can compete for the binding sites; iv) in the presence of conalbumin in quaternary systems resveratrol and sesamin showed the binding preferences for the lysozyme fibrils and chitosan. These findings can serve as a basis for the rational design and fabrication of novel nanocomposites for biomedical applications, particularly in wound healing.

Acknowledgements

This work was supported by the Ministry of Education and Science of Ukraine (the project “Design of novel biocompatible nanocomposites and improvement of ultrasound-based diagnostic methods for medical applications” No. 0126U001036).

ORCID

Valeriya Trusova, https://orcid.org/0000-0002-7087-071X; **Uliana Malovytsia,** https://orcid.org/0000-0002-7677-0779
Olga Zhytniakivska, https://orcid.org/0000-0002-2068-5823; **Galyna Gorbenko,** https://orcid.org/0000-0002-0954-5053

REFERENCES

[1] S. Yadav, P. Padhy, A. Singh, S. Sharma, Tanu, S. Fatima, A. Sinha, R. Tariq, Varsha, S. Sharma and S. Priya, Mater. Adv**. 5**, 4078–4090 (2024). https://doi.org/10.1039/d3ma00969f
[2] Q. Xuan, J. Cai, Y. Gao, X. Qiao, T. Jin, M. Peydayesh, J. Zhou, Q. Sun, L. Zhan, B. Liu, P. Wang, H. Li, C. Chen, and R. Mezzenga, Adv. Mater. **37**, 2417774 (2025). https://doi.org/10.1002/adma.202417774
[3] X. Jia, M. Peydayesh, Q. Huang and R. Mezzenga, Small **18**, 2105502 (2022). https://doi.org/10.1002/smll.202105502
[4] M. Díaz-Caballero, S. Navarro and S. Ventura, Biomacromolecules **22**, 2822–2833 (2021). https://doi.org/10.1021/acs.biomac.1c00222
[5] C. Kim, J. Park, W. Kim, W. Lee, S. Na and J. Park, Bioelectrochemistry **147,** 108214 (2022). https://doi.org/10.1016/j.bioelechem.2022.108214
[6] S. W. Lee, W. Lee, I. Kim, D. Lee, D. Park, W. Kim, J. Park, J. H. Lee, G. Lee and D. S. Yoon, ACS Sens. **6**, 777–785 (2021). https://doi.org/10.1021/acssensors.0c01582
[7] M. K. DeBari, M. N. Keyser, M. A. Bai and R. D. Abbott, Connect. Tissue Res. **61**, 163–173 (2020). https://doi.org/10.1080/03008207.2018.1553959
[8] J. Li and F. Zhang, Int. J. Mol. Sci. **22**, 10698 (2021). https://doi.org/10.3390/ijms221910698
[9] D. Wu, J. Zhou, Y. Shen, C. Lupo, Q. Sun, T. Jin, S. Sturla, H. Liang and R. Mezzenga, Biomacromolecules **24**, 1, 471–480 (2023). https://doi.org/10.1021/acs.biomac.2c01311
[10] Y. R. Lai, S. S. Wang, T. L. Hsu, S. H. Chou, S. C. How and T. H. Lin, Polymers **15**, 1444 (2023). https://doi.org/10.3390/polym15061444

[11] R. Shaw, K. Patel, N. Chimthanawala, S. Sathaye and S. Maji, Adv. Healthcare Mater. **14**, 2403560 (2025). https://doi.org/10.1002/adhm.202403560
[12] J. Sawicka, E. Iłowska, M. Deptuła, P. Sosnowski, P. Sass, K. Czerwiec, K. Chmielewska, A. Szymańska, Z. Pietralik-Molińska, M. Kozak, P. Sachadyn, M. Pikuła and S. Rodziewicz-Motowidło, Int. J. Mol. Sci. **22**, 3818 (2021). https://doi.org/10.3390/ijms22083818
[13] T. Chen, Y. Wang, J. Xie, X. Qu and C. Liu, Biomacromolecules **23**, 1376–1391 (2022). https://doi.org/10.1021/acs.biomac.1c01597
[14] T. Liu, Z. Wang, X. Zhang, D. Xu, Q. Yan, Y. Chen and S. Luan, Biomater. Sci. **13**, 688-696 (2025). DOI https://doi.org/10.1039/D4BM01494D
[15] Z. WeiSihong, W. Xia, P. Shao, P. Sun, and N. Xiang. Biomacromolecules **22**, 890–897 (2021). https://doi.org/10.1021/acs.biomac.0c01599
[16] J. Shah, D. Patel, D. Rananavare, D. Hudson, M. Tran, R. Schloss, N. Langrana, F. Berthiaume and S. Kumar. J. Funct. Biomater. **16**, 45 (2025). https://doi.org/10.3390/jfb16
[17] S. Naveedunissa, R. Meenalotchani, M. Manisha, S. Singh, S. Nirenjen, K. Anitha, N. Harikrishnan and B. Prajapati, Carbohydr. Polym. Technol. Appl. **11**, 100891 (2025). https://doi.org/10.1016/j.carpta.2025.100891
[18] V. Trusova, U. Malovytsia, O. Zhytniakivska and G. Gorbenko, (2026). East Eur. J. Phys. **1**, 525–530 (2026). https://doi.org/10.26565/2312-4334-2026-1-60
[19] Z. Ng, M. Addeen bin, M. Daud, K. Lian, S. Migeemanathan, G. Shin, T. Shunmugham, J. Thian Hee, T. Wei, K. Ling, N. Sa'aid, T. Thong, F. Ci and J. Tan, Trends Food Sci. Technol. **160**, 105024 (2025). https://doi.org/10.1016/j.tifs.2025.105024
[20] Y. Lin, S. Song and H. Guo, Curr. Opin. Food Sci. **63,** 101285 (2025). https://doi.org/10.1016/j.cofs.2025.101285
[21] Y. Takayama, Y. Effects of Lactoferrin on Skin Wound Healing. In: Lactoferrin and its Role in Wound Healing. Springer, Dordrecht. (2012). https://doi.org/10.1007/978-94-007-2467-9_5
[22] M. Shojaee, F. Navaee, S. Jalili–Firoozinezhad, R. Faturechi, M. Majidi and S. Bonakdar, Mater. Sci. Eng. C. **48**, 158–164 (2015). https://doi.org/10.1016/j.msec.2014.11.063
[23] G. Chhabra, M. Sayeed, M. Alshehri, S. Rab, S. Khan and T. Emran, Naunyn-Schmiedeberg's Arch. Pharmacol. 398, 2459–2485 (2025). https://doi.org/10.1007/s00210-024-03538-1
[24] S. Prasad, B. Patel, P. Kumar, J. Kaufman and Rajiv Lall, Vet. Sci. **12**, 514 (2025). https://doi.org/10.3390/vetsci12060514
[25] Y. Yan, H. Tao, J. He, and S-Y. Huang, Nat. Protoc. **15**, 1829–1852 (2020). https://doi.org/10.1038/s41596-020-0312-x

ДОСЛІДЖЕННЯ АМІЛОЇД – ПОЛІСАХАРИДНИХ КОМПОЗИТІВ МЕТОДОМ МОЛЕКУЛЯРНОГО ДОКІНГУ: І. ВЗАЄМОДІЇ З БІОЛОГІЧНО АКТИВНИМИ БІЛКАМИ ТА ПОЛІФЕНОЛАМИ

Валерія Трусова, Уляна Маловиця, Ольга Житняківська, Галина Горбенко
Кафедра медичної фізики та біомедичних нанотехнологій, Харківський національний університет імені В.Н. Каразіна м. Свободи 4, Харків, 61022, Україна

Амілоїдні фібрили — білкові агрегати з унікальною структурою — є новим типом наноматеріалів білкової природи з широким спектром застосувань. Одним із прикладів біомедичного застосування амілоїдних наноматеріалів є отримання біосумісних гідрогелевих покриттів для загоєння ран. Дане дослідження було спрямоване на оцінку можливості використання амілоїдних фібрил лізоциму, інтегрованих з полісахаридом хітозаном, в якості полімерного матриксу для інкорпорації агентів з вираженими ранозагоювальними властивостями, такими як поліфеноли та біологічно активні білки лактоферин та кональбумін. За допомогою методу молекулярного докінгу були визначені такі характеристики, як афінність, амінокислотний склад сайтів зв'язування та можливі конкурентні взаємодії між поліфенолами в двох-, трьох- та чотирьохкомпонентних системах. Виявлена здатність поліфенольних сполук до асоціації з біоактивними білками, при цьому найвища афінність спостерігалась для куркуміну в єнольній формі, кверцетину та сесаміну. У трьох- та чотирьохкомпонентних системах сайти зв'язування поліфенолів локалізувались або виключно на молекулах лактоферину чи кональбуміну, або ж містили амінокислотні залишки і фібрилярного лізоциму, і біоактивних білків. Встановлено, у яких комбінаціях поліфеноли можуть конкурувати між собою за сайти зв'язування. Отримані результати створюють основу для дизайну нових амілоїдних нанокомпозитів з ранозагоювальними властивостями.

Ключові слова: *амілоїдні фібрили лізоциму; хітозан; поліфеноли; лактоферин; кональбумін; сайти зв'язування; спорідненість зв'язування; молекулярний докінг*

East European Journal of Physics. 2. 594–599 (2026)
DOI: 10.26565/2312-4334-2026-2-66 ISSN 2312-4334

PHYSICS-INFORMED NEURAL NETWORK MODELING OF NONLOCAL CROWD DYNAMICS FOR EVACUATION SCENARIOS

A. Naumovets, **P. Kuznietsov**, **V. Cherkashyn**, **A. Gakh**
V.N. Karazin Kharkiv National University, 4 Svoboda Sq., Kharkiv 61022, Ukraine
**Corresponding Author e-mail: naumovets@karazin.ua*
Received March 2, 2026; revised April 23, 2026; accepted May 20, 2026

We investigate a nonlocal continuum model of crowd dynamics using a physics-informed neural network approach. The crowd is described by a system of nonlinear conservation laws in which the flux incorporates advection, diffusion, and nonlocal interaction terms accounting for density-dependent motion and limited perception of surrounding agents. Nonlocal effects are modeled through spatial convolutions with smooth kernels, enabling agents to respond to averaged density gradients rather than purely local information. The governing system of partial differential equations is solved using a physics-informed neural network known as PINN, which approximates the solution over the entire space–time domain while enforcing the physical constraints through automatic differentiation. The nonlocal interaction terms are implemented in a stable discrete convolution form, ensuring numerical robustness during training. The approach is demonstrated on the interaction of two pedestrian groups moving in opposite directions in a one-dimensional corridor. The results exhibit the formation and propagation of density fronts, the gradual merging of flows, and the emergence of stable mixed zones. A characteristic feature of the solution is the partial interpenetration of the groups without rigid collisions, reflecting realistic collective motion. To validate the method, the PINN solution is compared with a reference finite-difference scheme based on a Rusanov flux. Qualitative agreement is observed in front structure and mixing dynamics, while quantitative deviations in key characteristics remain within a few percent. A systematic parameter study shows that the PINN-based solution remains stable under variations of advection velocity, diffusion coefficient, and nonlocal interaction radius, in contrast to the finite-difference scheme, which exhibits strong stability limitations. These results demonstrate that PINN provides a robust and physically consistent tool for modeling nonlinear nonlocal crowd dynamics.

Keywords: *Physics-informed neural networks; Nonlocal crowd dynamics; Evacuation modeling; Advection-diffusion; Convolution kernels; Robustness; Complex geometries*

PACS: 07.05.Mh, 02.70.-c, 02.60.Cb

1. INTRODUCTION

With the increasing density of urban development, the growing number of mass events, and the risks associated with emergencies, there is an increasing need for effective methods to analyze collective motion and evacuation processes. Such problems require mathematical models that account for interactions among agents, the influence of environmental geometry, and the temporal evolution of density. From a mathematical perspective, collective motion can be described within a continuum framework using conservation laws for density. Such models have been developed since the 1970s [1] and have been successfully applied to describe pedestrian and traffic flows [2, 3, 4]. In more advanced formulations, nonlocal interactions are taken into account, where the motion is determined not only by the local density but also by its distribution in a surrounding neighborhood. This leads to the appearance of terms represented as integral convolutions with smooth kernels [5]. These models allow the incorporation of effects such as limited perception and the tendency to avoid regions of high density. Despite their physical consistency, nonlocal models pose significant challenges for numerical solution. The presence of integral terms increases computational complexity and complicates the stability of classical numerical schemes. Moreover, traditional discretization-based methods scale poorly when extended to higher-dimensional problems [6, 7].

In recent years, PINN has emerged as an alternative approach for solving differential equations [8], in which physical laws are directly embedded into the loss function of the neural network. This approach enables the computation of solutions without explicit domain discretization and naturally incorporates boundary and initial conditions. Further developments of the method focus on improving training stability and solution quality [9, 10]. Nevertheless, the application of PINN to nonlinear equations with nonlocal interactions remains insufficiently explored. In particular, the presence of convolution terms requires a dedicated implementation within the PINN framework and may significantly affect the stability and accuracy of the resulting solutions. In the present work, a crowd dynamics model is used as a representative example to investigate the applicability of PINNs to nonlocal equations of this type. One of the objectives is to assess the stability of the computational method and the reliability of the obtained solutions for such problems.

Cite as: A. Naumovets, P. Kuznietsov, V. Cherkashyn, A. Gakh, East Eur. J. Phys. 2, 594 (2026), https://doi.org/10.26565/2312-4334-2026-2-66

2. MODEL

We model the crowd as a continuum with density $\rho(t,x)$. When many agents of the same type move in similar directions, their motion can be treated statistically, and the overall crowd behaves like a compressible fluid. [1, 2, 3, 4] Accordingly, we adopt a conservation law (continuity equation)

$$\partial_t \rho + \nabla \cdot \mathbf{j} = 0, \tag{1}$$

where $\mathbf{j} = \rho \mathbf{u}$, and $\mathbf{u}$ is the velocity vector field. In contrast to an exact description involving a number of equations equal to the number of agents, this hydrodynamic approach allows for describing collective motion without tracking each person individually and significantly simplifies the mathematics of the problem, reducing the number of equations of motion to one.

To correctly represent the velocity of agents in a crowd, the direction and the magnitude of motion should be treated independently, in accordance with [5], was demonstrated that the dependence $v(\rho) = v_{\text{free}}(1 - \rho/\rho_{\max})$ reflects real behavior in a traffic jam. Here, $\rho_{\max}$ is associated with the finite size of the agents, and v_{free} is the maximum speed of free movement of the agents in the absence of crowding. In the considered scenario (in the absence of a crowd, agents, optimizing their direction of movement), move in the preferred direction $\mathbf{e}(x)$, which is unitary vector. The boundary conditions of movement in the corridor are $\mathbf{e} = \pm 1$, depending on whether the movement is left or right.

An attempt to avoid high-density areas is described by a vector $\mathbf{i}[\rho(x)]$. To model this behavior, it was proposed [5] to move along $-\nabla\rho$. In addition, in order to account for the radius of the agent's field of view, where it estimates the density, the density is averaged over a certain neighborhood with a smooth kernel η, which leads us to the following expression for $\mathbf{i}[\rho(x)]$

$$\mathbf{i}[\rho(x)] \;=\; -\,\varepsilon\,\frac{\nabla(\rho * \eta)(x)}{\sqrt{1 + \left\|\nabla(\rho * \eta)(x)\right\|^2}}, \qquad (\rho * \eta)(x) = \int_{-L}^{L} \rho(y)\,\eta(x-y)\,\mathrm{d}y, \tag{2}$$

where $*$ denotes spatial convolution with a kernel in the vicinity L. The coefficient $\varepsilon > 0$ controls the reaction strength: larger values correspond to stronger avoidance of crowded regions, while smaller values produce less sensitive trajectories. The denominator in (2) limits the magnitude of the deviation, preventing the reaction from becoming infinitely large. The natural presence of velocity dispersion among agents in a crowd is described by a diffusive flux term $\mathbf{q} = -D\,\nabla\rho$ Fick's law. Thus, total flux takes the form:

$$\mathbf{j} = \rho\, v(\rho)\,\big(\mathbf{e}(x) + \mathbf{i}[\rho(x)]\big) + \mathbf{q}, \tag{3}$$

being the non-linear expression in ρ. Totally, equation (1) for one type of agents takes the following form:

$$\partial_t \rho + \nabla \cdot \Big(\rho\, v(\rho)\big(\mathbf{e} + \mathbf{i}[\rho]\big)\Big) = D\,\Delta\rho, \tag{4}$$

here and further we omitt the notation of the dependence on (x).

The process of mixing flows of agents of two types is described by a system of equations of form (4). The mutual influence between agents of different types is accounted by the additional term in (3) of the form:

$$\mathbf{i}_k[\rho_l] \;=\; -\,\varepsilon_{k,l}\,\frac{\nabla(\rho_l * \eta_k)}{\sqrt{1 + \left\|\nabla(\rho_l * \eta_k)\right\|^2}}, \tag{5}$$

where $\varepsilon_{k,l}$ controls how strongly each group reacts to the local density of another group, and η_k defines the perceptual radius of the agents of type k where k and any other sub-indexes take values 1 and 2. Thus, the complete system describing the motion of the interacting groups is a nonlinear, nonlocal system of partial differential equations (PDEs) and has the following form:

$$\begin{cases} \partial_t \rho_1 + \nabla \cdot \Big(\rho_1\, v_1(\rho)\big(\mathbf{e}_1 + \mathbf{i_1}[\rho_1] + \mathbf{i_1}[\rho_2]\big)\Big) = D\,\Delta\rho_1, \\ \partial_t \rho_2 + \nabla \cdot \Big(\rho_2\, v_2(\rho)\big(\mathbf{e}_2 + \mathbf{i_2}[\rho_1] + \mathbf{i_2}[\rho_2]\big)\Big) = D\,\Delta\rho_2, \end{cases} \tag{6}$$

with $\rho = \rho_1 + \rho_2$ with Neumann boundary conditions corresponding to free outflow of agents. Developing PINNs for such systems is a central motivation of this work.

3. PINN COMPUTATION

The system equations (6) is a strongly nonlinear system of PDEs with nonlocal integral terms. We employ a PINN approach, originally introduced in [5] to solve it. The analysis is carried out on a space-time domain $0 \le x \le L$ with $L = 10$, and for times $0 \le t \le 9$. All variables and parameters in the model are expressed in dimensionless form. Before being passed into the neural network, the input coordinates are transformed using a Fourier feature embedding, which maps them to a higher-dimensional space using sinusoidal functions in order to improve the representation of

sharp spatial and temporal variations. This transformation affects only the neural network input representation and does not alter the governing equations. The maximum frequency of the Fourier features is set to $N_{\text{freq}} = 8$, which provides sufficient resolution of high-frequency solution components while maintaining training stability and avoiding unnecessary high-frequency modes that do not improve accuracy.

Here we present the implementation of the network consisting of 6 hidden layers with 256 neurons each, using the `tanh` activation function. The output layer contains two neurons corresponding to the two densities, and applies the `softplus` activation to ensure non-negativity of the predicted densities. All derivatives entering the equations are computed using TensorFlow's automatic differentiation. Direct integration inside the PINN, unlike differentiation, leads to instability during training. Therefore, the integral operator is rewritten in discrete form as a precomputed convolution matrix. This allows the integral term to be evaluated as a matrix multiplication, which remains differentiable and stable within the TensorFlow framework.

At the initial time, the crowd is assumed to form a configuration with well-defined boundaries. Therefore, the initial density distributions of the two agent groups are prescribed as localized super-Gaussian profiles.

$$\rho_i(x,0) = A_i \exp\left(-\left|\frac{x - x_i}{\sigma_i}\right|^{2m_i}\right) \tag{7}$$

where ρ_1 corresponds to the faster group and ρ_2 to the slower one. The slower group is initially located ahead of the faster group, such that interaction occurs only after a finite time interval. The boundary conditions correspond to an open-boundary problem with zero inflow at the left boundary and a free outflow at the right boundary. Training is performed in stages. During the first stage, the network is fitted to the initial and boundary conditions and to the correct conserved mass, establishing a stable baseline. Subsequently, the network progressively enforces the governing equations. By adjusting the weights in the loss function, we control the relative importance of the physical terms and suppress non-physical deviations, which improves the stability of the training process.

The PINN approach preserves the correctness of the solution across a wide range of physical parameters, since it does not rely on step-by-step temporal advancement and is not constrained by conditions such as the Courant–Friedrichs–Lewy restriction [11]. The neural network approximates the solution over the entire domain simultaneously, which makes the method robust to changes in velocity, the radius of nonlocal interaction, and diffusion coefficients.

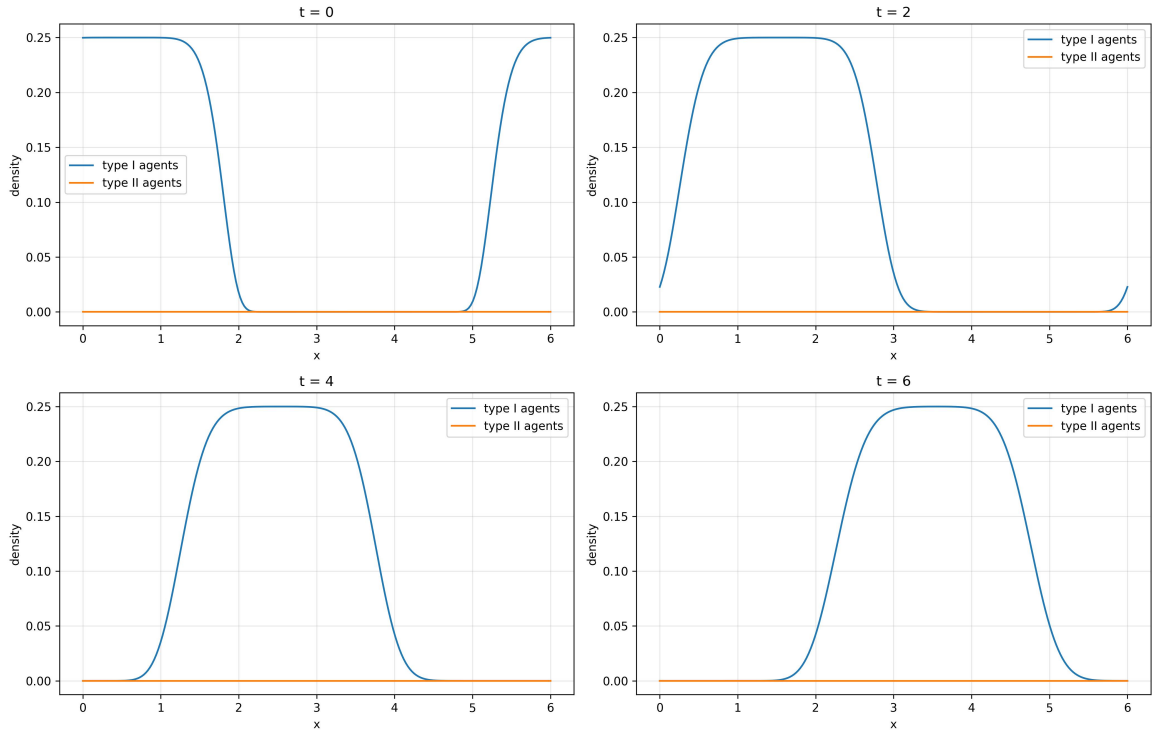

Figure 1. Motion of a single-type crowd

For clarity, and to illustrate the interaction effects between two groups, we first demonstrate that the numerical model correctly reproduces the dynamic of a single crowd moving along the corridor. The network is trained for 7000 epochs without further improvement in accuracy. Fig. 1 shows the spatial density profiles at time instants $t = 0.0$, 2.0, 4.0 and 6.0. The simulation was performed with parameters $A = 0.25$, $x = 0.6$, $\sigma = 1.2$, $m = 4$, and $v = 0.5$. As expected, the group moves as a whole.

Fig. 2 shows a qualitative change in the collective dynamics two groups of agents, that arises when a second is introduced. The second simulation was performed with parameters $A_{1,2} = 0.25$, $x_1 = 1.59$, $x_2 = 0.52$, $\sigma_{1,2} = 1.2$, $m_{1,2} = 4$, and $v_1 = 0.5$, $v_2 = 0.38$.

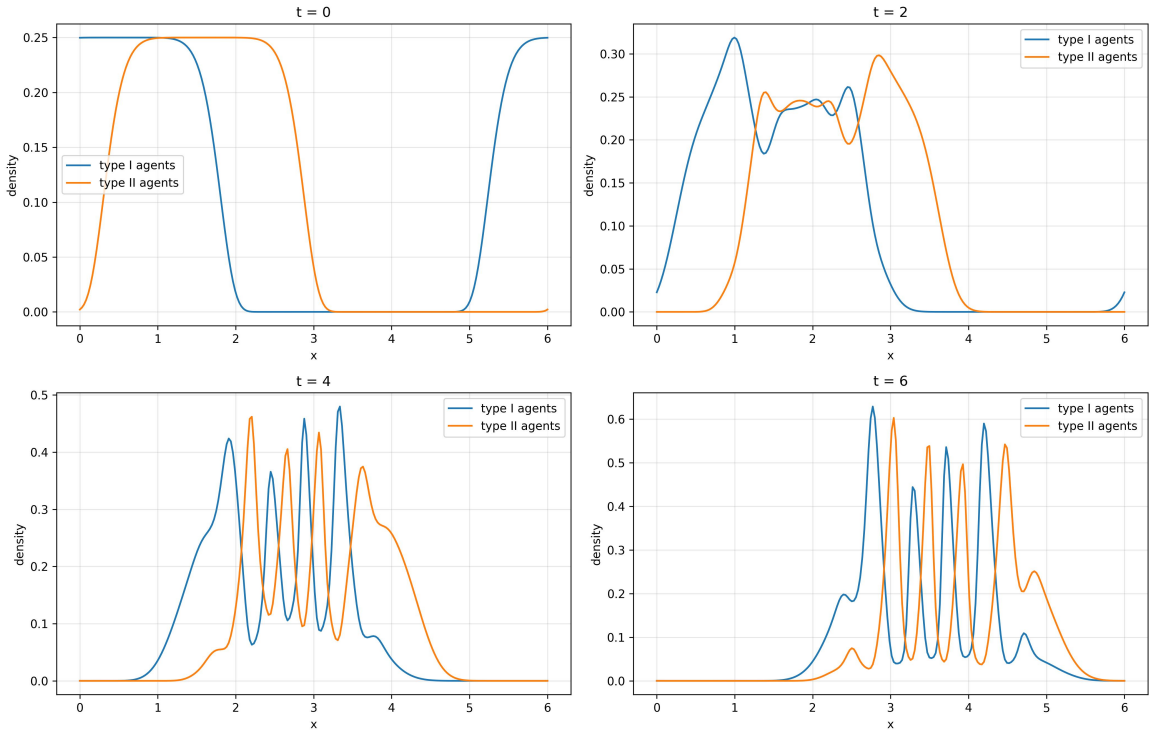

Figure 2. Spatial density profiles at selected time instants, illustrating the formation of quasiperiodic structures and interacting fronts. Both groups move in the positive direction of the x-axis, with the group of type I agents having a higher velocity.

The flow becomes fragmented into subgroups, and diffusive transport through low-density areas enables faster agents to overtake slower ones. As dispersion progresses, the overall density decreases, allowing unobstructed bypassing of slower agents and leading to the eventual disappearance of the periodic ordering. At the initial moment ($t = 0.0$), the faster group begins to catch up with the slower one. At the next stage ($t = 2.0$), the two groups already overlap significantly, and the difference in their preferred velocities leads to a deformation of the initial profiles and to the emergence of several local density maxima in the interaction zone. As the process develops further ($t = 4.0$), the model exhibits a characteristic phenomenon: the faster blue group gradually penetrates through the slower one, and quasiperiodic structures form. By $t = 6.0$ and beyond, this zone stabilizes into a broad segment that gradually shifts to the left, capturing mutual interpenetration and "pressing through" of the flows. The visualization demonstrates that the model reproduces key effects: gradual merging of flows, formation of compacted regions, and their subsequent displacement. The faster group overtakes the slower one and, after passing through it, forms a gap, a region of reduced total density. This behavior corresponds to the real behavior; people do not form a continuous medium; they can bypass, flow around, and partially pass through local clusters while maintaining their own speed, proving that social pressure and density allow for it.

The density fronts that emerge in the model have direct analogues in the physics of continuous media. Similar structures are formed, for example, in the exhaust plume of a jet engine: the hot jet, interacting with the surrounding air, creates zones of sharp density variation that move, stretch, flow around obstacles, and can partially "penetrate" through slower layers of the medium. These fronts are not rigid surfaces; they are dynamic transition zones where material moving at one speed enters the region of material moving at another speed. Similarly, in the crowd-motion model, the front represents a transition zone between two groups of people with different velocities and densities. It shifts, stretches, and can seep into the interior of the other group without an instantaneous equalization of speeds, reflecting the real kinematics of human movement.

Figure 3 presents the space-time diagrams of the densities $\rho_1(x,t)$ and $\rho_2(x,t)$. They demonstrate an evolutionary transition from an almost uniform distribution within each group to a quasiperiodic structure arising as a consequence of the interaction between the groups. As the process develops, alternating bands of higher and lower density are formed, with the density maxima of one group largely corresponding to the density minima of the other. This reflects a coordinated spatial modulation of the two interacting flows.

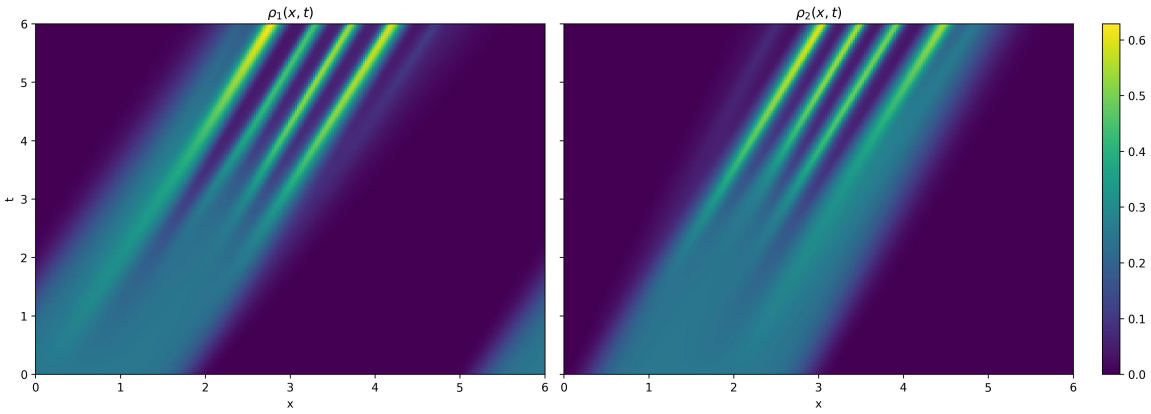

Figure 3. The space-time diagrams of the agent distributions in both groups

4. FDM VERIFICATION

1D, 2D problems without experimental data, with known parameters, are suited for solution by numerical methods such as the FDM. The model is discretized on a uniform one-dimensional grid, where the node values store the densities of the two groups. Thus, we deliberately considered simplefied problem in 1D to verify the PINN approach.

Both models, FDM and PINN, are run with identical initial conditions. The resulting density profiles, front positions, and mixing dynamics of the two groups are then compared. PINN reproduces the key features obtained by the FDM model: the shapes of the fronts and the interaction zones match visually, and the quantitative deviations remain small. To provide a qualitative assessment, we conducted simultaneous comparative runs for the FDM and PINN methods with initial conditions varying from $0.8 \cdot A_1$ to $1.2 \cdot A_1$. The relative discrepancies in the peak positions and front widths did not exceed 6% across all simulations considered. In addition, both models exhibited convergence under spatial grid refinement, which confirms the robustness of the obtained results and the consistency of the numerical implementation. Thus, the FDM framework serves as a reliable reference model against which the PINN demonstrates physically consistent behavior.

5. RESULTS ANALYSIS

The results demonstrate that PINN provides a stable and accurate reconstruction of solutions to nonlinear differential equations with nonlocal terms and remains operational over an extended parameter range. The obtained solution consistently reproduces the key dynamical features of two interacting pedestrian groups. At the initial moment the densities are fully separated, while during the evolution the faster group overtakes the slower one and forms a stable transition zone. This behavior realistic reflects pedestrian flow, where individuals partially interpenetrate rather than collide as rigid bodies.

The density fronts evolve without numerical artifacts: within the interaction region the gradients increase and then decrease smoothly. No nonphysical oscillations or discontinuities are observed. An analysis of temporal interaction areas shows that the deformation of the distribution remains regular and physically meaningful throughout the entire simulation interval. An examination of global characteristics shows that the front position, the width of the interaction areas, and the maximum density values change monotonically and without abrupt jumps, indicating a correct and stable reproduction of the nonlocal interaction mechanism.

Within the considered assumptions, the proposed PINN formulation demonstrates consistent performance. The structure of the method suggests applicability to more general problem classes beyond the present setting, including higher dimensions.

ORCID

A. Naumovets, https://orcid.org/0000-0001-6882-5672; **P. Kuznietsov**, https://orcid.org/0000-0001-8477-1395;
V. Cherkashyn, https://orcid.org/0009-0000-1975-8434; **A. Gakh**, https://orcid.org/0000-0002-1064-1448

REFERENCES

[1] L.F. Henderson, "The Statistics of Crowd Fluids," Nature, **229**(5284), 381–383 (1971). https://doi.org/10.1038/229381a0

[2] L.F. Henderson, "On the fluid mechanics of human crowd motion," Transportation Research, **8**, 509–515 (1974), https://doi.org/10.1016/0041-1647(74)90027-6

[3] N. Bellomo, and C. Dogbe, "On the Modeling of Traffic and Crowds: A Survey of Models, Speculations, and Perspectives," SIAM Review, **53**(3), 409 (2011). https://doi.org/10.1137/090746677

[4] R.L. Hughes, "A continuum theory for the flow of pedestrians," Transportation Research Part B: Methodological, 36(6), 507-535 (2002). https://doi.org/10.1016/s0191-2615(01)00015-7

[5] R.M. Colombo, and M. Lécureux-Mercier, "Nonlocal Crowd Dynamics Models for Several Populations," Acta Mathematica Scientia, **32**(1), 177-196 (2012). https://doi.org/10.1016/s0252-9602(12)60011-3

[6] R.J. LeVeque, *Finite Volume Methods for Hyperbolic Problems*, (Cambridge University Press, Cambridge, 2002), https://doi.org/10.1017/CBO9780511791253.

[7] J. P. Boyd, Chebyshev and Fourier Spectral Methods, (Dover Publications, Mineola, NY, 2001).

[8] M. Raissi, P. Perdikaris, and G. E. Karniadakis, "Physics-informed neural networks: A deep learning framework for solving forward and inverse problems involving nonlinear partial differential equations," Journal of Computational Physics, 378, 686–707 (2019). https://doi.org/10.1016/j.jcp.2018.10.045.

[9] A. D. Jagtap, E. Kharazmi and G. E. Karniadakis, "Conservative physics-informed neural networks on discrete domains for conservation laws: Applications to forward and inverse problems," Computer Methods in Applied Mechanics and Engineering, 365, 113028 (2020). https://doi.org/10.1016/j.cma.2020.113028.

[10] S. Wang, Y. Teng, and P. Perdikaris, "Understanding and mitigating gradient pathologies in physics-informed neural networks," Journal of Computational Physics, 449, 110768 (2021). https://doi.org/10.1137/20m1318043.

[11] R.J. LeVeque, and J. Randall, *Numerical Methods for Conservation Laws*, (Birkhäuser Verlag, Basel, 1992).

ФІЗИЧНО-ІНФОРМОВАНЕ НЕЙРОМЕРЕЖЕВЕ МОДЕЛЮВАННЯ НЕЛОКАЛЬНОЇ ДИНАМІКИ НАТОПУ ДЛЯ СЦЕНАРІЇВ ЕВАКУАЦІЇ

А. Наумовець, **П. Кузнецов**, **В. Черкашин**, **А. Гах**

Харківський національний університет імені В.Н. Каразіна, пл. Свободи, 4, Харків 61022, Україна

Ми досліджуємо нелокальну континуальну модель динаміки натовпу, використовуючи фізико-інформований нейронний мережевий підхід. Натовп описується системою нелінійних законів збереження, в яких потік включає адвекцію, дифузію та нелокальні члени взаємодії, що враховують рух, залежний від щільності, та обмежене сприйняття навколишніх агентів. Нелокальні ефекти моделюються за допомогою просторових згорток з гладкими ядрами, що дозволяє агентам реагувати на усереднені градієнти щільності, а не на суто локальну інформацію. Система диференціальних рівнянь з частинними похідними, що керує, розв'язується за допомогою фізико-орієнтованої нейронної мережі, відомої як PINN, яка апроксимує розв'язок по всьому просторово-часовому домену, одночасно дотримуючись фізичних обмежень за допомогою автоматичного диференціювання. Нелокальні члени взаємодії реалізовані у стабільній дискретній згортковій формі, що забезпечує числову стійкість під час навчання. Підхід демонструється на взаємодії двох груп пішоходів, що рухаються в протилежних напрямках в одновимірному коридорі. Результати демонструють формування та поширення фронтів щільності, поступове злиття потоків та виникнення стабільних змішаних зон. Характерною особливістю розв'язку є часткове взаємопроникнення груп без жорстких зіткнень, що відображає реалістичний колективний рух. Для валідації методу розв'язок PINN порівнюється з еталонною схемою скінченних різниць, заснованою на потоці Русанова. Якісна відповідність спостерігається у структурі фронту та динаміці змішування, тоді як кількісні відхилення в ключових характеристиках залишаються в межах кількох відсотків. Систематичне дослідження параметрів показує, що розв'язок на основі PINN залишається стабільним при змінах швидкості адвекції, коефіцієнта дифузії та радіуса нелокальної взаємодії, на відміну від схеми скінченних різниць, яка демонструє сильні обмеження стійкості. Ці результати демонструють, що PINN забезпечує надійний та фізично узгоджений інструмент для моделювання нелінійної нелокальної динаміки натовпу.

Ключові слова: *фізично-орієнтовані нейронні мережі; нелокальна динаміка натовпу; моделювання евакуації; адвекція-дифузія; ядра згортки; робастність; складні геометрії*

East European Journal of Physics. 2. 600-609 (2026)
DOI:10.26565/2312-4334-2026-2-67 ISSN 2312-4334

THE THEORY OF THE IDEAL ARMOR PLATE. ENERGY REGULARITIES OF THE HIGH-SPEED BODY IMPACT ON AN ARMOR PLATE

M.P. Odeychuk, I.V. Tkachenko, V.I. Tkachenko*
National Science Center «Kharkiv Institute of Physics and Technology»,1 Akademicheskaya St., Kharkiv, 61108, Ukraine
**Corresponding Author e-mail: tkachenko@kipt.kharkov.ua*
Received January 14, 2026; revised March 20; 2026; accepted May 12, 2026

This study analyzes the optimal energy characteristics of a flying body (FB) impacting an armor plate (AP). The considered energy characteristics include momentum, kinetic energy, and the power of both bodies. It is shown that only a small fraction of the FB momentum is transferred to the AP, whereas nearly all of the FB kinetic energy is converted into the internal energy of the AP. This internal energy consists of the energy of mechanical oscillations of the plate and the energy associated with material displacement within it. The energy of the natural oscillations of the AP, modeled as a rectangular parallelepiped with dimensions a, b(with $a \sim b$) and thickness c, is estimated. The frequencies of bending oscillations perpendicular to and along the plate surface are calculated. It is shown that the energy of bending oscillations along the surface with the largest area exceeds that of oscillations perpendicular to the surface by a factor of a^2/c^2. The transfer of the FB kinetic energy is assumed to occur in a cylindrical channel of base area S_0. It is shown that the maximum power transferred from the FB to the AP is equal to $16/27 \approx 0.5926$ of the initial FB power and is accompanied by a reduction of the FB velocity by a factor of three. The characteristic penetration length corresponding to maximum power loss is proportional to the FB length h. The multilayer AP configuration is also considered. It is shown that in subsequent layers with lower material density, conditions for maximum power loss are preserved. The thickness of each layer is determined by the distance over which maximum power loss occurs. The results indicate that properly designed multilayer APs can significantly reduce overall dimensions and weight while maintaining high protective efficiency. It should be noted that the present analysis is qualitative and does not aim at quantitative agreement with experimental data, as some secondary effects are neglected. The results provide a physical basis for understanding energy dissipation mechanisms and suggest directions for further optimization using numerical methods.
Keywords: A*rmor plate; Flying body; Impact; Energy; Power loss; Multilayer*
PACS: 46.40.-f, 46.55.+d,81.40.Lm

INTRODUCTION

In recent years, due to the increasing number of military conflicts and localized hostilities, the problem of protecting personnel and equipment from high-speed projectiles has become especially relevant. This topic has been extensively studied and is widely covered in monographs, scientific publications, and textbooks. Typically, such works describe different types of ammunition, their key parameters, and their penetration capabilities (see, for example, [1–3]).

After introducing the properties of projectiles, various methods for analyzing their interaction with protective barriers are considered. One common approach is the use of empirical relationships derived from extensive experimental data on projectile impact and penetration. These relationships provide practical estimates of penetration depth and energy absorption.

In addition to empirical approaches, analytical models have been developed to describe projectile motion within a target as a combination of functions that account for projectile design, the barrier's material properties, and interaction conditions. Although such models can be reasonably accurate within their domain of applicability, they often remain closely related to empirical formulas and may be insufficient to solve advanced design problems.

Another important class of methods is based on continuum mechanics. These approaches rely on conservation laws of mass, momentum, and energy and are typically implemented using finite-difference or finite-element numerical techniques. Such methods provide a more physically grounded description of high-speed impact processes and allow detailed analysis of stress, deformation, and failure mechanisms.

Nevertheless, regardless of the modeling approach, experimental validation remains the primary criterion for assessing model accuracy. Numerous studies demonstrate that existing theoretical and numerical methods can adequately reproduce experimental results under appropriate conditions.

Modern research on improving the protective performance of armor systems increasingly focuses on multilayer and composite materials. For example, composite armor consisting of Al_2O_3 ceramics and ultra-high-molecular-weight polyethylene (UHMWPE) has demonstrated significant improvements in energy absorption [4]. Optimizing layer thickness and configuration can lead to substantial gains in ballistic resistance.

Similarly, studies of laminated aluminum alloys have shown that enhanced ballistic performance can be achieved by increasing energy dissipation through plastic deformation and delamination [5]. Lightweight protective structures based on aluminum alloys have also been proposed, with modeling approaches demonstrating good predictive capability under high strain-rate conditions [6].

A common drawback of many existing approaches is the need for extensive numerical computations to achieve optimal performance, particularly when maximizing energy absorption while minimizing weight. This limitation can be

Cite as: M.P. Odeychuk, I.V. Tkachenko, V.I. Tkachenko, East Eur. J. Phys. 2, 600 (2026), https://doi.org/10.26565/2312-4334-2026-2-67

addressed by introducing an additional optimization criterion that maximizes the projectile's power-loss rate during penetration.

The aim of the present work is to develop a theoretical framework for an ideal armor plate that maximizes the energy dissipation of a high-speed flying body. The proposed approach identifies key energy-loss mechanisms and establishes conditions under which the penetration depth is minimized while the projectile's power loss is maximized. This framework can serve as a basis for further refinement using numerical simulations and experimental validation.

1. GENERAL POSITIONS

When a flying object strikes an armored structure, the primary focus is on analyzing the structure's strength and reliability. AP with various geometric dimensions can serve as armored structures. The thickness, width, and height of APs can vary widely, but they generally have the form of rectangular parallelepipeds with a volume of $V = Sc$, where $S = ab$ is the maximum cross-sectional area of the AP, a and b are the length and width of the AP, respectively, and c is the thickness of the AP. The AP material is characterized by density $\rho = M/V$, where M is the mass of the AP.

The AP material is a single-layer or multi-layer metal plate whose elastic properties are characterized by Young's modulus E, strength by the tensile strength of the metal or its composition σ_B, and flow stress $\sigma_{0.2\%}$.

The FB is, in turn, also a metallic object, often of complex shape and composition. The FB is characterized by geometric dimensions comparable to the base plate's thickness. The volume of the FB has a cylindrical form and is equal to $V_0 = S_0 h$, where S_0 is the base of the cylinder and h is its height.

The density of the material FB is equal to $\rho_0 = m/V_0$, and the velocity is directed perpendicular to the maximum cross-sectional area AP and is equal to u_0.

In its simplest form, the FB material is a single-layer or multi-layer metal cylinder, the elastic properties of which are characterized by Young's modulus E^*. Strength is determined by the tensile strength of the cylinder's metal or metal composition σ_B^*, as well as the flow stress $\sigma_{0.2\%}^*$.

1.1. Energy Characteristics of the FB

The FB is characterized by the momentum M_{fb}:

$$M_{fb} = mu_0, \tag{1}$$

and kinetic energy W_{fb}:

$$W_{fb} = \frac{mu_0^2}{2}. \tag{2}$$

The power of the FB is determined by the expression:

$$P_{fb} = \frac{\rho_0 S_0 u_0^3}{2}. \tag{3}$$

The energy characteristics of the FB are momentum, kinetic energy and transferred power.

1.2. Processes of Transfer of Energy FB to Energy AP

The impact of the FB on the AP leads to an increase in the momentum and kinetic energy of the AP, as well as mechanical oscillations of the AP.

Furthermore, there will be an increase in the AP temperature in the region of the FB's impact, limited to an area of approximately S_0. This localized temperature increase has been confirmed in many experiments studying the impact of the FB on the AP (see, for example, [3]). The localized temperature increase is so great that over an area of approximately S_0, the metal liquefies. In this case, we will consider a situation in which the depth of metal melting is approximately equal to the AP thickness. Otherwise, the AP is not pierced, and it performs its intended function. Therefore, we will not consider this case further.

Based on the above, when analyzing the energy characteristics of the AP, we will assume that two energy absorption processes are occurring simultaneously.

One process involves the absorption of energy by the entire volume of AP.

The second process is associated with the absorption of energy by the FB in a cylindrical channel of area S_0.

1.3. Transfer of the FB Energy into Oscillatory Energy of the Entire AP Volume

When FB impacts an AP, its kinetic parameters must be analyzed. These include the AP's momentum, kinetic energy, and power.

The AP's momentum M_{ap} is determined by the expression:

$$M_{ap} = Mw \tag{4}$$

where w is the AP velocity.

The kinetic energy of the AP W_{ap} is equal to:

$$W_{ap} = \frac{Mw^2}{2}. \quad (5)$$

The power of the AP P_{ap} is determined by the formula:

$$P_{ap} = \frac{\rho S w^3}{2}. \quad (6)$$

To determine the energy of mechanical oscillations of bending AP, we will proceed from the fact that the oscillations are subject to a rectangular plate with supported edges, whose edges only rest on a fixed support, but are not attached to it. We will determine the lowest frequency ω_{ap} of the bending oscillations of a rectangular plate for a neutral surface on which there is no tension. We will define the shape of the neutral surface by the expression $\zeta(x, y, t) = h_{ap} sin(k_x x) sin(k_y y) sin(\omega_{ap} t)$, where h_{ap} is the bending amplitude, $k_x = \pi/a$, $k_y = \pi/b$ are the wave numbers of oscillations in the x and y directions, $\omega_{ap} = 2\pi/T$, T is the period of the bending oscillations of the AP [7]. The magnitude of the frequency ω_{ap} is determined by the expression:

$$\omega_{ap} = \sqrt{\frac{Ec^2}{12\rho(1-\nu^2)}}\left[\left(\frac{\pi}{a}\right)^2 + \left(\frac{\pi}{b}\right)^2\right], \quad (7)$$

where ν is Poisson's ratio.

From [7], we determine the average kinetic energy of bending oscillations AP over the oscillation period T. It is determined by the expression:

$$\Omega_{ap} = \frac{\pi^4}{192}\frac{Ec^3 h_{ap}^2}{(1-\nu^2)}\left(\left(\frac{1}{a}\right)^2 + \left(\frac{1}{b}\right)^2\right)^2 ab, \quad (8)$$

Deviations of the surface of the AP from the equilibrium position caused by mechanical oscillations lead to an elongation ε, the value of which is determined by the expression:

$$\varepsilon = \frac{\pi}{4}\frac{h_{ap}^2}{a^2}. \quad (9)$$

Expression (8) allows us to determine the plasticity region of each AP, since exceeding the critical elongation value can lead to AP failure. In each specific case, such calculations must be performed to assess the AP's shape retention.

2. ENERGY TRANSFER FROM THE FB

When considering the energy transfer of the FB to AP, it is always important to know the answers to the following questions:

1. What is the minimum initial penetration velocity of the AP.
2. What changes in momentum and energy occur between interacting objects.
3. What are the conditions for loss of maximum power by FB.
4. What are the requirements for the multilayer AP?

Some of these questions are answered in the dissertation [8] and in the monograph [3].

In the dissertation [8], a general concept for barrier penetration is defined based on an analysis of high-velocity impact processes and armor penetration of various materials. This concept is based on the principle of redistributing the kinetic energy of an impact between the surface area of contact and the barrier's deep penetration. Using the proposed concept, the effects of ultra-deep penetration of micro-impactors under critical impact conditions are described.

However, the data in [3, 8] and many other sources not cited in this paper are not always readily available and require additional calculations. Therefore, answers to the questions posed are proposed below, formulated based on conservation laws.

2.1. A Minimum Initial AP Penetration Velocity

Based on the strength characteristics of the AP and the energy parameters of the FB, it is possible to formulate a condition for AP penetration. This condition is the requirement that the FB pressure on the AP surface exceeds the resistance force, which is determined by the flow stress $\sigma_{0.2\%}$:

$$\frac{1}{2}\rho_0 u_0^2 > \sigma_{0.2\%}. \quad (10)$$

To inequality (10) it is necessary to add the condition of smallness of the speed FB compared to the speed of sound c_s in the material AP:

$$u_0 < c_s. \quad (11)$$

From (10) and (11) we obtain the condition for the value of the speed FB at which the penetration of the AP occurs:

$$u_{0,min} = \frac{2\sigma_{0.2\%}}{\rho_0 c_s} < u_0 < c_s \tag{12}$$

The minimum speed $u_{0,min}$ of penetration of the AP is determined by the lower limit of inequality (12).

2.2. The Momentum and Energy of Interacting Objects Changing

The kinetic energy and momentum of the FB will be transferred to the entire AP, as well as to the material located in a cylindrical channel of area S_0. When the FB impacts the material in a cylindrical channel of area S_0, it can be assumed that a cork is formed, which can be squeezed out of the AP volume. Due to various dissipative processes (viscosity, thermal heating, and friction of the cork against the walls of the cylindrical channel), incomplete energy and momentum transfer between the FB and the cork should be observed.

Due to the high energy of the FB and the significant difference in the masses of the AP and FB, it can be concluded that the laws of conservation of energy and momentum are approximately satisfied. In a perfectly inelastic collision, the velocity of the AP after the interaction is equal to $\widehat{w}$ and is determined by the expression:

$$\widehat{w} \approx \frac{m}{(m+M)} u_0. \tag{13}$$

In a perfectly inelastic collision, the FB gets stuck in the AP, and the FB loses kinetic energy ΔW:

$$\Delta W = \frac{mu_0^2}{2} - \frac{(m+M)\widehat{w}^2}{2} = \frac{M}{M+m}\frac{mu_0^2}{2}. \tag{14}$$

Since $m \ll M$, practically all kinetic energy is converted into internal energy of the AP. The ratio $M/(M+m)$ determines the proportion of the FB kinetic energy converted into internal energy AP.

2.3. Conditions for Maximum Power Loss of the FB

To evaluate the efficiency of AP use, it is necessary to determine the conditions under which the FB power loss is maximum. For this, we will consider the energy exchange per unit of time between the FB and the cork in a cylindrical channel AP of area S_0.

Per unit of time, the following mass passes through the area S_0:

$$\dot{m} = \rho_0 S_0 \acute{u_0}, \tag{15}$$

where $\acute{u_0}$ is an average speed FB, and the dot above the letter means the time derivative.

The power transferred to the cork is estimated by the value:

$$P_{cork} = \frac{\dot{m}}{2}\left(u_0^2 - u_{0,fin}^2\right), \tag{16}$$

where $u_{0,fin}$ is the final velocity of the FB in the channel.

At the same time, the power consumption of the FB can be defined as the product of the resistance force F and the average speed of the FB:

$$\acute{P_{fb}} = F\acute{u_0}, \tag{17}$$

The resistance force can be estimated by the value:

$$F = \dot{m}\left(u_0 - u_{0,fin}\right), \tag{18}$$

From (16), (17), and (18) it follows that the average speed is equal to:

$$\acute{u_0} = \frac{1}{2}\left(u_0 + u_{0,fin}\right). \tag{19}$$

From (16), we obtain a function that describes the dependence of the FB power on the speed together with the cork:

$$\begin{aligned} P_{cork} &= \frac{1}{2}\rho_0 S_0 \acute{u_0}\left(u_0^2 - u_{0,fin}^2\right) = \frac{1}{2}\rho_0 S_0 \frac{1}{2}\left(u_0 + u_{0,fin}\right)\left(u_0^2 - u_{0,fin}^2\right) \\ &= \frac{1}{4}\rho_0 S_0 u_0^3 \left(1 + \frac{u_{0,fin}}{u_0}\right)\left(1 - \frac{u_{0,fin}^2}{u_0^2}\right). \end{aligned} \tag{20}$$

Analysis (20) shows that the maximum power will be transferred to the cork in a cylindrical channel provided that the final velocity satisfies the condition: $u_{0,fin} = u_0/3$. In this case, the lost power FB is equal to:

$$(P_{cork})_{max} = \frac{1}{2}\rho_0 S_0 u_0^3 \frac{16}{27} = \eta \cdot (W_{cork})_0. \quad (21)$$

where $(P_{cork})_0 = \rho_0 S_0 u_0^3 /2$ is the initial power of FB, $\eta = 16/27 \approx 0.5926$ is the power transfer coefficient.

The coefficient η coincides with the condition of A. Betz, which determines the maximum efficiency of a wind turbine [9].

Let us determine the distance at which this velocity FB decreases by a factor of three, i.e. $u_{0,fin} = u_0/3$. To do this, we write the equation of displacement of the contact boundary of FB of mass m with the cork:

$$\frac{du_0}{dt} = -\frac{1}{h}(u_0 + u_{0,fin})\left(u_0 - \frac{1}{2}u_{0,fin}\right) \quad (22)$$

Using the substitution $t = x/u_{0,fin}$, where x is the coordinate of the location of the contact boundary of the FB with the cork, we transform the equation to the form:

$$\frac{dy}{dx} = -\frac{1}{h}(y+1)\left(y - \frac{1}{2}\right) \quad (23)$$

where $y = u_0/u_{0,fin}$.

The solution to equation (23) is a function of the form:

$$y(\xi) = \frac{1}{2}\frac{\left(1 + 2e^{-\frac{3}{2}(\xi+\xi_0)}\right)}{\left(1 - e^{-\frac{3}{2}(\xi+\xi_0)}\right)} \quad (24)$$

where $\xi = x/h$ is the distance at which the FB loses its maximum power, ξ_0 is the integration constant.

The constant ξ_0 is determined from the condition that $y(\xi)$ should change three times over the distance of maximum power loss, for example, from $y(0) = 3^{n+1}$ to $y(z_{1,n}) = 3^n$, where the condition $n \gg 1$ must be fulfillment.

Calculations using formula (24) show that a decrease in the initial velocity FB by 3 times is observed at a distance of:

$$z_{1,n} = \frac{2}{3} ln\left[\frac{(3^n+1)}{(3^n-0.5)}\frac{(3^{n-1}-0.5)}{(3^{n-1}+1)}\right] \quad (24, a)$$

Thus, a threefold decrease in speed with a maximum loss of power FB occurs at a distance $x_n = z_{1,n}h$, where n is selected based on the realism of the obtained distance and experimental data.

2.4. Requirements for Ideal Multilayer AP

Ideal multilayer APs are those that provide maximum FB power loss. To calculate the ideal AP, for example, we'll compile Table 1, which lists the characteristic FB and AP parameters.

Table 1. Mass, geometric, strength, kinematic and energy characteristics of FB and AP

Parameter name	AP	FB
Mass, *kg*	M	m
Base area, m^2	$S = ab, (a\ -\ \text{length}, m;\ \ b\ -\ \text{width}, m)$	S_0
Thickness/length, *m*	c	h
Volume, m^3	$V = Sc$	$V_0 = S_0 h$
Density, kg/m^3	ρ	ρ_0
Young's modulus, *MPa*	E	E^*
Tensile strength, *MPa*	σ_B	σ_B^*
Flow stress, *MPa*	$\sigma_{0.2\%}$	$\sigma_{0.2\%}^*$
Velocity, *m/s*	w	u_0
Momentum, $kg\cdot m/s$	M_{ap}	M_{fb}
Kinetic energy, *J*	W_{ap}	W_{fb}
Power, $kg\cdot m^2/s^3$	P_{ap}	P_{fb}

When describing the impact of the FB on the AP, we distinguish two main processes:
- transfer of the FB momentum and energy to the entire volume of the AP;

- transfer of the FB energy to the AP material in a cylindrical channel of area S_0, which is formed by the high-energy pulsed impact of the FB on the AP.

The energy indicators of these processes are summarized in Table 2, where the characteristic indicators of energy transfer FB to the entire volume of the AP (Transfer I) and the characteristic indicators of energy transfer FB in the AP in a cylindrical channel with the base S_0 (Transfer II) are highlighted.

Table 2. Characteristic indicators of optimal energy transfer from the FB to the AP

Parameter name	Transfer I	Transfer II
Frequency of mechanical oscillations of bending of a rectangular plate, s^{-1}	ω_{ap}	–
Amplitude of mechanical oscillations of the AP bending, *m*	h_{ap}	–
Energy of bending AP oscillations with amplitude h_{ap}, $kg\cdot m^2/s$	Ω_{ap}	–
Elongation due to mechanical oscillations AP, dimensionless	ε	–
Velocity, *m*/*s*	$\widehat{w} \ll u_0$	u_0
Power, $kg\cdot m^2/s^3$	$P_{ap} \ll P_{fb}$	P_{cork}
Final speed of the FB at maximum power transfer, *m*/*s*	–	$\frac{1}{3}u_0$
One-time distance of maximum power loss of the FB, *m*	–	$z_{0,n}h$

The previous section described the conditions for the loss of maximum power FB in a single-layer AP, which corresponds to the ideal single-layer AP.

Below we will consider the requirements for ideal multilayer AP.

From (24) it follows that for a given n, at a distance $z_1 = z_{1,n}$, the maximum power loss of the FB is observed. For a single-layer AP, this power loss may be insufficient, and the FB will continue its movement with an undesirable result. Therefore, the question arises of using a second, and if that doesn't help, a third, or even more layers of AP. The answer to this question is contained in the results obtained for the first AP layer.

The expression for the maximum power loss (21) contains only the material density FB, the cross-section, and the velocity of the FB. Therefore, to estimate the optimal distance for the loss of maximum power in the second layer, the previous consideration is applicable, where a threefold decrease in the velocity of the FB with the loss of maximum power will already occur at a distance $z_2 = z_{1,n-1}$.

Fig. 1 shows a diagram for calculating the location of the first two layers of the AP when the FB passes with an initial velocity u_0 with a AP thickness equal to c. Position I is the moment the FB enters the AP, position II is the moment the first layer of the AP with thickness z_1 is formed, position III is the moment the second layer of the AP with thickness z_2 is formed.

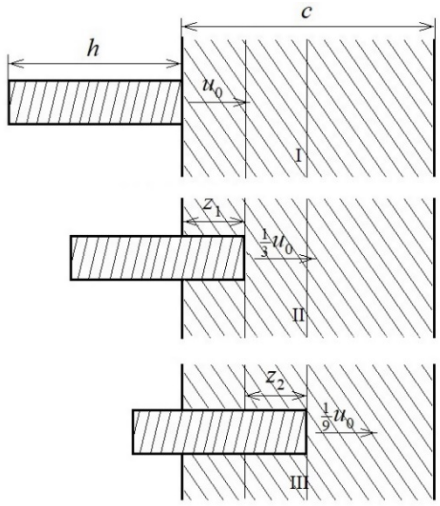

Figure 1. Schematic diagram of the arrangement of the first two layers of the AP as the FB of length h passes with an initial velocity u_0 at AP thickness equal to c

In the third layer of the AP, a threefold decrease in speed will occur at a distance $z_3 = z_{1,n-2}$.

Summing up these distances, we obtain the total thickness of the N - layer AP, at which the speed of the FB will change by 3^N times:

$$x_n \approx z_{1,n} + z_{1,n-1} + z_{1,n-2} + \cdots \tag{25}$$

Thus, for example, for $n = 4$ and for a three-layer AP ($N = 3$), there is a 27-fold decrease in the velocity of the FB over a length of $x_3 = 0.024 + 0.072 + 0.205 = 0.301$ and a loss of $\Delta U_3 = \eta + (1 - \eta)\,\eta + (1 - \eta - (1 - \eta)\,\eta)\,\eta \approx 0.932$ of the part of the initial power of the FB.

If the number of layers is large, i.e. $n \gg 1$, then the total power loss of the FB tends to unity, since the power losses in layers are determined by the expressions:

1 layer – η;

2 layer - $(1 - \eta)\,\eta$;

3 layer - $(1 - \eta - (1 - \eta)\,\eta)\,\eta$;

4 layer - $(1 - \eta - (1 - \eta)\,\eta - (1 - \eta - (1 - \eta)\,\eta)\,\eta)\eta$;

The total power loss is determined by an infinite decreasing geometric progression:

$$\Delta P_{n\to\infty} = \eta + (1 - \eta)\,\eta + (1 - \eta - (1 - \eta)\,\eta)\,\eta + (1 - \eta - (1 - \eta)\,\eta - (1 - \eta - (1 - \eta)\,\eta)\,\eta)\eta$$

$$+ \cdots = \eta[1 + (1 - \eta) + (1 - \eta)^2 + (1 - \eta)^3 + \cdots] = \eta\,\frac{1}{1 - (1 - \eta)} = 1.$$

From the calculations carried out it follows that in order to lose the maximum power of the FB in a multilayer AP, it is necessary to select the thickness of the layers in accordance with (25), where each term determines the thickness of the layers from the first $z_{0,n}$ to the second $z_{0,n-1}$, the third $z_{0,n-2}$, and so on.

For example, for an initial velocity of the FB 600 *m/s* and a minimum penetration velocity of 58.5 *m/s*, calculated using formula (12), it is sufficient to use a two-layer AP, since in a two-layer AP the velocity of the FB decreases by 9 times.

Since the density of the AP material is not included in the calculation of maximum power loss, subsequent layers of the AP can be composed of a lower-density material to lighten the structure. The optimal number and sequence of lightweight layers placed after the first layer should be determined experimentally.

3. NUMERICAL ESTIMATES OF THE IMPACT OF FB ON AP

Let us present numerical estimates of FB's impact on the AP. The initial data will be the average FB velocities and the characteristic AP parameters corresponding to the 7.62 *mm* AKM 7.62 *mm* PS bullet of the 1943 model 57-H-231 cartridge in a steel shell with a steel core, weight 7.9 *g*, with an initial velocity of 730 *m/s* [3].

As stated above, the FB has two channels of momentum, energy, and power loss.

These losses are as follows:

- losses due to the transfer of momentum and energy of the FB to the entire volume of the power supply.
- losses caused by the transfer of energy FB to the AP material in a cylindrical channel with the base S_0. The channel is formed by the high-energy pulsed action of the FB on the AP.

Let's first estimate the momentum and energy transfer of the FB to the entire volume of the AP. We'll assume that the angle α between the FB axis and the normal to the AP is equal to zero. Increasing this angle increases the AP thickness and improves the APs protective properties. Table 3 presents the characteristic parameters of the FB and AP steel, taken from [3].

Table 3. Characteristic mass, geometric, strength, kinematic, and energy parameters of FB and AP

Parameter name	AP	FB
Mass, *kg*	$M = 2.18$	$m = 7.9 \cdot 10^{-3}$ 7.62mm Kalashnikov assault rifle (AKM), steel core
Base area, m^2	$S = ab = 0.2 \times 0.2 = 4 \cdot 10^{-2}$, $(a$ – length, м; b – width, м)	$S_0 = 4.56 \cdot 10^{-5}$
Thickness, м	$c = 7 \cdot 10^{-3}$	$h = 2.68 \cdot 10^{-2}$
Volume, m^3	$V = Sc = 2.8 \cdot 10^{-4}$	$V_0 = S_0 h = 1.22 \cdot 10^{-6}$
Density, kg/m^3	$\rho = 7810$	$\rho_0 = 7810$
Young's modulus, *MPa*	$E = 2.15 \cdot 10^5$	$E^* = 2.15 \cdot 10^5$
Tensile strength, *MPa*	$\sigma_B = 30060$	$\sigma_B^* = 30060$
Flow stress, *MPa*	$\sigma_{0.2\%} = 1370$	$\sigma_{0.2\%}^* = 1370$
Poisson's ratio,	$\sigma = 0.33$	$\sigma = 0.33$
Rate of plastic deformation, s^{-1}	$\dot{\varepsilon} = 5 \cdot 10^4$	$\dot{\varepsilon} = 5 \cdot 10^4$
Sound velocity, *m/s*	$c_s = 5900 \ldots 6100$	$c_s = 5900 \ldots 6100$

Parameter name	AP	FB
Velocity, *m/s*	$w = 0$	$u_0 = 600 \cdots 745$
Momentum, *kg· m/s*	$M_{ap} = 0$	$M_{fb} = 4.74 \ldots 5.9$
Kinetic energy, *kJ*	$W_{ap} = 0$	$W_{fb} = 1.422 \ldots 2.192$
Power, *MW*	$P_{ap} = 0$	$P_{fb} = 38.5 \ldots 73.6$

It should be noted that given such a huge energy input and the rapidity of the processes, not all the coefficients in Table 3 are valid. However, we will assume that they are of the same order of magnitude. The true values of these coefficients must be determined experimentally.

4. TRANSFER OF THE FB ENERGY INTO ENERGY OF THE ALL VOLUME OF THE AP

Penetration and energy transfer from the FB to the energy of the entire volume of the AP is possible at a velocity FB satisfying condition (12). In numerical expression for the parameters of Table 3, this velocity value must satisfy the inequality:

$$58.5 < u_0 < 6000, m/s. \tag{26}$$

From the law of momentum conservation, we estimate the acquired speed by the AP:

$$\widehat{w} = \frac{7.9 \cdot 10^{-3} \cdot 600}{2.18} \approx \frac{mu_0}{M} = 2.17, m/s \tag{27}$$

Thus, the displacement of the AP during the incident is of the order of $\widehat{w}/\dot{\varepsilon} \sim 10^{-5}$ *m* and represents a very small value. The acquired kinetic energy of the AP is of the order of:

$$W_{ap} = \frac{M\widehat{w}^2}{2} \approx 1.09 \cdot 4.7 \approx 5.13, \qquad J. \tag{28}$$

The power received from the FB to the AP is determined by the value:

$$P_{ap} = \frac{M\widehat{w}^3}{2c} \approx \frac{2.18 \cdot 10.22}{2 \cdot 7 \cdot 10^{-3}} = 1.59 \cdot 10^3, \ W. \tag{29}$$

The kinetic energy (28) and power (29) acquired by the AP are small values relative to the initial values for FB: $W_{fb} \approx 0.5 \cdot 7.9 \cdot 10^{-3} 600^2 = 1.422\ kJ$ and $P_{fb} \approx 0.5 \cdot 7.810 \cdot 4.56 \cdot 10^{-2} 600^3 \approx 3.85 \cdot 10^7\ W$. Therefore, the change in the kinetic energy (28) and power (29) of the AP can be ignored when analyzing the energy exchange between the FB and the AP.

As shown above, the analysis of energy exchange between the FB and the AP includes an estimate of the power (21) converted into the AP's internal energy and an estimate of the distance over which this transition occurs (24).

A certain portion of the FB kinetic energy is also converted into the internal energy of the mechanical oscillations of the AP. Below, we present a numerical estimate of the energy and associated parameters transferred to the AP's mechanical oscillations.

4.1. Elongation, Frequency, and Energy of Mechanical Bending Oscillations According to Thickness c

Below, based on formulas (7), (8), (9), and the data in Table 3, are numerical estimates of the elongation (30.1), frequency (30.2), and energy of mechanical oscillations of bending across thickness c (30.3) under the condition $a \sim b$:

$$\varepsilon_c = \frac{\pi}{4} \frac{h_{ap}^2}{a^2}, \tag{30.1}$$

$$\omega_{ap} = \sqrt{\frac{Ec^2}{12\rho(1-\nu^2)}} \left[\left(\frac{\pi}{a}\right)^2 + \left(\frac{\pi}{b}\right)^2 \right] = 5.546 \cdot 10^3, \ s^{-1} \tag{30.2}$$

$$\Omega_{ap} = 2.03 \frac{2.15 \cdot 10^5 (7 \cdot 10^{-3})^3}{(1 - 0.89)} \frac{h_{ap}^2}{4 \cdot 10^{-2}} \approx 1.68 \cdot 10^5 \frac{h_{ap}^2}{a^2} = 1.68 \cdot 10^5 \frac{4}{\pi} \varepsilon_c, \qquad J. \tag{30.3}$$

In addition to mechanical bending oscillations along thickness c, similar flexural vibrations may also exist along length a. In this case, the elongation, frequency, and energy of the mechanical bending oscillations are described by other expressions. Let's define these expressions and perform numerical estimates of their values.

4.2. Elongation, Frequency, and Energy of Mechanical Bending Oscillations According to Thickness a

The elongation (31.1), frequency (31.2) and energy of mechanical bending oscillations along the length a (31.3) can be obtained from (7), (8), (9), if we replace $a \to c$ and $c \to a$ in them. Finally, under the condition $a \sim b$, we obtain numerical estimates of the indicated quantities:

$$\varepsilon_a = \frac{\pi}{4}\frac{h_{ap}^2}{c^2}, \tag{31.1}$$

$$\omega_{ap} = \sqrt{\frac{Ea^2}{12\rho(1-\nu^2)}}\left[\left(\frac{\pi}{c}\right)^2 + \left(\frac{\pi}{b}\right)^2\right] \approx \sqrt{\frac{Ea^2}{12\rho(1-\nu^2)}}\left(\frac{\pi}{c}\right)^2 = \tag{31.2}$$

$$= \sqrt{\frac{2.15\cdot 10^{11}\cdot 4\cdot 10^{-2}}{12\cdot 7810\cdot (0.89)}}\left(\frac{\pi}{7\cdot 10^{-3}}\right)^2 = \sqrt{\frac{2.15\cdot 10^{6}\cdot 4}{12\cdot 7.810\cdot 0.89}}10^6\cdot 0.2 = 6.42\cdot 10^7,\ s^{-1}$$

$$\Omega_{ap} = \frac{\pi^4}{192}\frac{Ea^3h_{ap}^2}{(1-\nu^2)}\left(\left(\frac{1}{c}\right)^2 + \left(\frac{1}{a}\right)^2\right)^2 ca \approx \frac{\pi^4}{192}\frac{Ea^3h_{ap}^2}{(1-\nu^2)}\left(\frac{1}{c}\right)^4 ca = \frac{\pi^4}{192}\frac{Ea^4h_{ap}^2}{(1-\nu^2)}\left(\frac{1}{c}\right)^3 = \tag{31.3}$$

$$= \frac{\pi^4}{192}\frac{Ea^4}{(1-\nu^2)c}\frac{h_{ap}^2}{c^2} \approx \frac{\pi^4}{192}\frac{2.15\cdot 10^{11}\cdot 2^4\cdot 10^{-4}}{(0.89)\cdot 7\cdot 10^{-3}}\frac{h_{ap}^2}{c^2} \approx 2.8\cdot 10^{10}\frac{h_{ap}^2}{c^2} = 2.8\cdot 10^{10}\frac{4}{\pi}\varepsilon_a, \qquad J.$$

In (30.1), (30.3), (31.1), (31.3), unknown quantities are elongations $\varepsilon_{a,c}$. Their values can be estimated by comparing the initial kinetic energy of the FB $W_{fb} \approx 1.422\ kJ$ and the energy of mechanical bending oscillations across the thickness c or a:

From (32) it follows that the elongation of mechanical bending oscillations along the thickness c is greater than that along the length a. It is obvious that it is these vibrations that are responsible for the mechanical destruction of the AP, since for certain grades of steel, elongations of the order of several percent are destructive [10].

CONCLUSIONS

The conditions for realizing an ideal armor plate (AP) under impact by a flying body (FB) have been investigated. As an illustrative example, an AP with a mass of $M = 2.18$ kg subjected to the impact of a 7.62 mm projectile with a mass of $m = 7.9 \times 10^{-3}$ kg has been analyzed. Although this specific case is considered, the proposed approach can be extended to other types of projectiles and target materials. The study focuses on the transformation of the FB energy characteristics - momentum, kinetic energy, and power - during interaction with the AP. It is shown that only a small fraction of the FB momentum is transferred to the AP, while nearly all of the FB kinetic energy is converted into the internal energy of the plate. This internal energy consists of the energy of mechanical oscillations of the entire plate and the energy associated with material displacement within it. The AP is modeled as a rectangular parallelepiped with dimensions a, b(with $a \sim b$) and thickness c. The frequencies of natural bending oscillations perpendicular to and along the plate surface have been estimated. It is shown that oscillations along the surface with the largest area occur in the megahertz range, whereas oscillations perpendicular to the surface lie in the kilohertz range. The energy of bending oscillations along the surface exceeds that of perpendicular oscillations by a factor of a^2/c^2. Under the condition $a^2/c^2 \gg 1$, this may lead to significant tensile strains and potential cracking of the plate. The analysis demonstrates that the ratio $M/(M+m)$ determines the fraction of the FB kinetic energy converted into the internal energy of the AP, which approaches unity for $m \ll M$. The transfer of kinetic energy is assumed to occur in a cylindrical channel of base area S_0. It is shown that the maximum power transferred from the FB to the AP reaches $16/27 \approx 0.5926$ of the initial FB power and corresponds to a reduction of the FB velocity by a factor of three. For normal impact, the characteristic penetration length over which maximum power loss occurs is proportional to the FB length h. The multilayer AP configuration has also been analyzed. It is shown that in subsequent layers with lower material density, the conditions for maximum power loss remain similar to those in the first layer. The optimal thickness of each layer is determined by the distance over which the FB experiences maximum power loss. The results indicate that properly designed multilayer armor plates can significantly reduce overall dimensions and weight while maintaining high protective performance. It should be emphasized that the present analysis is qualitative and does not aim to directly quantify agreement with experimental data, as several secondary effects have not been taken into account. Nevertheless, the proposed approach provides a physical basis for understanding energy dissipation mechanisms and offers guidance for further optimization using numerical modeling and experimental validation.

ORCID

Mikola Odeychuk, https://orcid.org/0000-0002-6507-2588; **Ivan Tkachenko,** https://orcid.org/0009-0005-1378-2077;
Viktor Tkachenko, https://orcid.org/0000-0002-1108-5842

REFERENCES

[1] I. A. Balaganskii, and L. A. Merzhievskii, *The action of weapons and ammunition*, (Izd-vo NGTU, Novosibirsk, 2004). (in Russian)
[2] V. M. Fomin, A. I. Gulidov, G. A. Sapozhnikov, *et al*., *High-speed interaction of bodies*, (Izd-vo Sib. otd-niia Ros. akad. nauk, Novosibirsk, 1999). (in Russian)
[3] S. A. Manzhura, D.S. Baulin, S.A. Gorelishev, *et al*., *Multilayer armored structures to provide protection for personnel and military equipment*, (NA NGU, Kharkiv, 2023). (in Ukrainian)
[4] W. Lu, Y. Wu, M. Ma, Y. Yu, X. Zhou, and G. Gao, Theoretical and Applied Mechanics Letters, **14**(5), 100550 (2024). https://doi.org/10.1016/j.taml.2024.100550
[5] F. Min, K. Gao, W. Wei, X. Wu, S. Wen, H. Huang, Z. Nie, *et al*., Int. J. Impact Eng. **191**, 104998 (2024). https://doi.org/10.1016/j.ijimpeng.2024.104998
[6] Y. Wu, W. Lu, Y. Yu, M. Ma, X. Sun, and G. Gao, Solids, **60**, 2695 (2025). https://doi.org/10.1134/S0025654425601624
[7] L. D. Landau, and E. M. Lifshitz, *Theory of elasticity,* (Pergamon Press, Oxford, 1986).
[8] S. E. Aleksentseva, Dr.S. dissertation, Samara, 2015. (in Russian)
[9] A. Betts, UFN, **10**(2), 26 (1930). (in Russian)
[10] A. V. Darkov, and G. S. Shapiro, *Strength of materials*, (Vysshaia shkola, M., 1975). (in Russian)

ТЕОРІЯ ІДЕАЛЬНОЇ БРОНЕВОЇ ПЛИТИ. ЕНЕРГЕТИЧНІ ЗАКОНОМІРНОСТІ УДАРУ ВИСОКОШВИДКІСНОГО ТІЛА ПО БРОНЕВІЙ ПЛИТІ

М.П. Одейчук, І.В. Ткаченко, В.І. Ткаченко

Національний науковий центр «Харківський фізико-технічний інститут», вул. Академічна, 1, Харків, 61108, Україна

Це дослідження присвячено аналізу оптимальних енергетичних характеристик летючого тіла (ЛТ), що зіткнеться з броньовою пластиною (БП). Розглянуті енергетичні характеристики включають імпульс, кінетичну енергію та потужність обох тіл. Показано, що лише невелика частина імпульсу ЛТ передається БП, тоді як майже вся кінетична енергія ЛТ перетворюється на внутрішню енергію БП. Ця внутрішня енергія складається з енергії механічних коливань пластини та енергії, пов'язаної зі зміщенням матеріалу всередині неї. Оцінено енергію власних коливань ЛТ, змодельованого як прямокутний паралелепіпед з розмірами a, b де $a \sim b$ та товщиною c. Розраховано частоти згинальних коливань, перпендикулярних поверхні пластини та вздовж неї. Показано, що енергія згинальних коливань вздовж поверхні з найбільшою площею перевищує енергію згинальних коливань, перпендикулярних до поверхні, в a^2/c^2 разів. Вважається, що передача кінетичної енергії ЛТ відбувається в циліндричному каналі з площею основи S_0. Показано, що максимальна потужність, що передається від ЛТ до БП, дорівнює 16/27≈0,5926 від початкової потужності ЛТ та супроводжується зменшенням швидкості ЛТ утричі. Характерна довжина проникнення, що відповідає максимальним втратам потужності, пропорційна довжині ЛТ h. Також розглянуто багатошарову конфігурацію БП. Показано, що в наступних шарах з меншою щільністю матеріалу зберігаються умови для максимальних втрат потужності. Товщина кожного шару визначається відстанню, на якій відбуваються максимальні втрати потужності. Результати показують, що правильно спроєктовані багатошарові БП можуть значно зменшити габаритні розміри та вагу, зберігаючи при цьому високу захисну ефективність. Слід зазначити, що цей аналіз є якісним і не має на меті забезпечити кількісну відповідність експериментальним даним, оскільки деякі вторинні ефекти не враховуються. Результати забезпечують фізичну основу для розуміння механізмів дисипації енергії та пропонують напрямки подальшої оптимізації за допомогою числових методів.

Ключові слова: *броньова плита; літаюче тіло; удар; енергія; втрати потужності; багатошаровість*

East European Journal of Physics. 2. 610–621 (2026)
DOI: 10.26565/2312-4334-2026-2-68 ISSN 2312-4334

AXIALLY SYMMETRIC SHARMA MITTAL HOLOGRAPHIC DARK ENERGY IN THE BRANS-DICKE THEORY

Suresh Kadali, **Neelima Davuluri***
Department of Mathematics and Statistics, GITAM (Deemed to be University), Visakhapatnam-530045, India
*Corresponding Author e-mail: neeludavuluri@gmail.com
Received March 2, 2025; revised May 3, 2025; accepted May 24, 2026

This study investigates Sharma–Mittal Holographic Dark Energy (SMHDE) within the context of Brans–Dicke theory of gravitation in an Axially Symmetric Cosmological Model. By employing Sharma–Mittal entropy, which provides a unifying generalization of Tsallis and Rényi entropies, a modified form of holographic dark energy density is formulated to incorporate non-extensive thermodynamic effects. The corresponding field equations are derived and solved to obtain exact analytical solutions. Furthermore, key cosmological parameters such as the EoS parameter, deceleration parameter, and squared speed of sound are systematically analyzed to examine the dynamical behaviour and stability of the model. The results indicate that the proposed framework successfully describes the late-time accelerated expansion of the cosmos while also accommodating possible anisotropies in the early cosmos. Overall, the model presents a consistent and physically viable extension of conventional holographic dark energy scenarios within scalar–tensor gravitational theory.

Keywords: *Sharma–Mittal Entropy; Holographic Dark Energy; Brans–Dicke Theory; Axially Symmetric Metric*

PACS: 95.36.+x, 98.80.-k, 98.80.jk, 11.10.Kk

1. INTRODUCTION

The theory of cosmology and gravitation is one of the great achievements of modern theoretical physics. The discovery of SNe Ia gave us the first evidence of the accelerated expansion of the Universe [1-2]. This discovery was then corroborated by independent measurements made from the observation of the cosmic microwave background (CMB) radiation and the study of the large scale structure [3-4]. All these observations show that our current Universe is dominated by a negative pressure mysterious constituent named dark energy (DE) and this component is responsible for driving the Universe towards an accelerated expansion. Observations have shown that DE comprises 70-75% of the energy density of the current universe [5-6]. But, still, the origin of DE is not known.

Many DE models have been proposed by many researchers in order to understand the nature of DE. Among those models, one interesting model is the holographic dark energy (HDE) model. The idea of HDE arises from the idea of the holographic principle postulated by 't Hooft and Susskind [7-8], which says that the number of degrees of freedom in any physical system is proportional to its boundary area and not its volume.

The holographic dark energy (HDE) model is motivated by the holographic principle proposed by 't Hooft and Susskind [7–8], which states that the physical degrees of freedom of a system are determined by its boundary area rather than its volume. Based on this idea, Cohen et al. [9] established a relation between the ultraviolet (UV) and infrared (IR) cutoffs by requiring that the vacuum energy contained in a region of size L should not exceed the mass of a black hole of the same size. This condition leads to the holographic dark energy density

$$\rho_{de} = 3k^2 M_p^2 L^{-2}$$

where k is a dimensionless holographic parameter, $M_p = (8\pi G)^{-1/2}$ is the reduced Planck mass, G is Newton's gravitational constant, and L denotes the infrared cutoff length scale. Later, Li [10] proposed the future event horizon as the IR cutoff and obtained a cosmologically viable HDE model capable of describing the observed accelerated expansion of the universe.

The conventional HDE model is constructed using the Bekenstein–Hawking entropy-area relation,

$$S_{BH} = \frac{A}{4G}$$

where A is the horizon area.

Since gravitational systems are characterized by long-range interactions and non-extensive thermodynamic behavior, generalized entropy formalisms have been proposed to extend the standard entropy description. Among these, Tsallis entropy [11] and Rényi entropy [12] have attracted considerable attention in cosmological applications. A more general entropy framework was introduced by Sharma and Mittal [13], which unifies both Tsallis and Rényi entropies through two independent parameters.

Cite as: S. Kadali, N. Davuluri, East Eur. J. Phys. 2, 610 (2026), https://doi.org/10.26565/2312-4334-2026-2-68

The Sharma–Mittal entropy is defined as

$$S_{SM} = \frac{1}{s}[(1 + lS_T)^{\frac{s}{l}} - 1]$$

where S_T denotes the Tsallis entropy, while s and l represent the deformation and non-extensivity parameters, respectively.

To formulate Sharma–Mittal holographic dark energy (SMHDE), the standard Bekenstein–Hawking entropy used in the HDE framework is replaced by Sharma–Mittal entropy. Taking $S_T = S_{BH} = A/4$ (in natural units $G = 1$) and considering the Hubble horizon $L = H^{-1}$, whose area is $A = \frac{4\pi}{H^2}$, the Sharma–Mittal entropy becomes

$$S_{SM} = \frac{1}{s}\left[\left(1 + \frac{\pi l}{H^2}\right)^{\frac{s}{l}} - 1\right]$$

where H is the Hubble parameter.

Using the holographic relation between entropy and dark energy density, Jawad et al. [14] and Iqbal and Jawad [15] obtained the Sharma–Mittal holographic dark energy density as

$$\rho_{de} = \frac{3k^2 S_{SM}}{8\pi L^4} = \frac{3k^2 H^4}{8\pi s}\left[\left(1 + \frac{\pi l}{H^2}\right)^{\frac{s}{l}} - 1\right]$$

where H is the Hubble parameter.

In contrast to conventional HDE, the SMHDE theory takes into account the effects of the entropy due to non-extensive thermodynamics using the parameters s and l. These correction terms have substantial impacts on the dynamics of the universe, which can explain not only inflation but also acceleration at late times in the same theory [16-17]. Besides, some recent studies have demonstrated that SMHDE models can offer stable evolution and phantom crossing in cosmology.

At the same time, scalar-tensor theories of gravity offer a viable alternative explanation of cosmic acceleration. One of the most successful generalizations of general relativity is the Brans-Dicke (BD) theory [18], proposed by Brans and Dicke in 1961. The BD scalar field inherently satisfies Mach's principle and acts as an important ingredient in explaining cosmological processes [19–20]. Some of the authors have studied the possibility of applying HDE and generalized entropy-based dark energy models within the framework of BD gravity, highlighting their peculiarities and stability properties [21-23].

On the other hand, observations of the anisotropies in the cosmic microwave background (CMB) and the formation of large-scale cosmic structures suggest that the early Universe may not have been perfectly isotropic. Therefore, anisotropic cosmological models, such as Bianchi-type models and axially symmetric models, play an important role in understanding the dynamical evolution of the Universe [24-25]. Axially symmetric universes provide a more general geometric framework than the standard Friedmann–Robertson–Walker (FRW) model and help to describe deviations from perfect isotropy in the early stages of cosmic evolution.

These developments motivate the present study, in which we investigate the Sharma–Mittal holographic dark energy model in an axially symmetric framework within the Brans–Dicke theory of gravity. The generalized Sharma–Mittal entropy is incorporated into the holographic energy density, and an anisotropic geometry is considered to examine the combined effects of entropic deformation, scalar–tensor coupling, and directional anisotropy on the evolution of the Universe. The corresponding field equations are derived, and important cosmological parameters, such as the equation of state parameter, the deceleration parameter, and the squared speed of sound, are analyzed to study the dynamical behavior and stability of the model.

The present work aims to provide a deeper understanding of the role of generalized entropy corrections in scalar–tensor theories and their implications for the evolution of the Universe.

2. METRIC AND FIELD EQUATIONS

The Axially Symmetric cosmological model can be defined as

$$ds^2 = dt^2 - A^2\left[dx^2 + f^2 d\Phi^2\right] - B^2 dz^2 \tag{1}$$

where A and B are functions of time t only and f is function of x .
Brans-Dicke field equations are given by

$$R_{ij} - \frac{1}{2}R\, g_{ij} = \frac{-8\pi}{\phi}T_{ij} - \omega\phi^{-2}\left(\phi_{,i}\phi_{,j} - \frac{1}{2}g_{ij}\phi_{,k}\phi^{,k}\right) - \frac{1}{\phi}\left(\phi_{i:j} - g_{ij}\phi_{,k}{}^{,k}\right) \tag{2}$$

and

$$\Box\phi = \frac{8\pi}{3 + 2\omega}T \tag{3}$$

Here ω is constant, $G_{ij} = R_{ij} - \frac{1}{2}R\,g_{ij}$ is the Einstein tensor, R_{ij} is Ricci curvature tensor, R is Ricci scalar and T_{ij} is the matter's energy momentum tensor,ϕ is the Brans-Dicke's scalar field, g_{ij} is the space time's metric tensor.
It's energy conservation equation is

$$T_{;j}^{\ ij} = 0 \tag{4}$$

The equation of the energy momentum tensors for matter and dark energy as follows

$$T_{ij} = T_{ij}^{m} + T_{ij}^{\wedge} \tag{5}$$

where T_{ij}^{m} and $T_{ij}^{\wedge}$ are represents the energy momentum tensor for DM and DE respectively and defined as

$$T_{ij}^{m} = (\rho_{de} + p_{de})\,u_i u_j - p_{de} g_{ij} \qquad \text{and} \qquad T_{ij}^{\Lambda} = \rho_m u_i u_j \tag{6}$$

Then the corresponding energy momentum tensor is given by

$$T_{ij} = diag\ \ (\rho_{de} + \rho_{de}, -p_{de}, -p_{de}, -p_{de}) \tag{7}$$

where ρ_m and ρ_{de} are the energy densities of DM and the DE respectively and p_{de} is the DE's pressure.
The field equations (2) and (3) for the metric in Eq. (1) can now be expressed using Eq. (7).

$$-\frac{8\pi}{\phi}p_{de} = \frac{\ddot{A}}{A} + \frac{\ddot{B}}{B} + \frac{\dot{A}\dot{B}}{AB} + \frac{\omega}{2}\frac{\dot{\phi}^2}{\phi^2} + \frac{\dot{\phi}}{\phi}\left(\frac{\dot{A}}{A} + \frac{\dot{B}}{B}\right) + \frac{\ddot{\phi}}{\phi} \tag{8}$$

$$-\frac{8\pi}{\phi}p_{de} = \frac{\ddot{A}}{A} + \frac{\ddot{B}}{B} + \frac{\dot{A}\dot{B}}{AB} - \frac{f''}{A^2 f} + \frac{\omega}{2}\frac{\dot{\phi}^2}{\phi^2} + \frac{\dot{\phi}}{\phi}\left(\frac{\dot{A}}{A} + \frac{\dot{B}}{B}\right) + \frac{\ddot{\phi}}{\phi} \tag{9}$$

$$-\frac{8\pi}{\phi}p_{de} = 2\frac{\ddot{A}}{A} + \frac{\dot{A}^2}{A^2} - \frac{f''}{A^2 f} + \frac{\omega}{2}\frac{\dot{\phi}^2}{\phi^2} + 2\frac{\dot{A}}{A}\frac{\dot{\phi}}{\phi} + \frac{\ddot{\phi}}{\phi} \tag{10}$$

$$\frac{8\pi}{\phi}(\rho_{de} + p_{de}) = \frac{\dot{A}^2}{A^2} + \frac{2\dot{A}\dot{B}}{AB} - \frac{\omega}{2}\frac{\dot{\phi}^2}{\phi^2} + \left(2\frac{\dot{A}}{A} + \frac{\dot{B}}{B}\right)\frac{\dot{\phi}}{\phi} \tag{11}$$

And the energy conservation equation is

$$\dot{\rho_m} + \dot{\rho_{de}} + (\rho_m + \rho_{de} + P_{de})\left(\frac{2\dot{A}}{A} + \frac{\dot{B}}{B}\right) = 0 \tag{12}$$

In this case, ordinary differentiation w.r.t t is represented by the notation dot $(\cdot)$ and differentiation w.r.t x is represented by notation dash $(')$.
From Eqs. (8)-(11), it is observed that the terms containing $f(x)$ depend only on the spatial coordinate (x), whereas the remaining terms are functions of cosmic time (t). Since both sides are functions of independent variables, they must be equal to a constant. Therefore, we set

$$\frac{f''}{f} = \alpha^2 \tag{13}$$

where α^2 is an arbitrary separation constant.

For the particular case $\alpha = 0$, (13) reduces to $f'' = 0$, whose solution is

$$f(x) = \alpha_1 x + \alpha_2$$

where α_1 and α_2 are constants of integration.

Consequently, the field equations can be rewritten as

$$-\frac{8\pi}{\phi}p_{de} = \frac{\ddot{A}}{A} + \frac{\ddot{B}}{B} + \frac{\dot{A}\dot{B}}{AB} + \frac{\omega}{2}\frac{\dot{\phi}^2}{\phi^2} + \frac{\dot{\phi}}{\phi}\left(\frac{\dot{A}}{A} + \frac{\dot{B}}{B}\right) + \frac{\ddot{\phi}}{\phi} \tag{14}$$

$$-\frac{8\pi}{\phi}p_{de} = \frac{\ddot{A}}{A} + \frac{\ddot{B}}{B} + \frac{\dot{A}\dot{B}}{AB} + \frac{\omega}{2}\frac{\dot{\phi}^2}{\phi^2} + \frac{\dot{\phi}}{\phi}\left(\frac{\dot{A}}{A} + \frac{\dot{B}}{B}\right) + \frac{\ddot{\phi}}{\phi} \tag{15}$$

$$-\frac{8\pi}{\phi}p_{de} = 2\frac{\ddot{A}}{A} + \frac{\dot{A}^2}{A^2} + \frac{\omega}{2}\frac{\dot{\phi}^2}{\phi^2} + 2\frac{\dot{A}}{A}\frac{\dot{\phi}}{\phi} + \frac{\ddot{\phi}}{\phi} \tag{16}$$

$$\frac{8\pi}{\phi}(\rho_{de} + p_{de}) = \frac{\dot{A}^2}{A^2} + \frac{2\dot{A}\dot{B}}{AB} - \frac{\omega}{2}\frac{\dot{\phi}^2}{\phi^2} + \left(2\frac{\dot{A}}{A} + \frac{\dot{B}}{B}\right)\frac{\dot{\phi}}{\phi} \tag{17}$$

3. SOLUTIONS OF THE FIELD EQUATIONS

Equations (14)-(17) form a system of four different equations with seven unknown variables; $\rho_m, \rho_{de}, p_{de}, \omega_{de}, A, B$ and ϕ. Hence to solve the system of equations we assume
(i)Firstly the relationship between the metric potentials A and B as

$$B = A^{k_1} \tag{18}$$

Here k_1 is a constant.
Following the works of R. C. Johri and R. Sudharsan [26], R. C. Johri and K. Desikan [27], and Diksha Trivedi [28],
(ii)Secondly, we assume a power-law relationship between the Brans–Dicke scalar field ϕ and the average scale factor $a(t)$, given by

$$\phi \propto [a(t)]^{k_2},$$

where k_2 is a constant power-law index.

Such a relation has been extensively employed in the literature to investigate various cosmological aspects of scalar–tensor theories. Motivated by its physical significance and to simplify the highly nonlinear field equations, we adopt the following form:

$$\phi = \phi_0 [a(t)]^{k_2} \tag{19}$$

where ϕ_0 and k_2 are arbitrary constants. This assumption reduces the mathematical complexity of the system and facilitates the derivation of exact cosmological solutions.

The effective or average scale factor is

$$a = (A^2 B)^{1/3} \tag{20}$$

The Volume scale factor V can be written as

$$V = a^3 = \sqrt{-g} = A^2 B \tag{21}$$

Using equations (18),(19) and(20),we get

$$A(t) = [k_5 (k_3 t + k_4)]^{1/k_5}, \text{where } k_5 = \frac{(k_1+2)(k_2+3)}{3} \tag{22}$$

where k_3 and k_4 are the integration constants.
From (18) and (22), we have

$$B(t) = [k_5 (k_3 t + k_4)]^{k_1/k_5} \tag{23}$$

Therefore, the corresponding metric can be expressed as

$$ds^2 = dt^2 - [k_5 (k_3 t + k_4)]^{2/k_5} \left[dx^2 + f^2 d\Phi^2\right] - [k_5 (k_3 t + k_4)]^{2k_1/k_5} dz^2 \tag{24}$$

We ascertain the cosmos's scale factor utilising equations (20), (22), and (23) as follows:

$$a(t) = [k_5 (k_3 t + k_4)]^{\frac{2+k_1}{3k_5}} \tag{25}$$

Therefore, from equations (19) and (25), we derive the scalar field as

$$\phi = \phi_0 [k_5 (k_3 t + k_4)]^{\frac{k_2}{k_2+3}} \tag{26}$$

We determine the Hubble's parameter from equation (25) as

$$H = \frac{\dot{a}}{a} = \frac{k_3(2+k_1)}{3k_5(k_3 t + k_4)} \tag{27}$$

The Deceleration parameter equation is as follows $q = \frac{-\ddot{a}(t)}{a(t)H^2}$
Equations (25) and (27) can be used to calculate the deceleration parameter.

$$q = \frac{3k_5}{2+k_1} - 1 \tag{28}$$

The Anisotropic parameter is described as

$$A_h = \frac{1}{3}\sum_{i=1}^{3}\left(\frac{H_i - H}{H}\right)^2 = \frac{6\left(k_1^2 + 2k_1 + 3\right)}{(k_1+2)^2} \tag{29}$$

The Expansion scalar is defined as $H = \frac{\theta}{3}$ so $\theta = 3H$
Equation (27) can be used to calculate the Expansion scalar as

$$\theta = \frac{k_3(2+k_1)}{k_5(k_3t+k_4)} \tag{30}$$

The redshift z is defined as $z = \frac{a_0}{a} - 1$
Using equation (25), and by considering $a_0 = 1$
Redshift for our model is given by

$$z = \frac{1 - [k_5\,(k_3t+k_4)]^{\frac{2+k_1}{3k_5}}}{[k_5\,(k_3t+k_4)]^{\frac{2+k_1}{3k_5}}} \tag{31}$$

,
Energy Density of Sharma-Mittal Holographic Dark Energy is defined as

$$\rho_{de} = \frac{3k^2H^4}{8\pi s}\left[\left(1+\frac{\pi l}{H^2}\right)^{\frac{s}{l}} - 1\right]$$

where k is a dimensionless constant, s and l are Sharma–Mittal entropy parameters corresponding to deformation and non-extensivity and H is Hubble's parameter.The parameter l measures the deviation from standard extensive thermodynamics, whereas s controls the deformation effect of the generalized entropy structure. An important feature of Sharma–Mittal entropy is that it reduces to Tsallis entropy in the limit $s \to l$, and to Rényi entropy in the limit $s \to 0$. Hence, Sharma–Mittal entropy provides a more general and physically consistent framework for describing gravitational systems with long-range interactions and non-additive thermodynamical behavior.
By substituting H value in the above equation from (27), we get energy density as

$$\rho_{de} = \frac{3k^2}{8\pi s}\left[\frac{k_3\,(2+k_1)}{3k_5}\right]^4\left[\frac{1}{(k_3t+k_4)^4}\right]\left[\left[1+\frac{9k_5^2(k_3t+k_4)^2l\pi}{k_3^2(2+k_1)^2}\right]^{\frac{s}{l}} - 1\right] \tag{32}$$

For plotting the graphical behavior of the cosmological parameters, we have considered the values $k = 0.7$, $k_1 = 2.01$, $k_2 = 1.01$, $k_3 = 0.45$, $k_4 = 3.5$, $s = 4.5$, $l = 6$, $a_0 = 1$, $k_6 = 1.2$ and $\omega = 50$. These chosen values satisfy the physical viability of the model and help in obtaining well-behaved graphical evolution of the cosmological quantities.

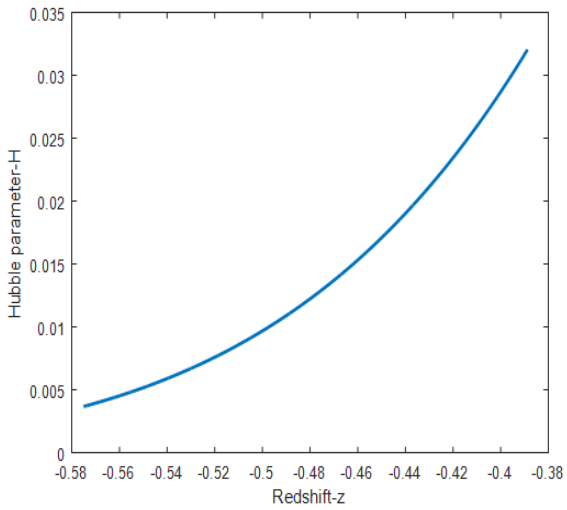

Figure 1. The Hubble parameter against redshift

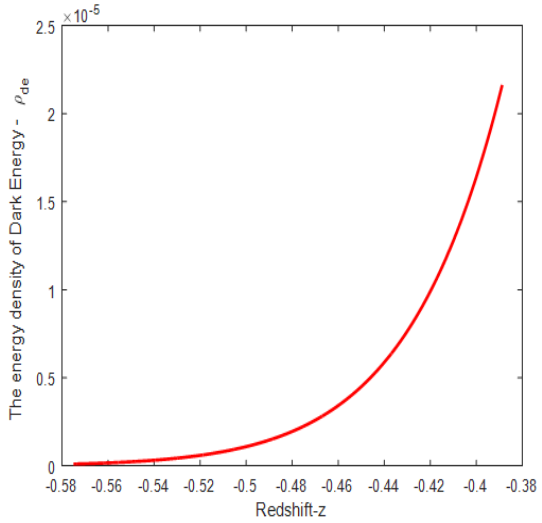

Figure 2. The DE's energy density against redshift

The equation that we will use to acquire the EoS parameter is as follows.

$$\omega_{de} = -1 - \frac{\rho'_{de}}{3H\rho_{de}}$$

Equations (27) and (32) can be used to calculate the EoS parameter of the model as

$$\omega_{de} = -1 + \frac{4k_5}{k_1+2} - \frac{\frac{18s\pi k_5^3[k_3t+k_4)^2}{k_3^2(2+k_1)^3}\left[1+\frac{9k_5^2(k_3t+k_4)^2l\pi}{k_3^2(2+k_1)^2}\right]^{\frac{s}{l}-1}}{\left[1+\frac{9k_5^2(k_3t+k_4)^2l\pi}{k_3^2(2+k_1)^2}\right]^{\frac{s}{l}}-1} \tag{33}$$

We can determine the matter's energy density using equations (12) and (32). Then

$$\rho_m = \frac{3k^2}{8\pi s}\left[\frac{k_3\,(2+k_1)}{3k_5}\right]^4\left[\frac{1}{(k_3t+k_4)^4}\right]\left[\left[1+\frac{9k_5^2(k_3t+k_4)^2l\pi}{k_3^2(2+k_1)^2}\right]^{\frac{s}{l}}-1\right]$$

$$+\frac{k_3^2\phi_0}{8\phi}[k_5\,(k_3t+k_4)]^{\frac{k_2}{k_2+3}-2}\left\{\begin{array}{c} 1+2k_1+(2+k_1)\,k_2k_5 \\ -\frac{k_2^2k_5^2}{2(k_2+3)^2}\left(-1+\frac{4k_5}{k_1+2}-\frac{\frac{18s\pi k_5^3[k_3t+k_4)^2}{k_3^2(2+k_1)^3}\left[1+\frac{9k_5^2(k_3t+k_4)^2l\pi}{k_3^2(2+k_1)^2}\right]^{\frac{s}{l}-1}}{\left[1+\frac{9k_5^2(k_3t+k_4)^2l\pi}{k_3^2(2+k_1)^2}\right]^{\frac{s}{l}}-1}\right) \end{array}\right\} \tag{34}$$

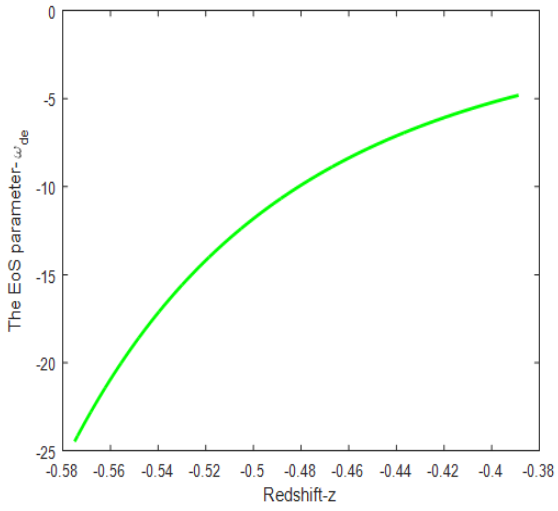

Figure 3. The EoS parameter against redshift

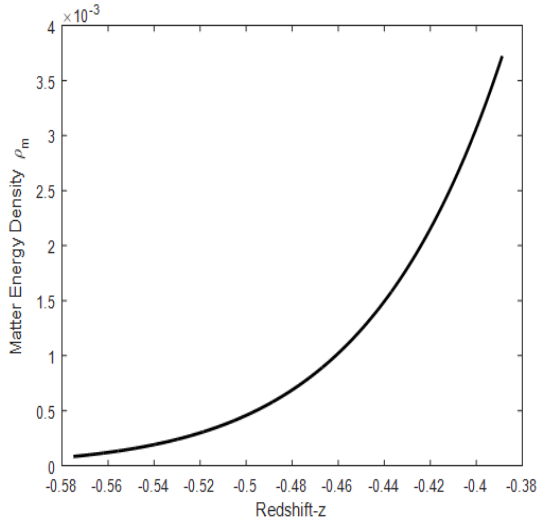

Figure 4. The energy density of matter against redshift

Hence from equations (27) and (33), we find the pressure of DE as

$$p_{de} = -\frac{\phi_0k_3^2[k_5\,(k_3t+k_4)]^{\frac{k_2}{k_2+3}-2}}{16\pi(k_2+3)^2}\left\{k_6+k_2^2k_5^2\left[-1+\frac{4k_5}{k_1+2}-\frac{\frac{18s\pi k_5^3[k_3t+k_4)^2}{k_3^2(2+k_1)^3}\left[1+\frac{9k_5^2(k_3t+k_4)^2l\pi}{k_3^2(2+k_1)^2}\right]^{\frac{s}{l}-1}}{\left[1+\frac{9k_5^2(k_3t+k_4)^2l\pi}{k_3^2(2+k_1)^2}\right]^{\frac{s}{l}}-1}\right]\right\} \tag{35}$$

The jerk parameter is represented by the following formula

$$j = \frac{\dddot{a}}{aH^3}$$

Now, with the use of Equations (25) and (27), we are able to calculate the Jerk Parameter as

$$j = \frac{3\,(k_2+2)\,(2k_2+5)}{k_3\,(k_1+2)} \tag{36}$$

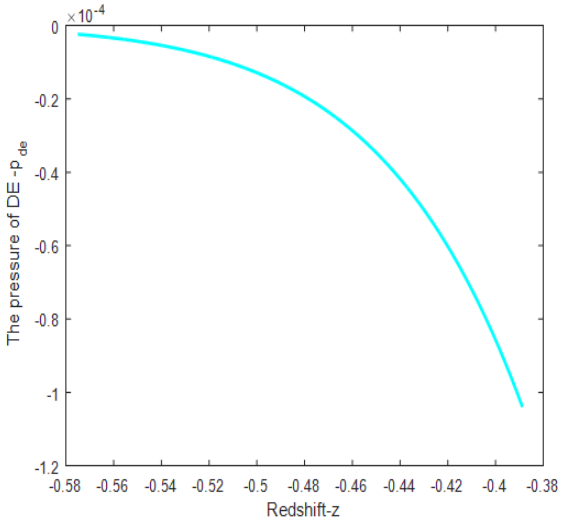

Figure 5. The pressure of DE against redshift

Statefinder Parameters:
The Hubble and deceleration parameters describe the universe's expansion, but because many dark energy models show similar behavior with these, we can't use them to tell the models apart. To fix this, Sahni et.al [30] came up with the statefinder parameters. These act as special cosmological tools to help us better differentiate and understand various dark energy models.These are defined as $r = \frac{\ddot{a}}{aH^3}$ and $s = \frac{r-1}{3(q-\frac{1}{2})}$.
Now, with the use of Equations (25) and (27), we get r as

$$r = \frac{3\,(k_2+2)\,(2k_2+5)}{k_3\,(k_1+2)} \tag{37}$$

and

$$s = \frac{2}{3k_3}\left[\frac{(k_1+2)\,(2k_2+5) - k_3\,(k_1+2)}{k_5 - (2+k_1)}\right] \tag{38}$$

Squared speed of sound: The squared speed of sound, denoted by the symbol v_s^2, is a variable whose sign is used to assess the stability of DE models.The DE model with $v_s^2 > 0$ is considered stable, while the DE model $v_s^2 < 0$ is considered unstable.
From the definition of the sound's squared speed, we have

$$v_s^2 = \frac{\dot{p_{de}}}{\dot{\rho_{de}}}$$

$$v_s^2 = \frac{-\frac{\phi_0 k_3^2 [k_5(k_3t+k_4)]^{\frac{k_2}{k_2+3}-2}}{16\pi(k_2+3)^2}\left\{\begin{array}{l}\frac{-k_3(k_2+6)}{(k_3t+k_4)(k_2+3)}\left[k_6 + k_2^2k_5^2\left[-1+\frac{4k_5}{k_1+2} - \frac{\frac{18s\pi k_5^3[k_3t+k_4)^2}{k_3^2(2+k_1)^3}\left[1+\frac{9k_5^2(k_3t+k_4)^2l\pi}{k_3^2(2+k_1)^2}\right]^{\frac{s}{l}-1}}{\left[1+\frac{9k_5^2(k_3t+k_4)^2l\pi}{k_3^2(2+k_1)^2}\right]^{\frac{s}{l}}-1}\right]\right] \\ +k_2^2k_5^2\left[\begin{array}{l}\frac{\frac{36s\pi k_5^3(k_3t+k_4)^3}{k_3^3(2+k_1)^5}\left[1+\frac{9k_5^2(k_3t+k_4)^2l\pi}{k_3^2(2+k_1)^2}\right]^{\frac{s}{l}-1}}{\left[\left[1+\frac{9k_5^2(k_3t+k_4)^2l\pi}{k_3^2(2+k_1)^2}\right]^{\frac{s}{l}}-1\right]^2} \\ \left\{\begin{array}{c}\frac{k_3^2(2+k_1)^2}{(k_3t+k_4)^2}+9l\pi\left(\frac{s}{l}-1\right)\left[1+\frac{9k_5^2(k_3t+k_4)^2l\pi}{k_3^2(2+k_1)^2}\right]^{-1} \\ -9k_5^2s\pi\left[1+\frac{9k_5^2(k_3t+k_4)^2l\pi}{k_3^2(2+k_1)^2}\right]^{\frac{s}{l}-1}\end{array}\right\}\end{array}\right]\end{array}\right\}}{\frac{3k^2}{8\pi s}\left(\frac{k_3(2+k_1)}{3k_5}\right)^4\left[\begin{array}{l}-4k_3(k_3t+k_4)^{-5}\left(\left\{1+\frac{9k_5^2(k_3t+k_4)^2l\pi}{k_3^2(2+k_1)^2}\right\}^{\frac{s}{l}}-1\right)+ \\ (k_3t+k_4)^{-4}\frac{s}{l}\left\{1+\frac{9k_5^2(k_3t+k_4)^2l\pi}{k_3^2(2+k_1)^2}\right\}^{\frac{s}{l}-1}\frac{18k_5^2(k_3t+k_4)l\pi}{k_3(2+k_1)^2}\end{array}\right]} \tag{39}$$

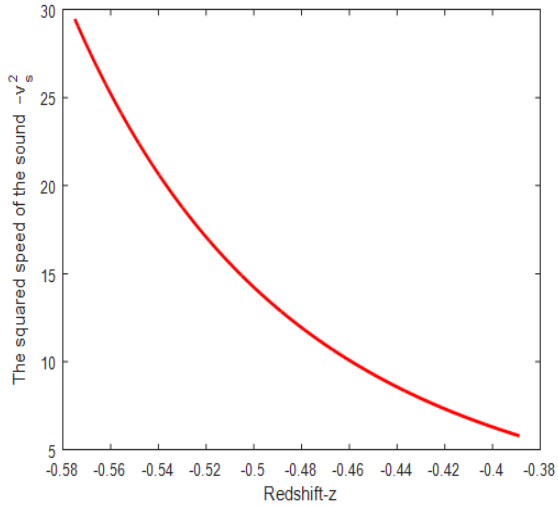

Figure 6. The Squared speed of sound versus redshift

The total density parameter defined as

$$\Omega = \Omega_m + \Omega_{de} \text{ here } \Omega_m = \frac{\rho_m}{3H^2} \text{ and } \Omega_{de} = \frac{\rho_{de}}{3H^2} \tag{40}$$

From equations (27) and (32) we have

$$\Omega_{de} = \frac{k^2}{8\pi s}\left[\frac{k_3\,(2+k_1)}{3k_5}\right]^2\left[\frac{1}{(k_3t+k_4)^2}\right]\left[\left[1+\frac{9k_5^2(k_3t+k_4)^2 l\pi}{k_3^2(2+k_1)^2}\right]^{\frac{s}{l}}-1\right] \tag{41}$$

From equations (27) and (34) we have

$$\begin{aligned}\Omega_m = {} & \frac{k^2}{8\pi s}\left[\frac{k_3\,(2+k_1)}{3k_5}\right]^2\left[\frac{1}{(k_3t+k_4)^2}\right]\left[\left[1+\frac{9k_5^2(k_3t+k_4)^2 l\pi}{k_3^2(2+k_1)^2}\right]^{\frac{s}{l}}-1\right] \\ & + \frac{k_3^2\phi_0}{8\phi}\left[k_5\,(k_3t+k_4)\right]^{\frac{k_2}{k_2+3}-2}\left\{\begin{array}{c} 1+2k_1+(2+k_1)\,k_2k_5 \\ -\frac{k_2^2k_5^2}{2(k_2+3)^2}\left(-1+\frac{4k_5}{k_1+2}-\frac{\frac{18s\pi k_5^3[k_3t+k_4)^2}{k_3^2(2+k_1)^3}\left[1+\frac{9k_5^2(k_3t+k_4)^2l\pi}{k_3^2(2+k_1)^2}\right]^{\frac{s}{l}-1}}{\left[1+\frac{9k_5^2(k_3t+k_4)^2l\pi}{k_3^2(2+k_1)^2}\right]^{\frac{s}{l}}-1}\right)\end{array}\right\}\end{aligned} \tag{42}$$

From equations (40),(41) and (42) we have

$$\begin{aligned}\Omega = {} & \frac{2k^2}{8\pi s}\left[\frac{k_3\,(2+k_1)}{3k_5}\right]^2\left[\frac{1}{(k_3t+k_4)^2}\right]\left[\left[1+\frac{9k_5^2(k_3t+k_4)^2 l\pi}{k_3^2(2+k_1)^2}\right]^{\frac{s}{l}}-1\right] \\ & + \frac{k_3^2\phi_0}{8\phi}\left[k_5\,(k_3t+k_4)\right]^{\frac{k_2}{k_2+3}-2}\left\{\begin{array}{c} 1+2k_1+(2+k_1)\,k_2k_5 \\ -\frac{k_2^2k_5^2}{2(k_2+3)^2}\left(-1+\frac{4k_5}{k_1+2}-\frac{\frac{18s\pi k_5^3[k_3t+k_4)^2}{k_3^2(2+k_1)^3}\left[1+\frac{9k_5^2(k_3t+k_4)^2l\pi}{k_3^2(2+k_1)^2}\right]^{\frac{s}{l}-1}}{\left[1+\frac{9k_5^2(k_3t+k_4)^2l\pi}{k_3^2(2+k_1)^2}\right]^{\frac{s}{l}}-1}\right)\end{array}\right\}\end{aligned} \tag{43}$$

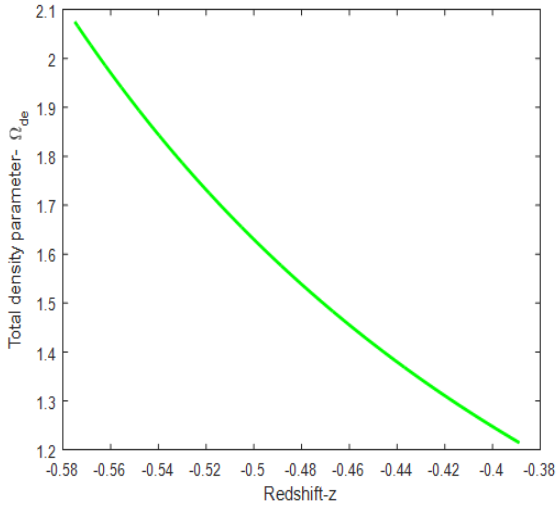

Figure 7. The total density parameter against redshift

The coincidence parameter is defined as

$$\bar{r} = \frac{\rho_{de}}{\rho_m} \tag{44}$$

From equations (32),(34) and (44) we have

$$\bar{r} = \frac{\frac{3k^2}{8\pi s}\left[\frac{k_3(2+k_1)}{3k_5}\right]^4\left[\frac{1}{(k_3t+k_4)^4}\right]\left[\left[1+\frac{9k_5^2(k_3t+k_4)^2l\pi}{k_3^2(2+k_1)^2}\right]^{\frac{s}{l}}-1\right]}{\frac{3k^2}{8\pi s}\left[\frac{k_3(2+k_1)}{3k_5}\right]^4\left[\frac{1}{(k_3t+k_4)^4}\right]\left[\left[1+\frac{9k_5^2(k_3t+k_4)^2l\pi}{k_3^2(2+k_1)^2}\right]^{\frac{s}{l}}-1\right]} + \frac{k_3^2\phi_0}{8\phi}\left[k_5\left(k_3t+k_4\right)\right]^{\frac{k_2}{k_2+3}-2}\left\{\left(-1+\frac{4k_5}{k_1+2}-\frac{\frac{18s\pi k_5^3[k_3t+k_4)^2}{k_3^2(2+k_1)^3}\left[1+\frac{9k_5^2(k_3t+k_4)^2l\pi}{k_3^2(2+k_1)^2}\right]^{\frac{s}{l}-1}}{\left[1+\frac{9k_5^2(k_3t+k_4)^2l\pi}{k_3^2(2+k_1)^2}\right]^{\frac{s}{l}}-1}\right)\right\}\left\{1+2k_1+(2+k_1)\,k_2k_5-\frac{k_2^2k_5^2}{2(k_2+3)^2}\right\} \tag{45}$$

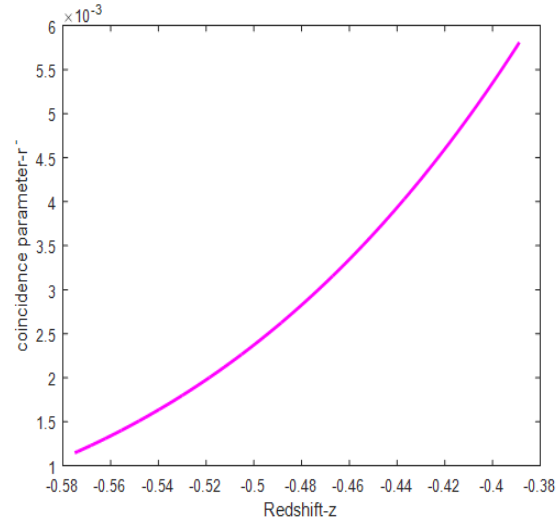

Figure 8. The coincidence parameter against redshift

The $\omega_{de} - \omega'_{de}$ plane: The plane $\omega_{de} - \omega'_{de}$ examination is used to assess the dynamic feature of the DE models evaluated by Steinhardt and Wang [29] where ω'_{de}denotes the derivative in relation to ln a. This approach has utilized the

fundamental model, leading to the creation of two plane models. The interior of the region$(\omega_{de}<0, \omega'_{de}>0)$ is the thawed area, while the area $(\omega_{de}<0, \omega'_{de}<0)$beneath it is frozen.
The expression for $\omega'_{de}$the derivative of equation (33) w.r.t ln a is obtained as

$$\omega'_{de} = \frac{\frac{36s\pi k_5^3(k_3t+k_4)^3}{k_3^3(2+k_1)^5}\left[1+\frac{9k_5^2(k_3t+k_4)^2l\pi}{k_3^2(2+k_1)^2}\right]^{\frac{s}{l}-1}}{\left[\left[1+\frac{9k_5^2(k_3t+k_4)^2l\pi}{k_3^2(2+k_1)^2}\right]^{\frac{s}{l}}-1\right]^2}\left\{\begin{array}{c}\frac{k_3^2(2+k_1)^2}{(k_3t+k_4)^2}+9l\pi\left(\frac{s}{l}-1\right)\left[1+\frac{9k_5^2(k_3t+k_4)^2l\pi}{k_3^2(2+k_1)^2}\right]^{-1} \\ -9k_5^2s\pi\left[1+\frac{9k_5^2(k_3t+k_4)^2l\pi}{k_3^2(2+k_1)^2}\right]^{\frac{s}{l}-1}\end{array}\right\} \tag{46}$$

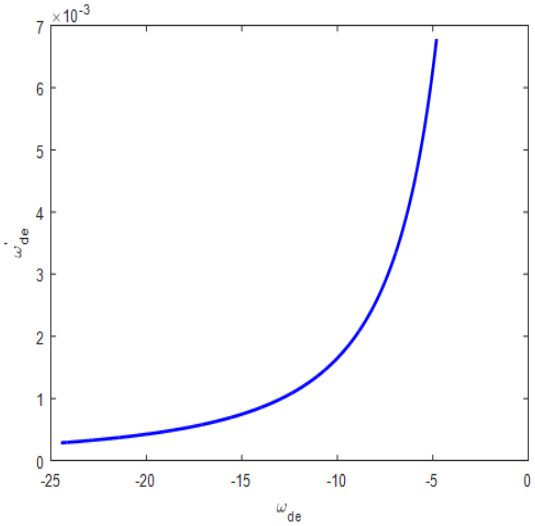

Figure 9. The $\omega_{de} - \omega'_{de}$ plane

4. CONCLUSIONS

In this study, we have investigated an Axially Symmetric Cosmological model within the context of Brans–Dicke theory, incorporating the SMHDE. The modified field equations were derived and analysed to examine the dynamical behaviour of the universe under the combined effects of anisotropy, scalar–tensor coupling, and generalized entropy. Our results demonstrate that the inclusion of Sharma–Mittal entropy significantly alters the evolution of holographic dark energy density, leading to notable modifications in key cosmological parameters. The model successfully describes late-time cosmic acceleration and highlights the crucial role of entropy generalization in shaping the expansion dynamics.

We have taken $k = 0.7$, $k_1 = 2.01$, $k_2 = 1.01$, $k_3 = 0.45$, $k_4 = 3.5$, $s = 4.5$, $l = 6$, $a_0 = 1$, $k_6 = 1.2$ and $\omega = 50$ values to plot the graphs.

- Figure 1 illustrates the relationship between redshift (z) and the Hubble parameter (H). From figure we observe that the Hubble parameter remains positive and decreases. However, the overall trend suggests that the cosmic expansion slows down over time, likely due to gravitational effects or other attractive forces. If this behaviour continues indefinitely, it may indicate a universe that could eventually stop expanding or transition into a slower, steady state of expansion.

- Figure 2 illustrates the relationship between the DE's energy density and redshift (z). The graph shows that the energy density remains positive and decreases. The positive value of the DE's energy density indicates its significant contribution to the total energy content of the cosmos. Moreover, as the redshift increases, the energy density gradually diminishes, suggesting that the cosmos is expanding and that the DE's density decreases progressively over cosmic time.

- Figure 3 illustrates the relationship between the EoS parameter (ω_{de}) and redshift (z). The graph shows that ω_{de} remains negative throughout its evolution and satisfies $\omega_{de} < -1$, indicating a phantom energy regime. Additionally, the EoS parameter decreases as redshift evolves. Since $\omega_{de} < -1$, the cosmos is undergoing accelerated expansion driven by phantom energy dominance. Although the acceleration persists, its magnitude may gradually decrease over cosmic time, depending on the dynamical behavior of the model.

- Figure 4 illustrates the relationship between the DM's energy density (ρ_m) and redshift (z). The graph shows that the dark matter energy density remains positive throughout its evolution and decreases. This behavior is consistent with an expanding universe

- Figure 5, the graph depicts the relationship between the pressure ($\bar{p}_{de}$) of DE and redshift (z). The graph shows that the pressure remains negative throughout its evolution and increases. This negative pressure of SMHDE indicates the presence of a repulsive component responsible for driving cosmic acceleration. As the pressure becomes more negative, the repulsive effect strengthens, thereby enhancing the accelerated expansion of the cosmos. This behavior is consistent with dark energy models that predict an increasing dominance of negative pressure in the cosmic dynamics.

- Figure 6 illustrates the relationship between the squared speed of sound (v_s^2) and redshift (z). The graph shows that v_s^2 remains positive throughout its evolution. The positivity of the squared speed of sound indicates that the model is free from classical instabilities under small perturbations. Therefore, this behavior suggests that the proposed cosmological model is stable over the considered redshift range.

- Figure 7 illustrates the relationship between the total density parameter against redshift.The graph shows that the total density parameter remains positive throughout its evolution and increases.The total density parameter change with redshift is depicted on the graph. Throughout, the overall density value stays positive, suggesting a cosmos with physical significance. Its upward trend indicates that, in comparison to the critical density, the total energy density increases. This demonstrates how the cosmos is entering a period of faster expansion driven by DE.

- Figure 8 illustrates the relationship between the coincidence parameter against redshift.The graph shows that the coincidence parameter remains positive throughout its evolution and decreases**.** Its decreasing behavior with time suggests that the universe evolves from an earlier matter-dominated phase to a late-time dark energy-dominated phase.

- Figure 9, the progression of our model is shown on the $\omega_{de} - \omega'_{de}$ plane. We observe that, depending on the graph values, $\omega_{de} - \omega'_{de}$ the plane trajectories change $\left(\omega_{de}<0, \omega'_{de}>0\right)$ in the thawed region.

Declarations:
Funding: No funds, grants, or other support was received.
Conflicts of interest: The authors have no conflicts of interest to declare that are relevant to the content of this article.
Availability of data and material: The data supporting the findings of this investigation are accessible from the corresponding author upon reasonable request.

Acknowledgements
we are thankful to the respected reviewer for his helpful comments, which have substantially improved the caliber of study and the presentation of our work.

ORCID

Suresh Kadali, https://orcid.org/0009-0004-9221-4483; **Neelima Davuluri**, https://orcid.org/0000-0003-1625-5596

REFERENCES

[1] A. G. Riess, *et al*., "Observational evidence from supernovae for an accelerating universe and a cosmological constant", Astronomical Journal, **116**, 1009 (1998). https://doi.org/10.1086/300499

[2] S. Perlmutter, *et al*., "Measurements of Omega and Lambda from 42 high-redshift supernovae", Astrophysical Journal, **517**, 565 (1999). https://doi.org/10.1086/307221

[3] D. N. Spergel, *et al*., "First-year WMAP observations: determination of cosmological parameters", Astrophysical Journal Supplement Series, **148**, 175 (2003). https://doi.org/10.1086/377226

[4] M. Tegmark, Y. Wang, and M. Zaldarriaga, "New dark energy constraints from supernovae, microwave background, and galaxy clustering", Physical Review Letters, **92**, 241302 (2004). https://doi.org/10.1103/PhysRevLett.92.241302

[5] Carroll, S. M., "The cosmological constant", Living Reviews in Relativity 4, 1 (2001). https://doi.org/10.12942/lrr-2001-1

[6] S. R. Choudhury, *et al*., "Dark energy density from observational constraints", Physics Letters B, **650**, 1–6 (2007). https://doi.org/10.1016/j.physletb.2007.04.010

[7] G. 't Hooft, "Dimensional reduction in quantum gravity," gr-qc/9310026 (1993). https://arXiv:gr-qc/9310026

[8] L. Susskind, "The world as a hologram", Journal of Mathematical Physics, **36**, 6377 (1995). https://doi.org/10.1063/1.531249

[9] A. G. Cohen, D. B. Kaplan, and A. E. Nelson, "Effective field theory, black holes, and the cosmological constant", Physical Review Letters, **82**, 4971 (1999). https://doi.org/10.1103/PhysRevLett.82.4971

[10] M. Li, "A model of holographic dark energy", Physics Letters B, **603**, 1 (2004). https://doi.org/10.1016/j.physletb.2004.10.014

[11] C. Tsallis, "Possible generalization of Boltzmann–Gibbs statistics", Journal of Statistical Physics, **52**, 479 (1988). https://doi.org/10.1007/BF01016429

[12] A. Rényi, *Probability Theory*, (North-Holland Publishing, Amsterdam, 1970). https://www.elsevier.com/books/probability-theory/renyi/978-0-444-10168-1

[13] B. D. Sharma, and D. P. Mittal, "New nonadditive measures of entropy for discrete probability distributions," Journal of Mathematical Sciences, **10**, 28 (1975). https://doi.org/10.1007/BF02303867

[14] A. Jawad, S. Rani, and A. Chaudhry, "Sharma–Mittal holographic dark energy in modified gravity", European Physical Journal C, **77**, 349 (2017). https://doi.org/10.1140/epjc/s10052-017-4914-2

[15] A. Iqbal, and A. Jawad, "Cosmological behaviour of Sharma–Mittal holographic dark energy models", European Physical Journal C, **79**, 982 (2019). https://doi.org/10.1140/epjc/s10052-019-7497-9

[16] S. Maity, and U. Debnath, "Dynamics of Sharma–Mittal holographic dark energy models", Modern Physics Letters A, **34**, 1950356 (2019). https://doi.org/10.1142/S0217732319503563

[17] S.H. Shekh, and U. Debnath, "Stability of Sharma–Mittal holographic dark energy in anisotropic cosmology", International Journal of Geometric Methods in Modern Physics, **18**, 2150027 (2021). https://doi.org/10.1142/S0219887821500274

[18] C. Brans, and R. H. Dicke, "Mach's principle and a relativistic theory of gravitation", Physical Review, **124**, 925 (1961). https://doi.org/10.1103/PhysRev.124.925

[19] O. Bertolami, and P. J. Martins, "Nonminimal coupling and quintessence", Physical Review D, **61**, 064007 (2000). https://doi.org/10.1103/PhysRevD.61.064007

[20] V. Faraoni, *Cosmology in Scalar-Tensor Gravity*", (Kluwer Academic Publishers, Dordrecht, 2004). https://link.springer.com/book/10.1007/978-1-4020-1989-2

[21] M. R. Setare, and M. Jamil, "Holographic dark energy in non-flat Brans-Dicke cosmology", Journal of Cosmology and Astroparticle Physics, **03**, 010 (2010). https://doi.org/10.1088/1475-7516/2010/03/010

[22] S. Ghaffari, H. Hossienkhani, and T. Azizi, "Interacting holographic dark energy in Brans-Dicke theory", Astrophysics and Space Science, **361**, 161 (2018). https://doi.org/10.1007/s10509-016-2734-0

[23] B. Kiran, and D. R. K. Reddy, "Minimally interacting HDE models in Brans-Dicke theory", Modern Physics Letters A, **36**, 2150011 (2021). https://doi.org/10.1142/S0217732321500110

[24] V. U. M. Rao, and K. V. S. Sireesha, "Axially symmetric perfect fluid cosmological models in Brans-Dicke theory", African Review of Physics, **7**, 54 (2012). http://lamp3.tugraz.at/ hadley/arp/arp.html

[25] B. Saha, and P. Mondal, "Anisotropic dark energy cosmology in Brans-Dicke gravity", European Physical Journal C, **82**, 567 (2022). https://doi.org/10.1140/epjc/s10052-022-10494-2

[26] V. B. Johri, and R. Sudharshan, "Power-law Expansion and Inflation in Brans–Dicke Theory", Australian Journal of Physics, **42**(2), 215–222 (1989).

[27] V. B. Johri and K. Desikan, "Cosmological Models with Constant Deceleration Parameter in Brans–Dicke Theory," General Relativity and Gravitation, **26**, 1217–1232 (1994). https://doi.org/10.1007/BF02106714

[28] D. Trivedi and A.K. Bhabor, "Higher Dimensional Bianchi Type-III String Cosmological Models with Dark Energy in Brans–Dicke Scalar-Tensor Theory of Gravitation," New Astronomy, **89**, 101658 (2021).https://doi.org/10.1016/j.newast.2021.101658

[29] R. R. Caldwell, and E. V. Linder, "The Limits of Quintessence", Physical Review Letters, **95**, 141301 (2005). https://doi.org/10.1103/PhysRevLett.95.141301

[30] V. Sahni, T. D. Saini, A. A. Starobinsky, and U. Alam, "Statefinder A New Geometrical Diagnostic of Dark Energy," Journal of Experimental and Theoretical Physics Letters (JETP Letters), **77**(5), 201–206 (2003). https://doi.org/10.1134/1.1574831

АКСІАЛЬНО СИМЕТРИЧНА ГОЛОГРАФІЧНА ТЕМНА ЕНЕРГІЯ ШАРМА-МІТТАЛА В ТЕОРІЇ БРАНСА-ДІККЕ

Суреш Кадалі, **Ніліма Давулурі**

Кафедра математики та статистики, GITAM, (вважається університетом), Вішакхапатнам-530045, Індія

Це дослідження вивчає голографічну темну енергію Шарма-Міттала (SMHDE) в контексті теорії гравітації Бранса-Дікке в аксіально симетричній космологічній моделі. Використовуючи ентропію Шарма-Міттала, яка забезпечує об'єднуюче узагальнення ентропій Цалліса та Реньї, формулюється модифікована форма густини голографічної темної енергії для врахування неекстенсивних термодинамічних ефектів. Відповідні рівняння поля виведені та розв'язані для отримання точних аналітичних рішень. Крім того, ключові космологічні параметри, такі як параметр EoS, параметр уповільнення та квадрат швидкості звуку, систематично аналізуються для вивчення динамічної поведінки та стабільності моделі. Результати показують, що запропонована структура успішно описує прискорене розширення космосу наприкінці часу, а також враховує можливі анізотропії в ранньому космосі. Загалом, модель являє собою послідовне та фізично життєздатне розширення традиційних голографічних сценаріїв темної енергії в рамках скалярно-тензорної гравітаційної теорії.

Ключові слова: *ентропія Шарми-Міттала; голографічна темна енергія; Теорія Бранса-Дікке; аксіально-симетрична метрика*

East European Journal of Physics. 2. 622-632 (2026)
DOI:10.26565/2312-4334-2026-2-69 ISSN 2312-4334

EPITAXIAL STABILIZATION AND RADIATION-STIMULATED SEGREGATION IN CA-PVD AlN/CrN MULTILAYER COATINGS UNDER ION BOMBARDMENT

O.V. Maksakova*, V.M. Beresnev, S.V. Lytovchenko, R.S. Galushkov
V.N. Karazin Kharkiv National University, 4, Svoboby Sq., 61000 Kharkiv, Ukraine
**Corresponding Author e-mail: o.maksakova@karazin.ua*
Received February 2, 2026; revised April 10, 2026; accepted April 20, 2026

This paper investigates the regularities governing the formation of the atomic-crystalline architecture, surface topography, and chemical composition of AlN/CrN multilayer coatings deposited via cathodic arc physical vapor deposition onto AISI 321 austenitic stainless-steel substrates. The synergistic effect of the negative substrate bias voltage (–50, –100, and –200 V) and the deposition duration of individual AlN layers (10, 40, and 60 s) on the kinetics of phase competition and the evolution of radiation-stimulated nanostructures was analyzed. Using X-ray diffraction and scanning electron microscopy, combined with energy-dispersive X-ray spectroscopy, it was established that at low deposition energies (–50 V, 10 s), the epitaxial template effect of the c-CrN matrix dominates, thereby stabilizing the metastable cubic c-AlN phase. Increasing both the layer thickness and the substrate bias to –100 V leads to the breakdown of pseudomorphic growth and transitions the system into a possible nanocrystalline or quasi-amorphous state. At high bias potential of -200 V, complete thermal relaxation occurs, accompanied by a textured phase transition of AlN into its stable hexagonal wurtzite modification (h-AlN). A counterintuitive decrease in the aluminum concentration (from 46.88 to 33.72 at. %) despite the prolonged growth time was observed. This phenomenon is driven by the selective re-sputtering of lighter Al atoms under the influence of a high-energy ion flux. Furthermore, radiation-stimulated interdiffusion of iron from the substrate into the coating, along with an ion-cleaning effect that removes interstitial carbon impurities from the matrix, was recorded. The insights obtained expand current understanding of non-equilibrium solid-state thermodynamics and open new possibilities for the precision tailoring of nanostructured protective coatings by optimizing ion-plasma parameters.
Keywords: *PVD; Nitrides; Multilayer coatings; AlN; CrN; Microstructure; Chemical composition; Phase state*
PACS: 68.55.Jk, 68.65.Ac

1. INTRODUCTION

In the context of the intensive development of modern condensed matter physics, ion-plasma technologies, and materials science of extreme states, a fundamental understanding of structure-formation processes in thin-film heterophase systems is of paramount importance. The investigation of the atomic-crystalline architecture of films synthesized under non-equilibrium conditions of high-energy ionic bombardment allows for the revelation of profound physical aspects of phase stability, the regularities governing the formation of metastable states, and the specific features of interfacial mass transfer. Unlike classical applied approaches that focus exclusively on recording macroscopic performance characteristics, the analysis of substructural variations reveals regularities in atomic diffusion, lattice relaxation, and energy balance at nanolayer interfaces [1, 2]. Structural investigations using X-ray diffraction (XRD), scanning electron microscopy (SEM), and energy-dispersive X-ray spectroscopy (EDS) are key tools for verifying theoretical models of non-equilibrium solid-state thermodynamics [3].

Among the diverse binary and ternary nitride systems, the combination of aluminum nitride (AlN) and chromium nitride (CrN) is of particular fundamental interest. The physical appeal of investigating this specific pair lies in the unique combination of their individual structural constants, thermodynamic parameters, and coordination geometries [4]. While chromium nitride forms a stable cubic lattice of the NaCl-type (space group $Fm\bar{3}m$, B1 structure) with octahedral atomic coordination at room temperature and atmospheric pressure, aluminum nitride under identical conditions crystallizes into a stable hexagonal wurtzite modification (space group $P6_3mc$, B4 structure) featuring tetrahedral coordination [5]. Combining two phases with distinct lattice symmetries and different coordination numbers (CN = 6 for CrN and CN = 4 for AlN) within a single thin-film system establishes conditions for severe structural competition and localized lattice instability [6].

The physical structure of these coatings is highly intricate, both in single-layer form (an unmixed ternary alloy, Al-Cr-N) and in multilayer periodic architectures. In single-layer configurations, research primarily focuses on the solubility limit of aluminum in the cubic lattice of CrN, forming a supersaturated substitutional solid solution, c-$Al_xCr_{1-x}N$ [2]. Replacing Cr atoms with Al atoms, which possess a smaller atomic radius, induces severe local lattice distortion, alters interplanar distances, and elevates the internal free energy of the system [6]. Upon reaching a critical Al concentration, a first-order phase transition occurs, accompanied by the collapse of the cubic symmetry and the precipitation of the hexagonal h-AlN phase [5, 9].

Transitioning to a multilayer periodic architecture opens up entirely new physical phenomena, the key among which is the epitaxial (pseudomorphic) stabilization of metastable phases [1, 7]. When the thickness of individual AlN

Cite as: O.V. Maksakova, V.M. Beresnev, S.V. Lytovchenko, R.S. Galushkov, East Eur. J. Phys. 2, 622 (2026), https://doi.org/10.26565/2312-4334-2026-2-69

nanolayers is compressed below a certain critical threshold, the coherent matching at the interfaces with the cubic CrN matrix forces the aluminum atoms to rearrange from a tetrahedral to an octahedral configuration [7]. This effectively results in the artificial stabilization of the high-pressure metastable cubic phase, c-AlN (NaCl-type), under ambient pressure conditions [1, 11]. Investigating the specific conditions under which this epitaxial constraint breaks down – thereby giving rise to diffuse halos and the subsequent relaxation of the system into the hexagonal wurtzite structure – stands as a fundamental problem in solid-state physics [5, 11].

The realization of such complex non-equilibrium states requires the deployment of high-energy techniques for plasma flux generation, among which cathodic arc deposition possesses the highest kinetic and thermodynamic efficiency [1, 3]. The physical essence of the cathodic arc process lies in the evaporation of the cathode material within localized arc spots, ensuring virtually 100% ionization of the working gas-metal flux and generating multiply charged ions (Al^{+}, Al^{2+}, Cr^{+}, Cr^{2+}, Cr^{3+}) [1, 10]. In contrast to conventional magnetron sputtering, where the average particle energy rarely exceeds several electron volts, cathodic arc technology ensures that ions arrive at the substrate with an intrinsic kinetic energy of 20 to 100 eV even before an external bias is applied [1, 8].

The uniqueness introduced by cathodic arc technology in AlN/CrN coatings stems from the ability to exert deep control over the phase composition via radiation-stimulated mass transfer mechanisms [2, 3]. Applying a negative substrate bias voltage accelerates the ion flux, thereby transforming the plasma potential energy into the kinetic energy of collision cascades on the surface of the growing film [8, 10]. This yields a series of unique structural effects. The first of them is a dynamic control over texture and defect formation. High-energy ion assistance drives the directed generation of point defects (vacancies and interstitials), thereby altering interatomic diffusion parameters and forcing the lattice to crystallize along rigorously predefined crystallographic orientations [8]. The second one is the effect of mass-dependent preferential re-sputtering. At extreme substrate biases, high-energy ions begin to selectively eject the lighter Al atoms (m_{Al} = 26.98 amu) compared to the heavier Cr atoms (m_{Cr} = 52.00 amu) from the already formed lattice [5]. This leads to unique stoichiometric shifts that run counter to the classical kinetic laws, which are strictly governed by deposition time [10]. The third effect is the presence of the cathodic droplet phase. A specific microstructural element of the cathodic arc method– – microdroplets ejected from the cathode target – creates a unique heterogeneous surface topography [1, 4]. These droplets act as localized centers of deformation and shadowing, tilting the growth trajectories of columnar grains and uniquely contributing to X-ray diffraction patterns due to verified phase discrepancies between the droplet body and its immediate periphery [1, 2].

The present research represents the precision analysis of the structural-phase and elemental transformations in AlN/CrN multilayer coatings (MLCs) deposited via CA-PVD onto AISI 321 austenitic stainless-steel substrates under the synergistic variation of energetic and temporal parameters. Throughout the experiments, the negative substrate bias voltage was systematically varied across critical points of energetic impact (–50 V, –100 V, and –200 V). Concurrently, the deposition duration of the individual AlN layers was sequentially adjusted to 10, 40, and 60 seconds.

The primary objective of this study is to uncover the fundamental physical causes behind the alterations in XRD diffraction profiles, topographical modifications captured by SEM, and the redistribution of elemental sublattices (including the behavior of impurity carbon atoms and interdiffusional iron originating from the substrate) monitored via EDS. The insights obtained expand current understanding of phase-competition kinetics and ion-stimulated evolution of nanostructures in the highly non-equilibrium thermodynamic environment of a cathodic arc plasma.

2. EXPERIMENTAL DETAILS

2.1. Deposition

The AlN/CrN MLCs were deposited by ion-plasma deposition (CA-PVD) in a reactor-type vacuum chamber (Bulat-6) equipped with two arc evaporators. Technically pure, separate aluminum and chromium targets, positioned symmetrically relative to the substrate holder, were used as cathode materials. The substrates were AISI 321 stainless steel (12X18H9T UA standard), previously mechanically polished to a mirror finish and ultrasonically cleaned in organic solvents. The selection of substrates was dictated by the requirements of optimal lattice matching, adequate thermal expansion compatibility with the AlN and CrN layers, and ensuring strong interfacial adhesion. Prior to coating deposition, the substrate surface was ion-cleaned in argon plasma at an elevated substrate bias to remove surface contaminants and activate the substrate.

Deposition parameters for all coatings are listed in Table 1. All MLCs were synthesized in a reactive nitrogen atmosphere at a constant pressure of 0.53 Pa. The nitrogen pressure was established through extensive preliminary experiments to identify the boundaries of the metallic-to-poisoned transition zone in the aluminum and chromium targets. At a nitrogen pressure of 0.53 Pa, nitrogen was insufficient to form nitride phases, and metallic dominated the coating composition. The selected value thus encompasses the complete transition from the formation of Al2N or Cr2N sub-nitrides to stable stoichiometric AlN and CrN. The negative substrate bias was varied to –50, –100, and –200 V, allowing investigation of the effect of ion bombardment energy on the structural evolution and composition of the coatings. The arc currents for the Cr and Al cathodes were maintained in the ranges of 105–110 A and 95–100 A, respectively, while the foil currents were adjusted within 0.4–0.5 A for Cr and kept at 0 A for Al. Minor variations in the arc and foil currents were introduced to stabilize the plasma discharge and compensate for target erosion, thereby ensuring a constant deposition rate and uniform plasma density across all processes. The deposition time for the AlN layers was systematically varied at 10, 40, and 60 seconds, while the CrN layer deposition parameters remained fixed. This variation was introduced to investigate the effects of evolution on phase, crystalline structure, elemental composition, and morphology.

Table 1. Technological parameters of AlN/CrN MLCs deposited by CA-PVD

AlN/CrN MLCs	Arc current (Cr/Al), A	Foil current (Cr/Al), A	Substrate bias, V	Nitrogen pressure, Pa	Deposition time Cr layer, s	Deposition time Al layer, s	Total deposition time, h	Bilayer quantity
1558	110/95	0.5/0	–50	0.53	10	10	1.65	70
1565	105/100	0.4/0	–100	0.53	10	40	1	72
1556	110/95	0.5/0	–200	0.53	10	60	1	55

Figure 1 shows a schematic of the CA-PVD deposition process for AlN/CrN MLCs. A chromium adhesion layer with a nanometer-scale thickness was first deposited to improve coating adhesion to the steel substrate. The multilayer structure was formed by periodically rotating the substrates relative to the evaporation sources, which ensured the sequential deposition of AlN and CrN layers. Three series of AlN/CrN MLCs were deposited with a bilayer number of 70, 72, and 55. The variation of a bilayer number was deliberately made to optimize the balance in total thickness of all MLCs and evaluate the same structural characteristics (including morphology, phase state and chemical composition).

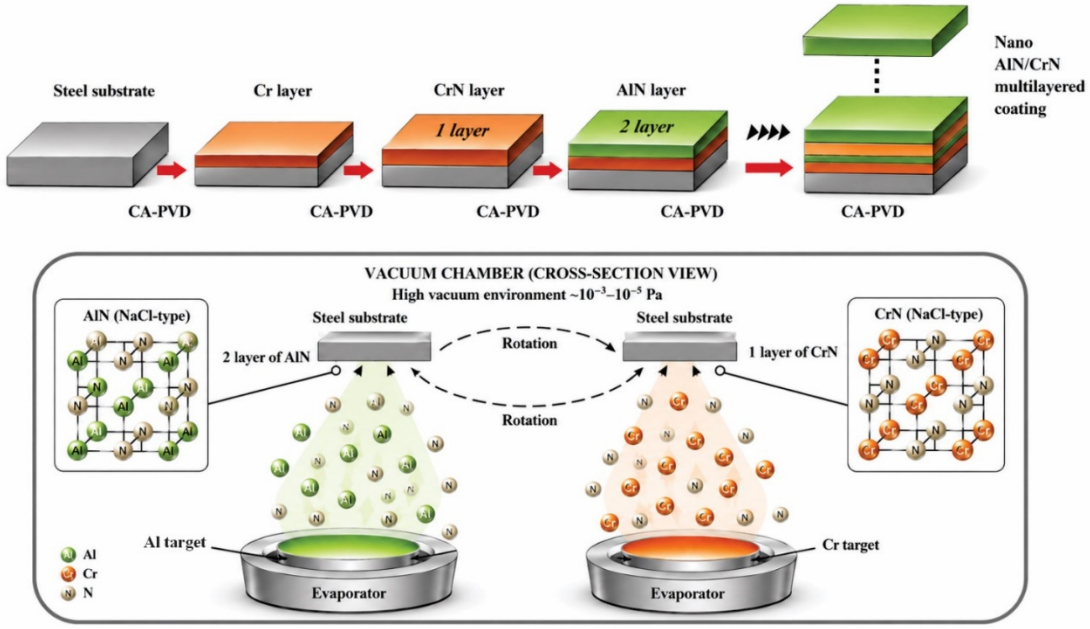

Figure 1. Schematic of AlN/CrN multilayer coating deposition by CA-PVD using separate Al and Cr targets with substrate rotation

2.2. Characterization

The surface morphology and topographic features of AlN/CrN MLCs were investigated by scanning electron microscopy (SEM) using a VEGA3 TESCAN scanning electron microscope. The microscopic analysis was conducted in the secondary electron (SE) detection mode to maximize surface-sensitive topographic contrast. The accelerating voltage of the primary electron beam (SEM HV) was maintained at 30.0 kV. The images were captured at working distances (WD) ranging between 15.07 mm and 19.72 mm. To ensure a comprehensive evaluation of the coating surface features, the analysis was performed across different scales: a low-magnification mode with a view field of 500 µm (utilizing a 100 µm scale bar) was used for overall surface overview. A high-magnification mode with a view field of 17.7 µm (utilizing a 10 µm scale bar) was employed for detailed examinations of localized surface fragments.

The phase composition and structural parameters of AlN/CrN MLCs were characterized by X-ray diffraction (XRD) analysis using a diffractometer operated in the “theta–2theta” geometry. The diffraction patterns were recorded utilizing Cu-Kα radiation (λ = 1.540600 A) generated from a Cu target at an operating voltage of 30.0 kV and a tube current of 30.0 mA. The optical system of the diffractometer was configured with a 1.0° divergence slit, a 1.0° scatter slit, and a 0.150 mm receiving slit. Data collection was performed in a continuous scanning mode over a 2theta angular range of 10.0°–100.0° at a scanning speed of 2.0°/min, a sampling pitch (step size) of 0.02°, and a preset time of 0.60 s per step. Phase identification, qualitative search-match analysis, and profile fitting were carried out using the Match! software package (Crystal Impact) linked with the International Center for Diffraction Data (ICDD) PDF-2 (Release 2004) reference database. The evaluation of the average crystallite size (sub-grain domain size) was performed via the Scherrer equation using a shape factor (Scherrer constant) of 0.94.

The elemental composition and distribution within the AlN/CrN MLCs were analyzed by energy-dispersive X-ray spectroscopy (EDS). The measurements were performed using an EDS detector integrated into the VEGA3 TESCAN scanning electron microscope. X-ray generation and spectrum collection were carried out over an energy range from 0 to 15 keV, recording characteristic emission intensities in counts per electron volt (cps/eV). Identification and deconvolution

of the overlapping elemental lines, specifically the low-energy light element region comprising Carbon (C-K), Nitrogen (N-K), and Aluminum (Al-K), alongside the transition metal series of Chromium (Cr-K), and Iron (Fe-K)), were executed using the integrated microscope software.

3. EXPERIMENTAL RESULTS

3.1. Surface structure

Figure 2 (left side) illustrates the surface morphology of AlN/CrN MLC deposited at a substrate bias of –50 V. The low-magnification image (at a 100 μm scale) reveals a highly developed surface topography typical for arc-plated films, heavily populated by macroparticles (droplets). This droplet phase generation is directly linked to the liquid metal emission from the cathode spots at arc currents of 110 A (Cr) and 95 A (Al). A detailed analysis indicates a polydisperse distribution of the macroparticles. Large, irregularly shaped solidified splats with sizes ranging from 15 to 35 μm are randomly distributed across the surface, with a spatial frequency of approximately 40–80 μm between them. Spherical droplets of medium (2–8 μm) and submicron (less <1 μm) sizes are also observed. The high-magnification SEM image (at a 10 μm scale) shows that the large droplets underwent significant flattening upon high-velocity impact with the substrate before solidification.

Planimetric evaluation demonstrates that the droplet-free matrix occupies approximately 75–80% of the total surface area, while the macroparticles and associated boundary defects cover the remaining 20–25%. The substrate bias of –50 V provided insufficient ion bombardment energy to suppress or re-sputter these large metallic aggregates during growth. The surface matrix exhibits a fine-grained, slightly dome-like texture, which is possibly indicative of a dense, competitive columnar growth of the alternating AlN and CrN nanolayers (at 10 s deposition cycles).

The surface morphology of AlN/CrN MLC deposited at an increased negative substrate bias of –100 V and an asymmetric layer deposition time (Cr/Al = 10/40 s) is presented in Figure 2 (center side). The low-magnification SEM image (at a 100 μm scale) reveals a modified topography compared to the previous sample, characterized by a reduction in the count of sharp volumetric macroparticles and the appearance of distinct crater-like tracks and flattened rims. The high-magnification view (at a 10 μm scale) captures a large, complex-shaped solidified metallic splat (~20–25 μm in size) with highly flattened, smoothed boundaries. This morphological evolution is directly attributed to the higher substrate bias of –100 V, which enhances the kinetic energy of the incident ion flux. The intense ion bombardment induces a noticeable re-sputtering effect on the protruding elements of the liquid droplet phase and stimulates lateral adatom diffusion during crystallization.

Statistical image processing indicates that the defect-free matrix area expanded to approximately 82–85% of the total surface, leaving only 15–18% occupied by macroparticles and associated boundary defects. The extended deposition time of the AlN layer (40 s) acts as a planarizing factor, effectively encapsulating the underlying droplet-induced roughness. Under these energetic conditions, the surface matrix may have acquired a significantly denser, highly smoothed sub-microcrystalline surface texture with suppressed competitive columnar dome formation, thereby ensuring a more uniform multilayer architecture.

The surface morphology of AlN/CrN MLC, deposited at an elevated negative substrate bias of –200 V and an asymmetric growth cycle (Cr/Al = 10/60 s), is illustrated in Figure 2 (right side). The low-magnification SEM micrograph (at a 100 μm scale) reveals a significantly modified, flattened surface topography. The application of high-energy ion bombardment (–200 V) activates intense sub-surface atomic displacement and energetic re-sputtering processes, which fundamentally alter the macroparticle evolution. The high-magnification view (at a 10 μm scale) focuses on a highly deformed macrodefect boundary, highlighting the joint effect of intense ion shearing and matrix overgrowth. Under a strict ion-assisted regime at –200 V, the arriving high-velocity nitrogen and metal ions severely erode and flatten the protruding liquid metallic droplets ejected from the cathodes. The extended 60 s deposition window for the AlN layer allows the matrix to structurally assimilate and fragment the droplet inclusions, completely erasing sharp phase boundaries. The remaining defect fraction is represented by highly planarized splats and shallow, smoothed craters.

Planimetric image analysis reveals a noticeable reduction in the defect-free matrix area, which drops to approximately 65–70% of the total surface, while the macroparticle occupation and associated micro-craters expand to 30–35%. This topographical degradation indicates that at an extreme negative substrate bias of –200 V combined with an extended AlN deposition time of 60 s, a defect accumulation mechanism becomes dominant. The high-energy incident ion flux induces preferential re-sputtering of the growing nitride matrix, thereby exposing and topographically highlighting the heavier metallic droplets that possess lower sputtering yields.

A comparative analysis of the surface morphology across the three investigated AlN/CrN MLCs reveals a non-monotonic transition in growth mechanisms governed by the synergy of substrate bias and AlN deposition time. At a low substrate bias of –50 V and short symmetric cycles (Cr/Al = 10/10 s), the coating surface is characterized by sharp, open macroparticles covering up to 25% of the area within a typical competitive columnar matrix. Increasing the bias to –100 V with an asymmetric cycle (Cr/Al = 10/40 s) introduces an optimal energetic window where ion-induced re-sputtering flattens droplet boundaries and activates adatom mobility, successfully expanding the clean matrix fraction to its maximum of 82–85%. However, escalating the negative bias to an extreme value of –200 V coupled with a prolonged 60 s AlN cycle triggers a severe over-bombardment regime. In this state, the clean matrix area shrinks back to 65–70% due to preferential ion etching of the nitride phases, which accentuates and exposes the un-sputtered metallic droplet aggregates. This severe ion-assisted treatment effectively suppresses the standard competitive columnar growth but yields

a highly stressed, fragmented, and topographically developed nanostructured surface architecture with the highest defect density among the altered parameters.

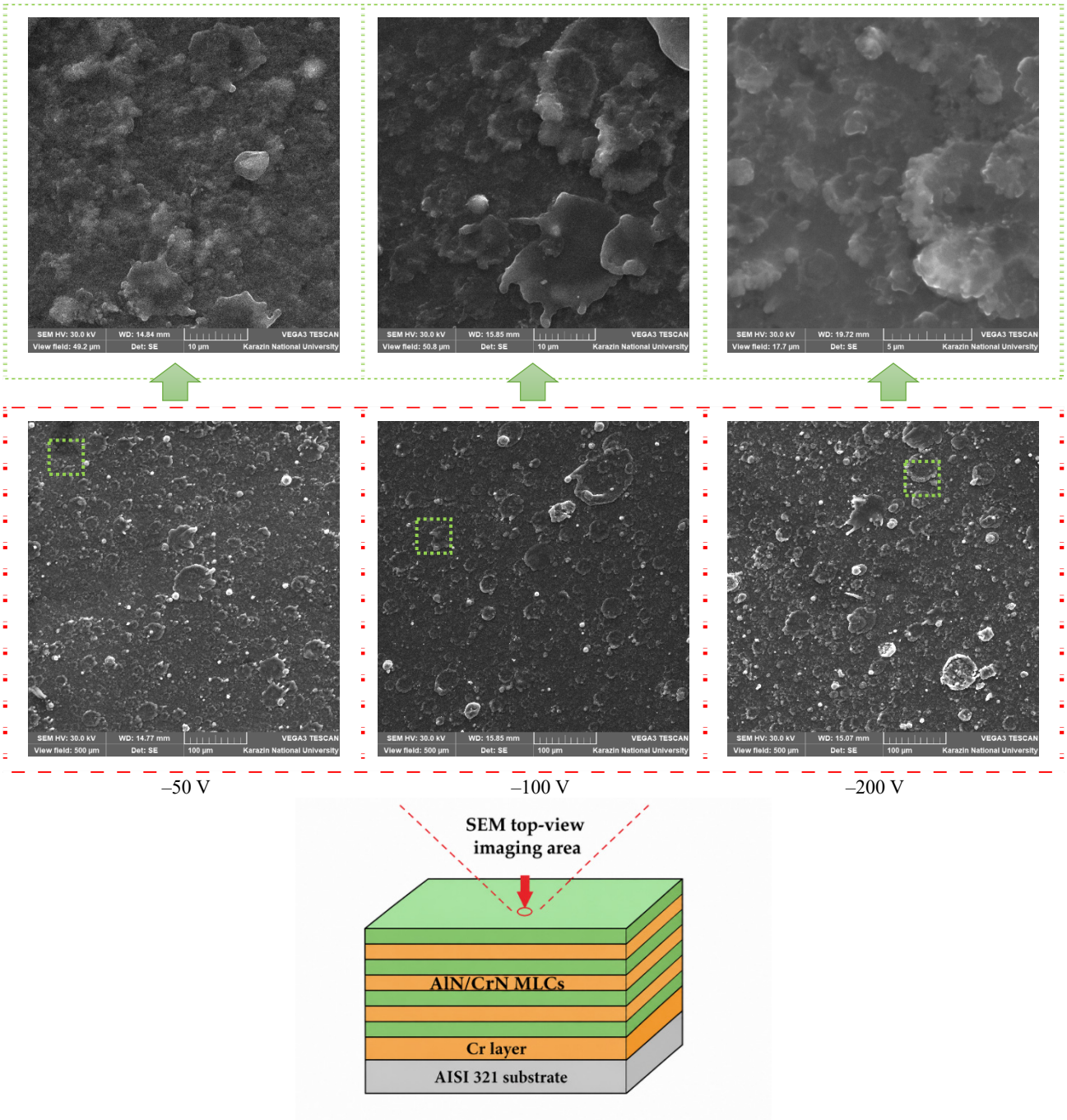

Figure 2. SEM images of AlN/CrN multilayer coatings deposited by CA-PVD at different substrate biases –50 V (left side), –100 V (center side) and –200 V (right side)

3.2. Structural-phase state

X-ray structural analysis of AlN/CrN MLCs, presented in Figure 3, reveals a heterophase crystalline structure. This structure consists of a mixture of stable cubic chromium nitride (c-CrN) with a NaCl-type structure, metastable cubic aluminum nitride (c-AlN) also possessing a NaCl-type structure, and stable hexagonal aluminum nitride (h-AlN) with a wurtzite structure.

On the X-ray pattern of AlN/CrN MLC deposited at substrate bias of –50 V, a doublet of peaks in the interval 2theta ≈ 32–36° is clearly visible. The first broad maximum at 2theta = 35.51° is formed due to the superposition of the h-AlN(002) and c-CrN(111) planes. The presence of the c-AlN(111) conjugate peak at 2theta = 38.43° confirms that with an ultrashort deposition time (10 s) the c-CrN lattice exerts a strong stabilizing (epitaxial) effect, forcing a significant part of the AlN phase to crystallize in the metastable cubic modification. A weak reflex of the hexagonal h-AlN(100) phase is

also recorded at 2theta ≈ 32.6°. The presence of a pronounced peak at 2theta = 64.87° (c-AlN(220) / h-AlN(103)) probably indicates that the coating has a polycrystalline structure with developed interphase boundaries.

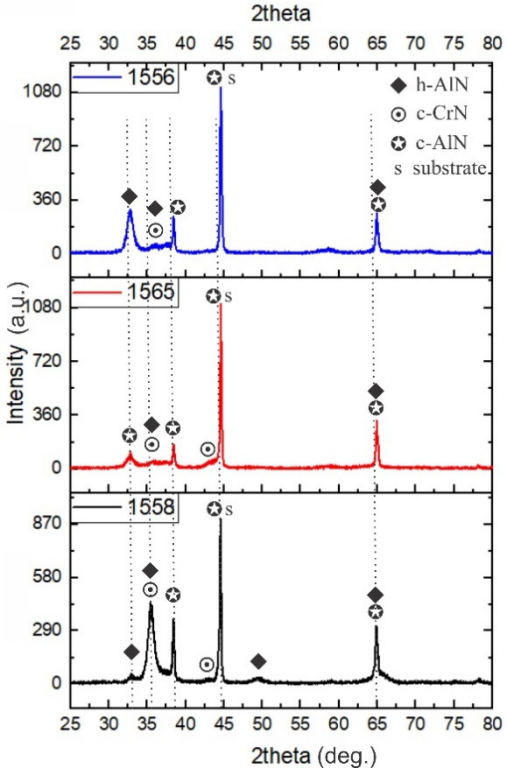

Figure 3. XRD patterns of AlN/CrN multilayer coatings deposited by CA-PVD at different substrate biases: –50 V (bottom pattern), –100 V (center pattern) and –200 V (top pattern)

For the following AlN/CrN MLC, increasing the deposition time of the AlN layer to 40 s, in combination with increasing the substrate bias to –100 V, radically changes the thermodynamics and kinetics of the transformed phases. A sharp drop in intensity and a significant broadening of all diffraction maxima of the coating in the range 2θ ≈ 32-40° are observed. The peak at 2θ = 36.07° (h-AlN/c-CrN) practically levels off, transforming into a diffuse halo. The observed changes are caused by two factors. First, the growth of the bias potential to –100 V intensifies ion bombardment, destructuring the crystal lattice and grinding the grain to a nanocrystalline or quasi-amorphous state. Secondly, increasing the thickness of the AlN layer (40 s) removes the system from the zone of epitaxial influence of cubic c-CrN. Within the AlN layer, a competition between the metastable cubic and stable hexagonal phases leads to strong internal microstresses, an increase in the density of packing defects, and a decrease in the intensity of the XRD signal.

For AlN/CrN MLC, an extreme increase in substrate bias to –200 V and a long growth cycle of AlN (60 s) shifts the structural mechanism towards radiation-stimulated phase segregation. A pronounced "return" of peak intensity is observed. The X-ray pattern is dominated by a clear, intense, and relatively narrow peak at 2theta = 32.75°, corresponding to the h-AlN(100) plane. At the same time, the peak at 2theta = 37.48° becomes low-intense and broad, and the reflex of cubic c-AlN(111) at 2theta = 38.47° again acquires an increase of intensity. The long continuous operation time of the aluminum evaporator (60 s) under hard ion assistance (–200 V) provides excess kinetic and thermal energy to the adatoms. This initiates the processes of dynamic return (recrystallization) and grain coalescence. The AlN phase is completely freed from epitaxial clamping on the part of c-CrN (since the layer becomes too thick) and thermodynamically relaxes into its stable hexagonal wurtzite form with a pronounced preferential orientation (texture) along the (100) plane.

Table 2. Summarized X-ray parameters of AlN/CrN MLCs deposited by CA-PVD at different substrate biases

2 theta, deg.	d-spacing, A	Identified phase	Crystallographic plane (*hkl*)	PDF card No.
32.75-32.89	2.7211-2.7319	h-AlN	(100)	01-070-2543
35.51-37.48	2.5260-2.7312	h-AlN/c-CrN	(002)/(111)	01-070-2543/00-011-0065
38.43-38.47	2.3404-2.3383	c-AlN	(111)	00-046-1200
43.75	2.0676	c-CrN	(200)	00-011-0065
44.56-44.61	2.0295-2.0315	substrate+c-AlN	(200)	00-046-1200
49.37	1.8444	h-AlN	(102)	01-070-2543
64.87-64.93	1.4349-1.4361	substrate+(h-AlN+c-AlN)	(220)+(103)	01-070-2543/00-046-1200

The average crystallite size for all investigated AlN/CrN MLCs was evaluated via the Scherrer formula, using the diffraction data of the most intense (dominant) textured peak corresponding to the hexagonal h-AlN modification. It was

established that variations in the deposition parameters exert a significant influence on the orientational stability and structural dispersion of the coatings. Specifically, for the AlN/CrN MLC obtained at substrate bias of –50 V and equal layer deposition times (Cr/Al = 10/10 s), the dominant reflection appears at 2theta = 35.51°, which is characterized by the minimum crystallite size in the series, measuring 13±2 nm. With an increase in the negative bias to –100 V and a prolonged aluminum layer growth duration (Cr/Al = 10/40 s), a shift in the preferred orientation is observed. The peak at 2theta = 32.81° becomes dominant, while the grain size slightly increases to 16±2 nm. This indicates an intensification of the hexagonal phase crystallization process under conditions of increased AlN layer thickness. A further increase in the energy of the bombarding ions at a bias of –200 V and an asymmetric deposition time (Cr/Al = 10/60 s) localizes the main diffraction maximum at 2theta = 32.75°. Concurrently, a minor reduction in the grain size down to 14±2 nm was recorded. This dynamic is attributed to enhanced ion re-sputtering and the generation of high residual stresses under extreme substrate biases, which ultimately restricts the diffusion growth of the crystallites.

3.3. Elemental composition

The elemental composition analysis of AlN/CrN MLCs deposited at various negative substrate biases (–50 V, -100 V, and –200 V) is presented in Table 3 and Figure 3.

Table 3. Elemental composition of AlN/CrN MLCs deposited by CA-PVD at different substrate biases: –50 V, –100 V, and –200 V

AlN/CrN MLCs	Substrate bias, V	Cr/Al deposition time, s	Elemental composition, at.%					
			Al	Cr	N	C	Fe	Total
1558	–50	10/10	46.88	6.15	45.94	0.68	0.35	100
1565	–100	10/40	45.21	18.37	35.69	0.26	0.47	100
1556	–200	10/60	33.72	21.21	44.31	0.14	0.62	100

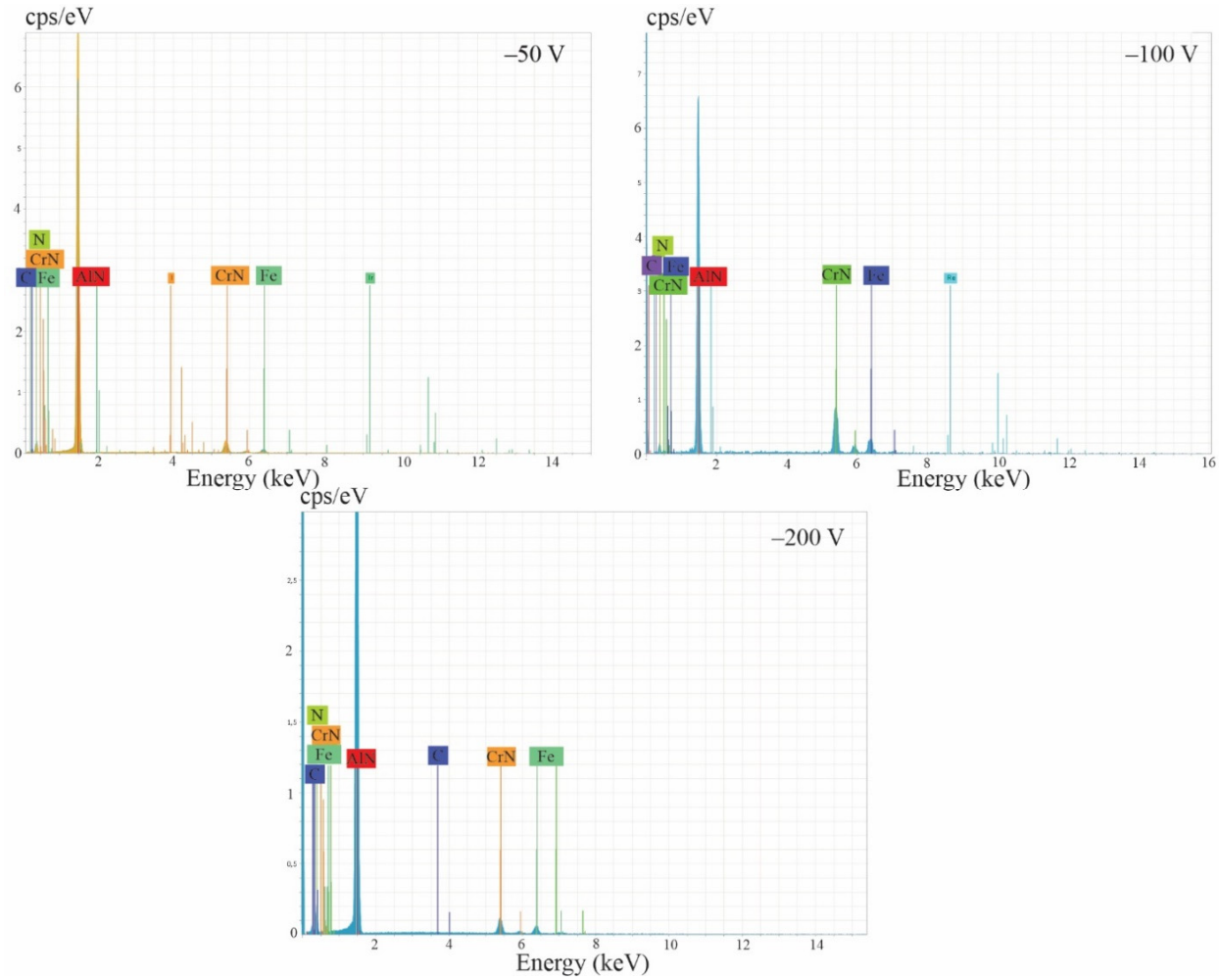

Figure 3. EDS spectra of AlN/CrN multilayer coatings deposited by CA-PVD at different substrate biases: –50 V (left spectrum), –100 V (right spectrum) and –200 V (center spectrum)

The elemental composition of the AlN/CrN MLC deposited at a substrate bias of –50 V and equal layer growth times (Cr/Al = 10/10 s) exhibits a high aluminum concentration of 46.88 at. %. The chromium content is minimal, at 6.15 at. %,

resulting in a high Al/Cr atomic ratio. Nitrogen constitutes 45.94 at. %, which is close to the stoichiometric ratio expected for a dominant AlN phase mixed with a smaller fraction of CrN. Trace amounts of carbon (0.68 at. %) and iron (0.35 at. %) are also detected within the coating matrix.

As the negative substrate bias is increased to –100 V and the aluminum layer deposition time is prolonged to 40 s (Cr/Al = 10/40 s), the elemental composition undergoes a noticeable transition. Despite the fourfold increase in the Al layer deposition time, the aluminum content slightly decreases to 45.21 at.%. Concurrently, the chromium concentration increases significantly to 18.37 at. %, while the nitrogen content drops to 35.69 at. %, suggesting a variation in phase stoichiometry. The carbon impurity level drops to 0.26 at. %, whereas the iron concentration slightly increases to 0.47 at. %.

At the highest negative substrate bias of –200 V and maximum aluminum layer deposition duration (Cr/Al = 10/60 s), a counterintuitive elemental distribution is observed. The aluminum content drops significantly to 33.72 at. %, representing the lowest Al concentration in the series. In contrast, the chromium content reaches a maximum of 21.21 at. %, while the nitrogen content returns to 44.31 at.%. The concentration of carbon impurities is minimized to 0.14 at. %, while the iron content reaches its peak value of 0.62 at. %.

In summary, elemental composition analysis of the investigated AlN/CrN MLCs revealed a counterintuitive decrease in the aluminum concentration (from 46.88 to 33.72 at. %) along with a concomitant increase in the chromium content as the ion bombardment energy was elevated. This phenomenon is driven by the preferential re-sputtering of the lighter aluminum atoms (m_{Al} = 26.98 amu vs. m_{Cr} = 52.00 amu) under the influence of high-energy ions at a substrate bias of -200 V, which effectively counteracts the effect of the prolonged Al layer deposition time. The presence of iron (0.35-0.62 at. %) is attributed to ion-stimulated interdiffusion from the AISI 321 stainless steel substrate, whereas the reduction in carbon content (down to 0.14 at.%) at higher negative biases is explained by the ion cleaning effect, which promotes the desorption of impurities.

High bias energies at –200 V induce severe lattice distortion, vacancy generation, and stress-driven diffusion. Under these extreme conditions, the thermodynamically more stable CrN phase suppresses the growth of metastable Al-containing phases. Consequently, the excess aluminum may be displaced to the grain boundaries, forming amorphous interlayers, or undergoes continuous secondary re-sputtering by plasma ions, thereby reducing its overall atomic fraction as detected by energy-dispersive X-ray spectroscopy (EDS).

4. DISCUSSIONS

4.1. Correlation between Deposition Parameters, Composition, and Phase Evolution

The structural and compositional evolution of the synthesized AlN/CrN MLCs is governed by a complex interplay of thermodynamics and kinetics. This behavior is dictated by the simultaneous modification of the negative substrate bias voltage (–50 V to –200 V) and the systematic expansion of the AlN layer growth window (t_{Al} = 10, 40, 60 s).

The epitaxial template effect is dominant at low deposition energies (–50 V, 10 s). At this stage, the incoming adatoms possess relatively low kinetic energy. The crystallization process is dominated by the structural constraint of the underlying cubic CrN template (B1, NaCl-type) [12]. Due to the minimal thickness of the AlN layer, the interface strain energetically minimizes the volume free energy required for the formation of the metastable cubic AlN modification (c-AlN), space group (Fm3m) [13]. This template effect forces a significant portion of AlN to mirror the rock-salt structure of CrN, as confirmed by the strong c-AlN(111) reflection at 2theta = 38.43°. At this stage, the hexagonal wurtzite phase h-AlN is possibly suppressed, manifesting with an isolated h-AlN(100) peak.

The competitive phase boundary disruption appears during mid-deposition energies (–100 V, 40 s). Transitioning to substrate bias of –100 V while simultaneously lengthening the AlN deposition step to 40 s breaks this pseudomorphic growth state. The increased layer thickness shifts the upper boundary of the AlN layer far beyond the spatial envelope of the epitaxial clamping exerted by the c-CrN lattice. As a result, the AlN phase attempts to relax into its thermodynamically stable hexagonal configuration (h-AlN, B4 wurtzite type). The overlap of competing tetrahedral (hexagonal) and octahedral (cubic) coordination matrices produces a localized structural mismatch [14]. This structural conflict manifests on the XRD profiles as severe peak attenuation and the formation of a diffuse halo in the 2theta ≈ 32–40° interval. Concurrently, the elevated ion bombardment at –100 V induces widespread lattice defects and grain refinement, reducing the long-range crystalline order to a quasi-amorphous state [15].

The radiation-stimulated segregation and coalescence start to dominate at high-deposition energies (–200 V, 60 s). At these parameters, the structural mechanism shifts entirely toward radiation-stimulated phase segregation and thermal relaxation [15]. High-velocity ion flux (N^+) delivers extensive kinetic energy directly to the film surface. This energy accelerates localized atomic displacement and adatom mobility. Because the 60 s growth interval yields an Al-rich environment independent of the CrN template, the excess energy facilitates dynamic recrystallization and grain coalescence. The AlN system completely escapes the interfacial strain of CrN, allowing the phase to crystallize into its highly textured, stable hexagonal wurtzite form along the h-AlN(100) plane at 2theta = 32.75°.

4.2. Analytical Insight into Mass-Dependent Preferential Re-sputtering Mechanisms

The elemental tracking shown in Table 3 reveals an unexpected composition profile: the net atomic concentration of Al drops from 46.88 at.% to 33.72 at.% despite a sixfold increase in the Al-target evaporation time. This compositional shift is driven by the physics of ion-surface interactions under varying acceleration potentials.

This phenomenon is governed by the discrepancy in atomic mass between the constituent transition metal and the principal group-III element (m_{Al} = 26.98 amu versus m_{Cr} = 52.00 am) [16]. According to classical cascade sputtering theories, the energy transfer coefficient (γ) during a binary atomic collision is maximized when the masses of the incident projectile particle (m_1, e.g., N^+) and the target atom (m_2) are closely matched:

$$\gamma = \frac{4m_1m_2}{(m_1 + m_2)^2}$$

Because the mass of nitrogen (m_N = 14.01 amu) sits closer to that of aluminum than chromium, energy transfer to the Al sublattice is highly efficient. At a low bias of –50 V, the incident ion energy remains below the threshold required for meaningful sub-surface sputtering, preserving the nominal deposition rates and yielding an Al/Cr ratio. When the potential is increased to –200 V, the kinetic energy of the incoming ions spikes, intensifying selective (preferential) re-sputtering of the lighter Al atoms from the growing layer. Conversely, the heavier Cr atoms exhibit a lower sputtering yield under these conditions and remain securely bound within the matrix. This process shifts the overall film stoichiometry toward a lower Al atomic fraction and compresses the Al/Cr ratio [17]. The high-energy ion bombardment at –200 V also generates high residual compressive stresses and a high concentration of point defects (vacancies and interstitials). Under these conditions, the thermodynamically stable CrN phase exhibits a lower free energy of formation and a higher cohesive energy compared to the metastable cubic AlN phase. This difference suppresses the retention of metastable c-AlN. The structural stress forces the excess, unbonded aluminum out of the primary lattice. This displaced aluminum either migrates via stress-driven diffusion to the grain boundaries – forming thin, amorphous AlN_x interlayers – or is stripped from the surface by continuous secondary plasma ion erosion.

4.3. Analysis of Impurities (C and Fe)

The inclusion of trace impurities provides additional insight into the CA-PVD deposition environment.

The carbon (0.68 to 0.14 at.%) acts as a typical residual interstitial impurity, originating from background hydrocarbons in the vacuum chamber (10^{-3}–10^{-5} Pa). At –50 V, these volatile carbon species easily co-condense onto the cold adatom sites. Raising the bias voltage to –20 V activates an ion cleaning effect [18]. The energetic ion flux imparts sufficient momentum to break weak C-C and C-metal bonds, desorbing these weakly adhered contaminants and driving the carbon content down to a negligible 0.14 at.%.

The iron (0.35 to 0.62 at.%) trace shows an opposite trend, increasing alongside the negative substrate bias. Since the coatings are deposited on an AISI 321 stainless steel substrate, this iron signature is driven by ion-stimulated interdiffusion at the film-substrate interface. The high-energy ion bombardment at –50 V creates forward-recoil atom displacements and a high density of point defects within the near-surface layers of the steel substrate [19]. This defect network acts as a series of high-speed diffusion pathways, prompting Fe atoms to migrate upward into the initial chromium adhesion layer and the subsequent AlN/CrN nanostructure.

CONCLUSIONS

This paper establishes the regularities governing the formation of the atomic-crystalline architecture, surface topography, and chemical composition of CA-PVD AlN/CrN multilayer coatings. Based on a comprehensive analysis (XRD, SEM/EDS), the following conclusions were drawn.

1. Three distinct structural regimes of phase evolution were identified. At low deposition energies (–50 V, 10 s), the epitaxial template effect of the c-CrN matrix dominates, stabilizing the metastable cubic c-AlN phase. A bias of –100 V (40 s) breaks down the pseudomorphic growth, transitioning the system into a nanocrystalline state. At an extreme bias potential of –200 V (60 s), complete thermal relaxation occurs, accompanied by a textured phase transition into stable hexagonal wurtzite h-AlN(100).
2. The evolution of surface topography is governed by the deposition energy. The –100 V regime was identified as optimal, where the intensified ion flux smooths the macroparticle boundaries, expanding the defect-free matrix to 82–85%. At –200 V, an over-bombardment regime takes over, triggering selective etching of the nitride phase and exposing heavier metallic droplets.
3. The elemental composition changes were determined. A counterintuitive decrease in Al concentration (from 46.88 to 33.72 at. %) was recorded despite the prolonged growth time. This phenomenon is driven by the mass-dependent selective re-sputtering of lighter Al atoms under high-energy ion flux. Increasing the bias voltage activates an ion-cleaning effect that reduces carbon contamination (down to 0.14 at. %), but simultaneously stimulates iron interdiffusion from the steel substrate into the coating (increasing up to 0.62 at. %).

The insights obtained expand the current understanding of non-equilibrium solid-state thermodynamics and open new avenues for the precision engineering of nanostructured protective coatings.

Acknowledgments

This work was supported by the Ministry of Education and Science of Ukraine (MES) under the National Budget Program (Project 0124U001127).

ORCID

Olga Maksakova, https://orcid.org/0000-0002-0646-6704; **Vyacheslav Beresnev**, https://orcid.org/0000-0002-4623-3243;
Serhii Lytovchenko, https://orcid.org/0000-0002-3292-5468; **Ruslan Galushkov**, https://orcid.org/0000-0002-9105-9774

REFERENCES

[1] W. Cheng, J. Wang, X. Ma, P. Liu, P.K. Liaw, and W. Li, "A Review on Microstructures and Mechanical Properties of Protective Nano-Multilayered Films," J. Mater. Res. Technol. **27**, 2413–2442 (2023). https://doi.org/10.1016/j.jmrt.2023.10.012

[2] B. Warcholinski, A. Gilewicz, P. Myslinski, E. Dobruchowska, and D. Murzynski, "Structure and Properties of AlCrN Coatings Deposited Using Cathodic Arc Evaporation," Coatings, **10**(8), 793 (2020). https://doi.org/10.3390/coatings10080793

[3] A.E. Reiter, V.H. Derflinger, B. Hanselmann, T. Bachmann, and B. Sartory, "Investigation of the properties of $Al_{1-x}Cr_xN$ coatings prepared by cathodic arc evaporation," Surf. Coat. Technol. **200**, 2114–2122 (2005). https://doi.org/10.1016/j.surfcoat.2005.01.043

[4] K. Lukaszkowicz, J. Sondor, A. Paradecka, M. Pawlyta, B. Chmiela, M. Pancielejko, B. Szczucka-Lasota, *et al*., "Structure and Tribological Properties of AlCrN + CrCN Coating," Coatings, **10**(11), 1084 (2020). https://doi.org/10.3390/coatings10111084

[5] J.F. Tang, C.Y. Lin, F.C. Yang, and C.L. Chang, "Influence of nitrogen content and bias voltage on residual stress and the tribological and mechanical properties of CrAlN films," Coatings, **10**(6), 546 (2020). https://doi.org/10.3390/coatings10060546

[6] H. Cao, J. Yang, Y. Li, L. Ren, F. Qi, N. Zhao, Y. Zhou, *et al*., "Effect of nitrogen pressure on the microstructure, mechanical and electrochemical properties of CrAlN coatings deposited by filter cathode vacuum arc," Ceramics International, **48**(24), 36570-36584 (2022). https://doi.org/10.1016/j.ceramint.2022.08.216

[7] C. Sabitzer, J. Paulitsch, S. Kolozsvári, R. Rachbauer, and P.H. Mayrhofer, "Impact of bias potential and layer arrangement on thermal stability of arc evaporated Al-Cr-N coatings," Thin Solid Films, **610**, 26–34 (2016). https://doi.org/10.1016/j.tsf.2016.05.011

[8] A.D. Pogrebnyak, A.P. Shpak, N.A. Azarenkov, and V.M. Beresnev, "Structures and properties of hard and superhard nanocomposite coatings," Physics-Uspekhi, **52**(1), 29 (2009). https://doi.org/10.3367/UFNe.0179.200901b.0035

[9] S. Liu, Y. Yang, R. Ji, X.T. Zeng, and W.J. Clegg, "AlN/CrN multilayer structures with increased thermal stability," Scripta Materialia, **130**, 242-246 (2017). https://doi.org/10.1016/j.scriptamat.2016.12.020

[10] W-C. Huang, and H-W. Chu, "Influence of Layer Configuration on the Morphology and Corrosion Resistance of CrAlN/TiSiN Multilayer Coatings Prepared via Cathodic Arc Deposition," Coatings, **16**(6), 658 (2026). https://doi.org/10.3390/coatings16060658

[11] J. Nyman, M. Junaid, N. Sarius, J. Birch, S. Kahl, and H. Högberg, "Substrate bias effects on cathodic arc deposited Cr coatings," Results in Materials, **19**, 100450 (2023). https://doi.org/10.1016/j.rinma.2023.100450

[12] Z. Chen, D. Holec, M. Bartosik, P.H. Mayrhofer, and Z. Zhang, "Crystallographic orientation dependent maximum layer thickness of cubic AlN in CrN/AlN multilayers," Acta Materialia, **168**, 190-202 (2019). https://doi.org/10.1016/j.actamat.2019.02.004

[13] M. Bartosik, M. Todt, D. Holec, J. Todt, L. Zhou, H. Riedl, H. J. Böhm, *et al*.,."Thermal expansion of rock-salt cubic AlN," Applied Physics Letters, **107**(7), 071602 (2015). https://doi.org/10.1063/1.4928911

[14] B. Alling, A.V. Ruban, A. Karimi, O.E. Peil, S.I. Simak, L. Hultman, and I.A. Abrikosov, "Mixing and decomposition thermodynamics of *c*−Ti1−*x*Al*x*N from first-principles calculations," Physical Review B, **75**(18), 045123 (2007). https://doi.org/10.1103/PhysRevB.75.045123

[15] J. Musil, "Hard and superhard nanocomposite coatings," Surface and Coatings Technology, **125**(1-3), 322-330 (2000). https://doi.org/10.1016/S0257-8972(99)00586-1

[16] G. Greczynski, J. Lu, M. Johansson, J. Jensen, I. Petrov, J.E. Greene, and L. Hultman, "Selection of metal ion irradiation for controlling Ti1-xAlxN alloy growth via hybrid HIPIMS/magnetron co-sputtering," Vacuum, **86**(8), 1036-1040 (2012). https://doi.org/10.1016/j.vacuum.2011.10.027

[17] Z. Zhang, and M.G. Lagally, "Atomistic Processes in the Early Stages of Thin-Film Growth," Science, **276**(5311), 377-383 (1997). https://doi.org/10.1126/science.276.5311.37

[18] A. Metel, Y. Bublikov, Y. Melnik, C. Sotova, F. Milovich, A. Seleznev, *et al*., "Features of the Process of Surface Preparation of Products Using Glow Discharge Plasma During the Deposition of Modifying Coatings," Journal of Composites Science, **9**(12), 640 (2025). https://doi.org/10.3390/jcs9120640

[19] X. Li, B. Bakhit, M.P. Johansson Jõesaar, L. Hultman, I. Petrov, and G. Greczynski, "Toward energy-efficient physical vapor deposition: Routes for replacing substrate heating during magnetron sputter deposition by employing metal ion irradiation," Surface and Coatings Technology, **415**, 127120 (2021). https://doi.org/10.1016/j.surfcoat.2021.127120

ЕПІТАКСІАЛЬНА СТАБІЛІЗАЦІЯ ТА РАДІАЦІЙНО-СТИМУЛЬОВАНА СЕГРЕГАЦІЯ У БАГАТОШАРОВИХ ПОКРИТТЯХ AlN/CrN, ОТРИМАНИХ МЕТОДОМ CA-PVD ЗА УМОВ ІОННОГО БОМБАРДУВАННЯ

О.В. Максакова, В.М. Береснєв, С.В. Литовченко, Р.С. Галушков

Харківський національний університет імені В.Н. Каразіна, майдан Свободи, 4, 61000 Харків, Україна

У цій роботі досліджено закономірності формування атомно-кристалічної архітектури, топографії поверхні та хімічного складу багатошарових покриттів AlN/CrN, осаджених методом катодно-дугового фізичного осадження з парової фази на підкладки з аустенітної нержавіючої сталі AISI 321. Проаналізовано синергетичний вплив від'ємної напруги зміщення до підкладки (від –50 до –200 В) та тривалості осадження індивідуальних шарів AlN (10, 40 і 60 с) на кінетику фазової конкуренції та еволюцію радіаційно-стимульованих наноструктур. Методами рентгенівської дифракції та растрової електронної мікроскопії у поєднанні з енергодисперсійною рентгенівською спектроскопією встановлено, що за низьких енергій осадження (–50 В, 10 с) домінує ефект епітаксіального шаблону матриці c-CrN, тим самим стабілізуючи метастабільну кубічну фазу c-AlN. Збільшення як товщини шару, так і напруги зміщення до –100 В призводить до руйнування псевдоморфного росту та

переводить систему в ймовірний нанокристалічний або квазіаморфний стан. За високого потенціалу зміщення –200 В відбувається повна термічна релаксація, що супроводжується текстурованим фазовим переходом AlN у його стабільну гексагональну модифікацію вюрциту (h-AlN). Спостерігалося контр-інтуїтивне зниження концентрації алюмінію (з 46,88 до 33,72 ат.%), незважаючи на тривалий час росту . Цей феномен зумовлений селективним перерозпиленням легших атомів Al під дією високоенергетичного іонного потоку. Крім того, було зафіксовано радіаційно-стимульовану інтердифузію заліза з підкладки у покриття, разом із ефектом іонного очищення, який видаляє домішки впровадження вуглецю з матриці. Отримані результати розширюють поточне розуміння нерівноважної термодинаміки твердого тіла та відкривають нові можливості для прецизійного проєктування властивостей наноструктурних захисних покриттів шляхом оптимізації іонно-плазмових параметрів.

Ключові слова: *вакуумно-дугова технологія; нітриди; багатошарові покриття; AlN; CrN; мікроструктура; хімічний склад; фазовий стан*